GHENT
UNIVERSITY

FACULTY
OF SCIENCES

Diving into the colloidal synthesis of Transition Metal Dichalcogenides

Gabriele Pippia

Promotor: Prof. Dr. Ir. Iwan Moreels

Co-promotor: Prof. Dr. Ir. Zeger Hens

Thesis submitted in fulfillment
of the requirements of the degree of
Doctor of Science in Chemistry
Academic year 2022-2023

Promotor

Prof. Dr. Ir. Iwan Moreels	Department of Chemistry

Co-promotor

Prof. Dr. Ir. Zeger Hens	Department of Chemistry

Chair

Prof. Dr. Klaartje De Buysser	Ghent University

Jury members

Pr. Dr. Peter Vandenabeele	Ghent University
Prof. Dr. Ir. Pieter Geiregat	Ghent University
Dr. Beatriz Martín-García	CIC nanoGUNE
Dr. Jannika Lauth	Leibniz Universität Hannover

Ghent University
Faculty of Science

Department of Chemistry
Krijgslaan 281 Building S3, B-9000 Gent, Belgium

This work was supported by the European Research Council (ERC) under the European Union's Horizon 2020 research and innovation programme (grant agreement No. 714876 PHOCONA).

Acknowledgments

This is the end of a long journey, started four years ago with a simple reply to a vacant position as PhD student. Four years later, I find myself with lots of memories, not only made by the thousands of days in the lab, happiness and frustration, but also (and mostly) by the people I met during this journey, that helped me growing as researcher and, most importantly, as a person. Starting from who made this all possible, I want to thank my supervisor and my co-supervisor, Iwan and Zeger, for letting me start this adventure. Iwan, I appreciated every suggestion and feedback you gave me to improve the quality of my work. Marga, you know that expressing my feelings is not something I'm used to - it is a long road and I'm still far from the end - but you know how much you are important for me. You know better than anyone else the struggle behind this journey of mine and I know better than anyone else the support you gave me during this time. Now it's the turn of my fellow Italian citizens, Alessio and Carmen. I always looked up at you two as source of inspiration not only on how to be a better researcher, but also about how to be a better person. I learnt lots of things from you two, and I can't deny that you were the ones that influenced me the most. You gave me valuable lessons and, overall, I learned to share more my feelings with the people I care about. Thank you. Jari and Benny, a.k.a the Belgian resistance to the Italian invasion of Fun office. I can't deny you also had a huge impact on me, similar to what Ale and Carmen had. Jari, you are one of the brightest person I met so far, you made look everything super easy. Benny, you had a beautiful evolution in these years; you are way different than the guy I met few years ago. You taught me a similar lesson as Ale and Carmen, and I am grateful for that. Fadi, first, sorry for the leadership course (and messing up your survey!). Second, thank for the help you gave me in the lab and in the office, trying to cheer me up all the times you saw me in a bad mood for my research. I appreciated that. Pieter, my North Star regarding TMDs. I don't know how many times I came to you asking random stuff about TMDs, but I know that you always had an answer for me. Hannes, you are the most cheerful guy I ever met so far, always with a smile and a joke to make everyone laugh. Despite all the difficulties, you always managed keep your smile and move forward, no matter what. You are also one of the hardest worker, running synthesis after synthesis (I mean, just look at your thesis and how many things are there) and achieving incredible results. Leila, you are like Schr odinger's cat: you can be super sweet and super scary, depending on who opens the box. Luckily, I never experienced the scary Leila in all the time we spent together, but only the sweet version of you (how can I forget the cake you made for me?), the one that could get in one second which thoughts crossed my mind. Kim, you had the toughest position of all: lab responsible. Enforcing rules, making sure that everyone stay safe in the lab, and trying to keep it running smoothly is not an easy task at all, but you did great, keeping your smile and your cheerful attitude during all of this. Ezat, you are by far the quietest and hardest worker of all PCN. It has always been a joy seeing you in the lab, and sometimes a bit worrying (you definitely work too much!). I really hope all your efforts will pay back soon. To my second favorite spectroscopist, Chandu, I'm sorry that I made you wait so long to measure some decent TMDs, but hey, finally something came out no? It was a pleasure play badminton together and having you around, always so social and talkative. Cristina, my favorite living meme, you are such a unique combination that I can't describe it. The moments with you in the lab were one of the funniest one, and the ones outside even more. You are one of my closest friend and I am happy of that. And now my favorite student, Diem. I still remember the first meeting we had. I was terrified, there was no room for failure. The project had to work, and luckily I had you as a student. I am proud of all the work you did, despite all the difficulties you never surrendered, but you kept fighting over and over. Delphine, thanks you for trying to gather all the group together organizing so many activities. I hope everything with your illness will become better. Wouter, you are not forgotten. I still remember our jokes, our stupid and serious discussions, and your love for guitar and chemistry. I remember you always tapping your fingers on the bench, as if you were actually playing a guitar. I remember the song from SOAD you played all the time to annoy me, where most of the words where changed with the word table. I remember when you brought your chili pepper at the Christmas dinner, and I ate one as a challenge. You are not forgotten my friend. Katrien, thanks for the fun time at the TEM and for entrusting me as vice-captain for the TEM. Pierre and Kathleen, thanks for all the work you did and for solving all the issues I had from the administrative side. Anastasia, thanks for thousands of measurements you did for me, and for the all the lovely conversations we had. Bart, I will miss bothering you all the time with random chats, trying to figure out how to make work all the silly requests you got. Ivo, even if you were rarely around I enjoyed all the (sober and not) chats we had. Ivan, it has been a pleasure having you here and collaborate with you, trying to find an application to my TMDs. Servet, my fellow videogames player, we still need to play something together. Alina, good luck with your PhD, I hope you will get more confident on using the TEM. Tim, we spent so many hours together, and I learnt so much about you. I hope your future will be still bright. Chokri, you and your radio are the sparkle of joy of all S3. Dobromil, Onur, Luca, Jaqueline, Denny, Jing, Thoai, I didn't have the chance to know you better, but I wish you good luck for your research.

Ghent, 2022
Gabriele Pippia

Table of Contents

2 Colloidal Synthesis of Fluorescent MoX_2 (X = S, Se)

List of Common Acronyms

A

Abs	Absorption (spectroscopy)
ARPES	Angle-Eesolved PhotoEmission spectroscopy

C

CBM	Conduction Band Minimum
CVD	Chemical Vapor Deposition

D

DOE	Design Of Experiment
DOS	Density of States
DSD	Definitive Screening Design

E

EDX (EDS)	Energy-Dispersive X-ray Spectroscopy

F

F_4TCNQ	2,3,5,6-Tetrafluoro-7,7,8,8-tetracyano-quinodimethane
FFT	Fourier transform analysis
FWHM	Full Width at Half Maximum

H

HER	Hydrogen Evolution Reaction
HR-TEM	High Resolution Transmission Electron Microscopy

L

LPE	Liquid-Phase Exfoliation

M

MOCVD	Metal-Organic Chemical Vapor Deposition

N

NC	Nanocrystal
nm	nanometer

O

OA	Oleic Acid
ODE	1-Octadecene
OLA	Oleylamine

P

PL	Photoluminescence (spectroscopy)

Q

QD	Quantum Dot
QW	Quantum Well
QWr	Quantum Wire

S

SOC	Spin-Orbit Coupling

T

TEM	Transmission Electron Microscopy
TMD	Transition Metal Dichalcogenide

U

UV-Vis	Ultraviolet-Visible Light (spectroscopy)

V

VBM	Valence Band Maximum
VdW	Van der Waals

X

XPS	X-ray Photoelectron Spectroscopy

1

Introduction

1.1 Research Context

The pressure for technological improvement have pushed the scientific community onto the research of different solutions that can satisfy this constant evolution. While part of the effort is devoted on the optimization of the current technologies and materials (semiconductors) involved on it, the other part is aiming on developing and understanding of new materials that can yield to a new technological evolution. A clear example of this is the light bulb, that evolved from a tungsten filament in an argon-filled bulb to its halogen variant until the research on new type of materials gave birth to the first LED,[1] changing forever the illumination in our homes. Driven by this need, the scientific community spent countless efforts on the study of different semiconductors and their different properties at different scales, finally exploiting the material properties at nanometer (nm, 10^{-9} m) scale. Despite examples of uses of nanocrystals (NCs) can be traced back to 5000 years BC,[2] the modern nanoscience with nanocrystals starts in the early 1980s[3] with the investigation of colloidal semiconductor nanocrystals for light-harvesting applications.[3–5] It is after the explanation of the quantum size effect that such semiconductor nanocrystals were termed quantum dots (QDs).[6–11] Since then the research on colloidal nanocrystals yielded to synthetic protocols that provides narrow size distributions,[12] uniform morphologies, controlled surface chemistry,[13] and enhanced optical properties;[14] making possible to explore new nanocrystals characterized by different degrees of quantum confinement, such as 1D (quantum wire, QWr) and 2D (quantum wells, QW) (Figure 1.1). This tremendous development ultimately led to nanocrystals of such high quality to be suitable for commercial applications, as demonstrated by the first CdSe quantum dot-based TV launched by Sony in 2013.[15]

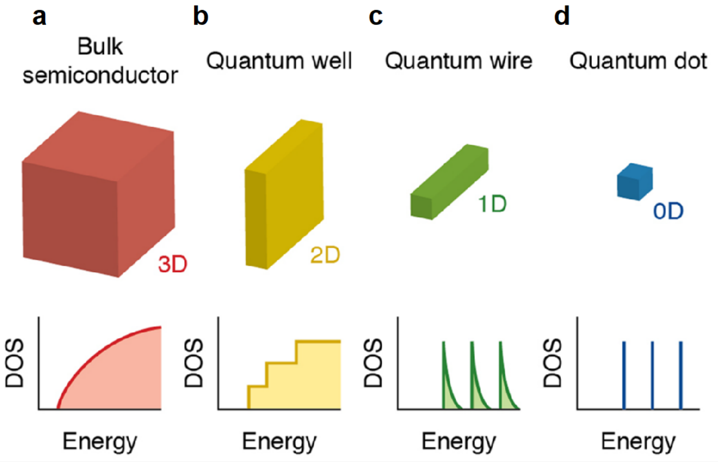

Figure 1.1: Representation of the different nanocrystals dimensionalities and relative Density Of States (DOS) of a bulk semiconductor (a), quantum well (b), quantum wire (c), and quantum dot (d). Reproduced from Ref. 16.

The interest on 2D nanomaterials revamped after the discovery of graphene and its extraordinary properties in 2004 by Nosovelov.[17] As 2D materials, transition metal dichalcogenides (TMDs) and the standard-bearer MoS_2 went under deep study to understand (and exploit) its properties. The discovery of its transition from indirect to direct band gap when reduced to monolayer and its photoluminescent properties by Mak[18] and Splendiani[19] ignited the research on these materials and the possible applications.[20] The combination of sub-nanometer thickness, the strong light-matter interaction, the band gap tunabily, and the broken inversion symmetry in odd-layer number makes TMDs ideal candidates for different applications, such as transistors,[21] catalyst for water-splitting reactions,[22] electronics,[23] photonics,[24] and optoelectronic.[25]

1.2 Transition Metal Dichalcogenides

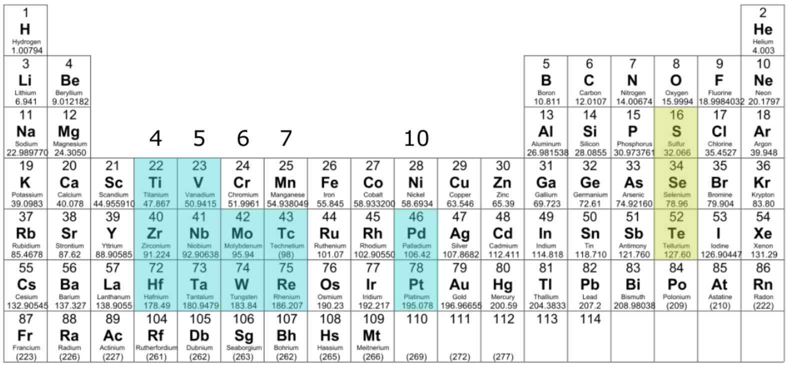

Figure 1.2: Periodic table with highlighted transition metals (cyan) and chalcogens (yellow) part of the TMDs family originating layered structures.

Transition metal dichalcogenides are a class of material with general formula MX_2 (M = transition metal, X = chalcogen) where the transition metal belongs to Groups 4-10; with only Group 4-7 and 10 displaying layered structure (Figure 1.2). This latter subgroup consist in over 40 different materials, with different structure morphology and optoelectronic properties depending on their chemical composition and polytype.

1.2.1 TMDs Crystal Structure

TMDs structure consist in three-atom-thick layers (with structure X-M-X) held together by Van der Waals (VdW) interactions. Each of these layers consist in a hexagonally packed plane of metal atoms sandwiched between two planes of chalcogen atoms, held together by in-plane covalent bonds. The stacking order of the layers determines the polymorphism of the final structure. The most common polytypes are octahedral (1T, D_{3d}^3 point group), trigonal prismatic (2H, D_{3d}^1 point group) and rhombohedral (3R) (Figure 1.3), however is possible

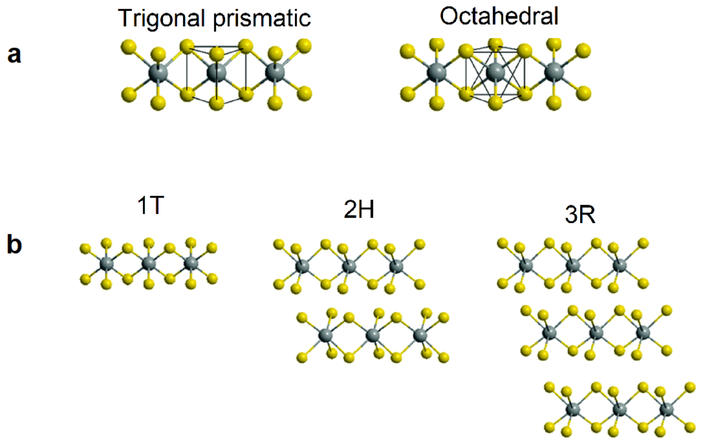

Figure 1.3: (a) Trigonal prismatic and octahedral coordination of metal ion in TMDs. (b) Layer stacking order of the three typical TMDs polytypes. Adapted from Ref. 26.

to have distorted structures such as 1T' for $MoTe_2$.[27] The preferred polytype depends on the d- electron count of the transition metal and its atomic radius. While all Group 4 (d^0) and Group 10 TMDs (d^6) shows only octahedral structure, Group 5 (d^1) feature few trigonal prismatic polytypes as well. This trend becomes opposite in Group 6 (d^2), where the favorite polytype is the trigonal prismatic while Group 7 (d^3) features only 1T/ 1T' distorted polytype.[28]

1.2.2 TMDs Electronic Band Structure

Bulk TMDs have electronic properties that spans from insulators to semiconductors and semimetals, depending on the metal and polytype.[28] This behavior reflects the effect of coordination environment of the metal on the electronic structure. While Group 4 ad Group 7 TMDs are semiconductors, Group 5 TMDs shows metallic/ semimetallic behavior.[29] Group 6 and Group 10 sulfide and selenides are semiconductors while tellurides are semimetals (Group 6) or metals (Group 10).[28]

The Density Of States (DOS) diagram reveals that, independently of the polytype, the non-bonding d orbitals are located between the bonding (σ) and antibonding (σ^*) orbitals (Figure 1.4). In octahe-

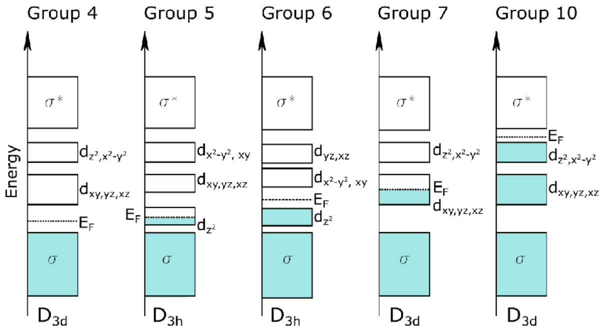

Figure 1.4: Density Of States scheme of Group 4-7 and 10 TMDs, with highlighted the non-bonding *d* orbitals.

drally coordinated metal atoms (D_{3d}, Group 4, 7 and 10) the non-bonding orbitals include $d_{z^2,x^2\text{-}y^2}$ and $d_{yz,xz,xy}$ while for trigonal prismatic coordination (D_{3h}, Group 5 and 6) the non-bonding orbitals are formed by d_{z^2}, $d_{x^2-y^2,xy}$ and $d_{xz,yz}$ with a sizeable gap (∼1 eV) between the first two groups of orbitals.[28] The chalcogen atoms effect on DOS is lower compared to the metal atoms, with a progressive broadening of the *d* bands and a decrease in band gap energy increasing the atomic number of the chalcogen.[29] TMDs are well-known for the thickness-dependent band gap reorganization; however this is not valid for all of them. For instance, while Group 6 TMDs shows an indirect-to-direct band gap conversion and an increasing of band gap energy going from bulk to monolayer, Group 4 TMDs band structure remains almost unchanged.[30]

1.2.3 Group 6 TMDs (G6-TMDs)

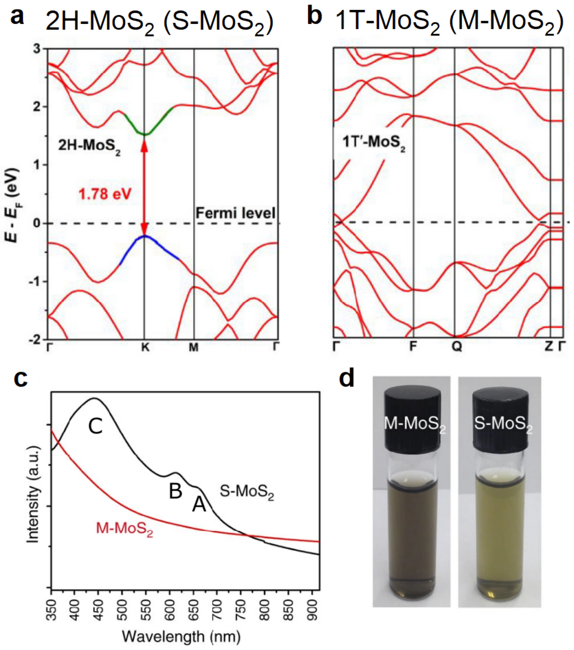

Figure 1.5: Comparison between electronic band structure of (a) monolayer 2H-MoS$_2$ and (b) monolayer 1T-MoS$_2$. Adapted from Ref. 31. Copyright 2020 American Chemical Society. c) UV-Visible absorption spectrum of 1T-MoS$_2$ (M-MoS$_2$, red trace) and 2H-MoS$_2$ (S-MoS$_2$, black trace) with highlighted the three absorption bands A, B, C, and d) colloidal suspension of the aforementioned samples. Adapted from Ref. 32

This subclass features the most studied TMDs, such as molybdenum and tungsten disulfide (MoS$_2$, WS$_2$), diselenide (MoSe$_2$, WSe$_2$), and ditelluride (MoTe$_2$, WTe$_2$). As described before, the stacking order of the single layers determines their polytype and electronic structure; the 1T polytype determines a metallic nature while the 2H polytype determines a semiconducting nature for disulfides and diselenides and semimetallic for ditellurides.[29] As an example, in Figure 1.5a is reported the difference in the electronic structure for the 1T and 2H polytype of monolayer MoS$_2$;[33] this difference in the electronic structure is reflected in the different optical properties (Figure 1.5c). The 2H-MX$_2$ nanocrystals (M = Mo, W; X = S, Se) have been subject to extensive studies in the last decades due to their opto-electronic properties such as thickness-dependent band gap energy, indirect-to-direct transition going from bulk to monolayer, and broken inversion symmetry in odd-number of layers.

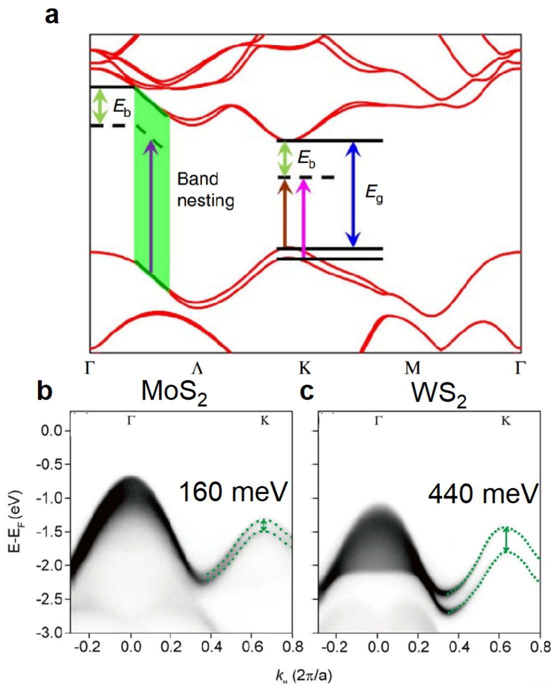

Figure 1.6: (a) Energy band structure of MoS_2 monolayer with highlight the of A/B/C electronic transitions (considering the spin-orbit coupling), the band gap energy the direct band gap transitions (E_g) and the exciton binding energy E_b. The green area is the band nesting region. Adapted from Ref. 34. (b-c). ARPES data of MS_2 (M = Mo, W) valence band with highlighted the spin-orbit interaction energy gap. Adapted from Ref. 35.

The electronic band structure of MX_2 is characterized by a direct transition between valence and conduction band at the K point of the Brillouin zone,[18,19] with the splitting of the valence band at K point originated by the spin-orbit coupling (SOC),[36,37] and a band nesting region[34,38] (where valence and conduction bands are parallel to each other in energy) (Figure 1.6). This valence band splitting originates the A and B transitions seen in Figure 1.5c (while the band nesting region originates the C transition); using angle resolved photoemission spectroscopy (ARPES) the energy splitting has been found to go from ~160 meV for MoS_2 to ~400 meV for WS_2 (Figure 1.6b and c).[35]

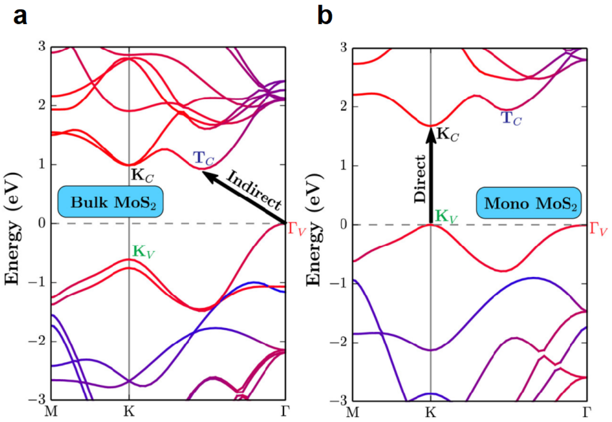

Figure 1.7: (a). Electronic band structure of bulk MoS_2 with highlighted the indirect band gap transition. (b). Electronic band structure of monolayer MoS_2 with highlighted the direct band gap transition. Adapted with permission from Ref. 39. Copyright 2015 American Chemical Society.

1.2.4 Band gap conversion in G6-TMDs

The electronic structure of G6-TMDs is well known for its conversion from indirect-to-direct band gap due to the strong quantum confinement effect along the thickness direction (Figure 1.7).[18, 19, 39, 40] The quantum confinement effect arises as a result of geometrical confinement of excitons[41] when one (or more) of the nanocrystal dimension is approaching the size of the Bohr radius (a_0, distance between electron and hole pair). In bulk G6-TMDs the transition between valence and conduction band is not at the K point of the Brillouin zone but between the Γ point of the valence band and the T_C point of the conduction band. This transition is labeled as indirect since the wave vector is not conserved, requiring a phonon for momentum conservation[42] while in a direct transition the wave vector is conserved. The low oscillator strength associated to phonon-assisted indirect transition makes this transition not visible,[18] differently than the direct transitions, characterized by a strong oscillator strength.[43] To explain the indirect-to-direct band gap transition is necessary to evaluate the electronic wave functions in a VdW system, where the electronic wave function does not extend in the space separating the single layers.[39] In MoS_2, the electronics states of conduction (K_C) and valence band (K_V) (mostly made of Mo d, S p_x and p_y orbitals) are intralayer localized, making them insensible to the changes in number of layers. The Γ_V and T_C electronic states are made mostly of Mo d and S p_z orbitals, displaying a substantial delocalization in the interlayer region, differently than the common VdW solids (Figure 1.8).[39] As a result, these states are strongly bounded with the adjacent layers, showing significant energy variation with the number of layers. The overlapping of the electronic states intra- and interlayer in real and k-space yields to three different transition regimes: indirect I transition (when number n of layer > 5) $\Gamma_V \rightarrow T_C$, where the transition in k-space is indirect (*i.e.*, momentum is not conserved) while is direct in real space (*i.e.*, overlap of wave functions); Indirect II transition ($1 <$ n $<$ 5 layers) $\Gamma_V \rightarrow K_C$, where both k- and real space are characterized by indirect transitions; and direct transition $K_C \rightarrow K_C$ in monolayer, where the transition is direct in both k- and direct space.[39] This transition is not available for $MoSe_2$ and WSe_2 that go directly from indirect I to direct band gap transition. The energy of A, B, and C transitions have been found to be thickness-dependent, blue shifting while decreasing the number of layers;[18, 44–46] this has been attributed

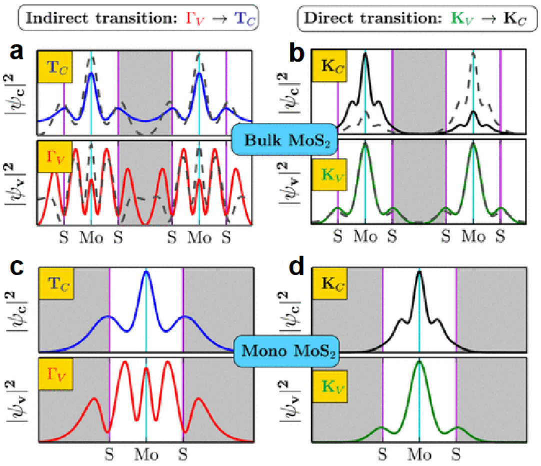

Figure 1.8: Planar-averaged squared magnitude of wave functions of the band-edge states for the bulk and the monolayer plotted along the direction perpendicular to the layers. Panels (a,c) refer to the indirect band gap transition, and panels (b,d) correspond to the direct transition. The interstitial region outside the sandwich S-Mo-S layers is shown in gray. Adapted with permission from Ref. 39. Copyright 2015 American Chemical Society.

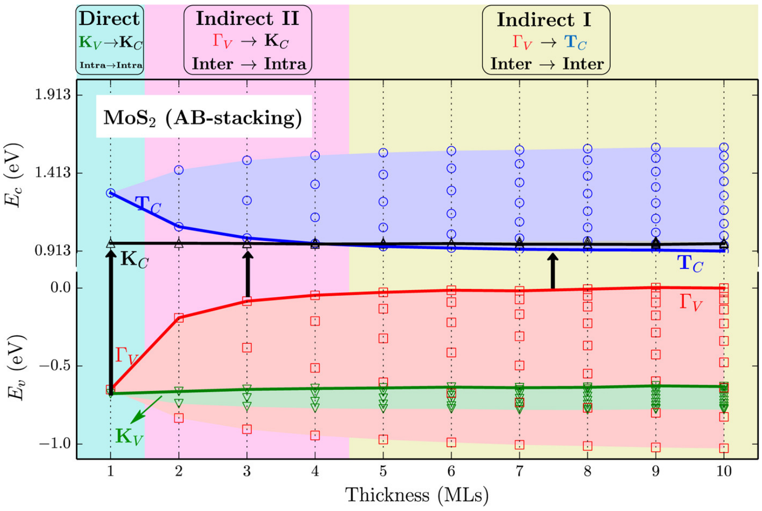

Figure 1.9: Evolution of various band-edge states of MoS$_2$ going from multilayer to the monolayer. The light color indicates the span of the single states energy levels. The band gap transitions features three regimes: Indirect I (Γ_V → T_C, yellow), Indirect II (Γ_V → K_C, pink), and Direct (K_V → K_C, cyan). Reprinted with permission from Ref. 39. Copyright 2015 American Chemical Society.

to size and thickness-induced scattering effect.[23,47]

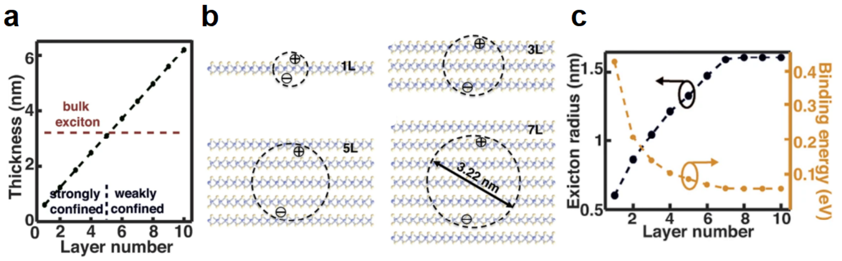

Figure 1.10: (a) Definition of weak and strong quantum confinement regime according to the size of the exciton in bulk MoS_2 and the thickness of MoS_2 nanocrystal. When the number of layers < 5 the exciton experiences strong quantum confinement. (b) Schematic illustration of the size of excitons in the films with different layer numbers. (c) Correlation between MoS_2 C exciton binding energy and Bohr radius with the number of layers. Adapted from Ref. 50.

1.2.5 Excitons in G6-TMDs

When interacting with a photon having suitable energy, an electron is promoted from the valence to the conduction band, leaving a vacancy (hole) in the valence band. This electron-hole pair, bounded via Coulomb interaction, is called exciton. According to the number of layers, excitons in TMDs can experience weak or strong quantum confinement (Figure 1.10a), determining their binding energies and Bohr radius; in monolayer MoS_2 the exciton binding energy is ~0.5 eV[48, 49] while the Bohr radius is 0.602 nm.[50, 51] This strong Coulomb interaction (assisted by the low dielectric screening outside the monolayer) translates to up to 20% absorption per monolayer at the exciton resonance in the spectral region.[52]

The generated excitons can recombine following different pathways, radiative (with photoemission) or non-radiative (without photoemission). Radiative photoemission (*i.e.*, bright exciton) is present when the electron-hole pair are on the same wave vector K of the Brillouin zone.[53] When the electron-hole pair are located on different wave vectors, the radiative pathway is not available, and the exciton is called a momentum-forbidden dark exciton (if the electron-hole pair have different spin then we talk about spin-forbidden dark excitons).[53] Excitons can recombine non-radiatively even being on the same wave vector due to the presence of defects, that acts as non-radiative center.[45] The native presence of defects makes TMDs poorly luminescent, with a quantum efficiency (QE%) of 0.6%[54] even in mechanically exfoliated samples. TMDs are affected by the presence of different typologies of defects, such as chalcogen or metal vacancies,[55] chalcogen adatom,[56] and grain boundaries.[57,58] The synthetic route influence the type of defects present in the material; samples obtained via chemical vapor deposition (CVD) and mechanical exfoliation are characterized by chalcogen vacancies, while samples obtained via physical vapor deposition (PVD) are characterized by antisite defects (*i.e.*, metal atom occupying chalcogen position).[55] *Ab initio* calculations on mechanically exfoliated MoS_2 have shown that chalcogen vacancies are energetically favorite, with formation enthalpies of 2 eV.[55] The presence of S vacancies on mechanically exfoliated samples has been rationalized considering that either Mo and S are prone to reach a solid-gas phase equilibrium on the exfoliated material; hence as the saturated vapour pressure of sulfur is higher than molybdenum, more S is released compared to Mo, making the material S deficient.[55] In case of CVD-synthesized MoS_2, the presence of S vacancies is caused by the precursor used in the synthesis, typically MoO_3. To convert the oxide into disulfide it is necessary to run the synthesis in S-rich conditions; however residual oxygen atoms may be still present in the structure. Such atoms have been found to be less stable than sulfur, hence they tend to desorb into the gas phase, leaving a vacancy in the S site.[55] In case of PVD samples, the MoS_2 precursor is sublimated into gas-phase as clusters and atoms, carried by Ar/H_2, and then condensed into a solid-phase MoS_2. As stated above, S possesses an higher saturated vapour pressure than Mo, yielding a S-deficient (and Mo-rich) environment. These clusters and atoms are highly mobile, prone to form a structure with the lowest total energy; energetic calculation show that for this system, the formation of antisite defects is favorite compared to sulfur vacancies.[55] The presence of defects generates new electronic states inside the band gap;[59,60] S vacancies produce shallow hole trap and deep electron trap states while antisite defects form deep electron traps and two different hole traps (a shallow hole trap close to the valence band and a deep hole trap close to the deep electron trap).[61] Despite being the n-type behaviour associated to S vacancies, it has been found that it is correlated to the presence of interstitial impurities generated during the growth process.[62] The n-type behavior can be tailored using doped substrates,[63] via chemical passivation[64] or doping with p-type molecules (Figure

1.11),[65,66] potentially yielding to QE% close to near-unity.[54]

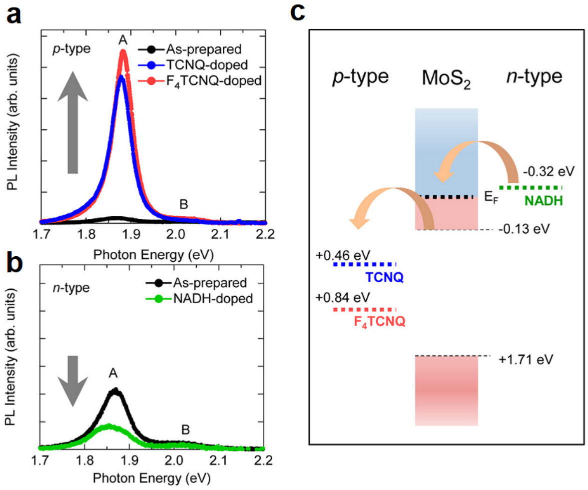

Figure 1.11: (a) Photoluminescence spectra of monolayer MoS_2 before and after *p*-type doping. (b) PL spectra of monolayer MoS_2 before and after *n*-type doping. (c) Relative potentials (vs Standard Hydrogen Electrode) of monolayer MoS_2 and *n*- and *p*-type dopants. Reprinted from Ref. 65. Copyright 2013 American Chemical Society.

Several molecules have been found suitable as dopants, such as thiol molecules,[64,67,68] oleic acid,[69] bis(trifluoromethane) sulfonimide (TFSI),[54,70] hydrohalic acids,[71] 2,3,5,6-tetrafluoro-7,7,8,8-tetracyanoquinodimethane (F_4TCNQ) or 7,7,8,8-tetracyanoquinodimethane (TCNQ) (Figure 1.11a),[65,72,73] xylene,[74] oxygen,[75] and water.[76–78] These molecules acts via chemisorption (e.g. thiol molecules), passivating the surface defects[64,67] or via physisorption (e.g. F_4TCNQ) where the position of the molecule lowest unoccupied molecular orbital (LUMO) and highest occupied molecular orbital (HOMO) compared to the VBM and CBM of the material determine its n-type or p-type doping effect.[65,73]

1.2.6 Group 6 TMDs - MX_2 alloys

Beside via thickness control or doping, another way for fine-tune the electronic band structure is via alloying (Figure 1.12). A careful control on the composition permits to explore the energy region

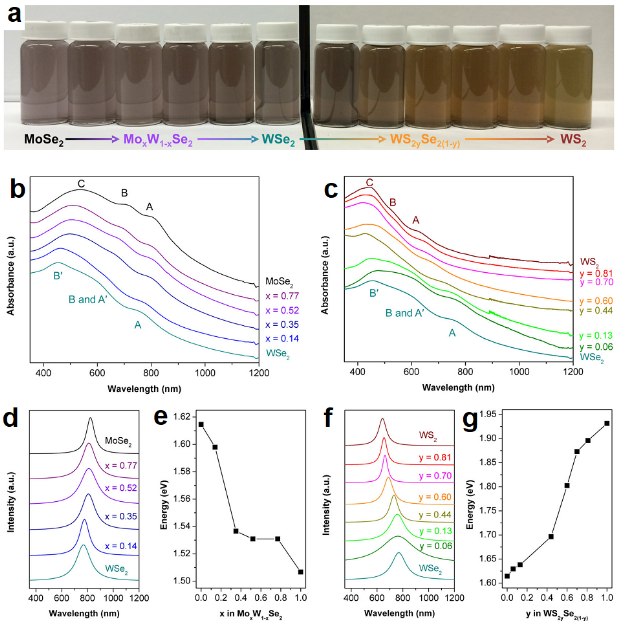

Figure 1.12: Optical properties of colloidal TMD alloys. (a) Photograph of $Mo_xW_{1-x}Se_2$ and $WS_{2y}Se_{2(1-y)}$ samples suspended in ethanol. (b) Normalized UV–Vis absorbance spectra, (c) A excitonic, and (d) corresponding energy for $Mo_xW_{1-x}Se_2$ nanostructures. (e) Normalized UV–Vis absorption spectra, (f) A excitonic peaks, and (g) corresponding energy for $WS_{2y}Se_{2(1-y)}$ nanostructures. Adapted from Ref. 79. Copyright 2017 American Chemical Society.

between the single alloy components[79–83] (Figure 1.12d and g); ultimately leading to a precise control of the alloy properties, such as photoluminescence (Figure 1.12c and f).[84] Not all materials can be combined into alloys; as selection rules the alloy components must have similar lattice symmetry and small lattice mismatch.[84] In this regard, TMDs within the same transition metal group can form alloys, due to the similar lattice symmetry and the small lattice mismatch.[84] Ternary TMDs alloys can combine different chalcogenides,[79, 85–87] such as $MoS_xSe_{(2\text{-}x)}$,[85] or different transition metals[79, 88] such as $Mo_xW_{(1\text{-}x)}Se_2$.[79] Quaternary alloys, such as $Mo_xW_{1\text{-}x}S_ySe_{2\text{-}y}$ are also possible.[89] Theoretical calculation have shown that ternary and quaternary alloys have negative formation enthalpies despite the energy loss due to lattice mismatch.[90] Quaternary alloys, thanks to the band gap energy region covered (that spans from 1.40 eV to more than 1.80 eV, Figure 1.13), are a promising material for different applications, such as solar absorbers,[90] field effect transistors,[91] optoelectronic devices,[92] and catalyst for water-splitting reactions.[93]

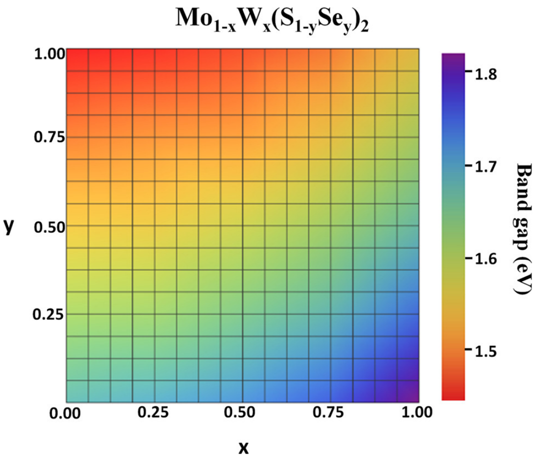

Figure 1.13: Band gap region of quaternary TMD alloys $Mo_xW_{1-x}S_{2y}Se_{2(1-y)}$ as functions of compositions x and y. Reproduced from Ref. 90. Copyright 2018 American Chemical Society.

TMDs alloys can be produced using different strategies, such as colloidal synthesis,[79,87] or wet chemical route,[94] exfoliation from bulk (produced by chemical vapor transport),[95] chemical vapor deposition,[89] and chalcogen exchange.[96] In addition, colloidal synthesis and CVD permits the synthesis of lateral (where different 2D crystals bonded in a single atomic layer) or vertical (where layers of different materials are stacked by VdW interactions) heterostructures[97–100] (Figure 1.14a and b) and Janus alloys (Figure 1.14c). While in lateral heterostructures the oriented growth occurs only when the materials have similar lattice symmetry and low lattice mismatch,[103] vertical heterostructures (VdW heterostructures) don't suffer from these limitations,[104,105] allowing the formation of heterostructures with large lattice mismatch (over 50%).[106] Following the Anderson's Rule[107] for semiconductors, the relative position of conduction band minimum (CBM) and valence band maximum (VBM) of the combined materials (aligned at vacuum energy levels) determine the type of heterostructure, namely Type-I, *quasi*- Type-II and Type-II[97] (it is

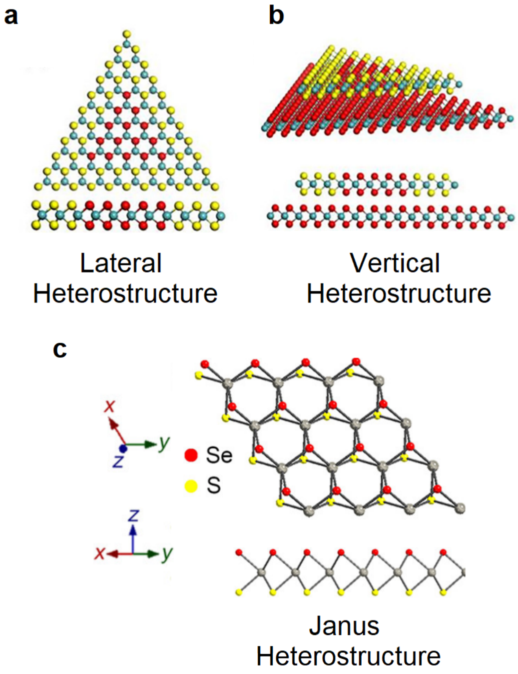

Figure 1.14: Example of lateral heterostructure (a) and vertical heterostructure (b). Adapted from Ref. 101. Copyright 2019 American Chemical Society. (c) MoSSe Janus heterostructure. Adapted from Ref. 102. Copyright 2021 American Chemical Society.

also possible a Type III, that is similar to Type II but without band gap, acting as semimetal).[108] In a Type-I heterostructures, such as CdSe/ZnS or MoS_2/ReS_2[109] (Figure 1.15a), CBM and VBM are located in the same material, that possess the narrower band gap.[109] As a result, the photogenerated carriers are localized in the same material; if the carriers are generated in the wider-gap material, they will move to the narrower-gap material. In a *quasi*- Type-II (or Type-I$\frac{1}{2}$) heterostructure, such as CdSe/CdS (Figure 1.15b), either their CBM or VBM are similar in energy; as a result one of the carriers will be delocalized on the entire heterostructure. In a Type-II heterostructure, such as CdSe/ZnTe or MoS_2/WSe_2[108] (Figure 1.15c) CBM and VBM are located in different materials, and the resulting photogenerated electron-hole couple will be localized in different materials, ultimately

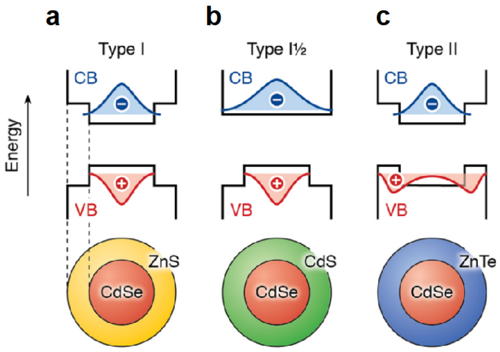

Figure 1.15: Schematic representation of the carrier localization in (a) Type-I heterostructure, (b) Type *quasi*–Type-II and (c) Type-II heterostructure. Reproduced from Ref. 16.

increasing the lifetime of the recombination. This is the most common adopted typology for G6-TMDs.[108]
A particular TMD heterostructures are the Janus alloys (Figure 1.14c) (or in general Janus nanoparticles), defined as materials whose surfaces possess two or more distinct physical properties, obtained via different composition or functionalization.[110] The synthesis of such materials features different strategies, such as masking and functionalization, phase separation, self-assembly[110] and physical deposition.[111] In case of Janus TMDs, these are obtained via CVD, replacing a chalcogenide layer on the surface.[112] The broken vertical symmetry generates an intrinsic out-of-plane dipole that yields to superior photocatalytic activity,[113,114] large in-plane and vertical piezoelectricity,[115] and slower exciton recombination compared to pristine TMDs.[102]

1.3 Production methods

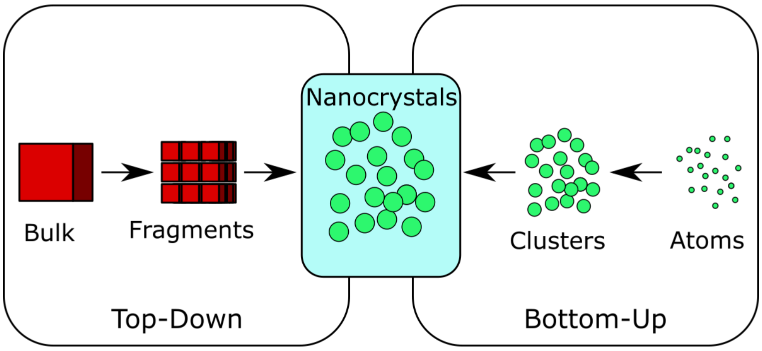

Figure 1.16: Representative scheme of Top-Down and Bottom-Up approaches in the synthesis of nanostructured materials.

The production strategies used for the production of TMDs (and more in general of nanocrystals) can be categorized in two main typologies, according to the starting species: Top-Down and Bottom-Up approaches (Figure 1.16). A top-down approach use as starting species bulk material, that is then reduced in size using different techniques. An example of this is the synthesis of graphene,[17] that is obtained peeling off the single layers that constitute graphite structure. On the other hand, bottom-up approach starts from the atomic (or molecular) precursors to build the final nanostructures. An example of bottom-up is the colloidal synthesis of MoS_2 described in Chapter 2. Some of these strategies will be briefly described in the following sections.

1.3.1 Top-down

1.3.1.1 Mechanical cleavage

Mechanical cleavage refers to a group of techniques (micro and nanomechanical cleavage) that uses mechanical force to separate the single layers present in the bulk structure. Micromechanical cleavage is the first successful technique used in graphite exfoliation (Figure 1.17a);[17] using scotch-tape to peel off the single layers. It ensures high quality material with the downside of low production rate,[118] making it ideal only for research studies. The nanomechanical cleavage variant utilizes a very sharp tungsten probe with a 10 nm tip controlled by piezoactuators, that permits to obtain high quality

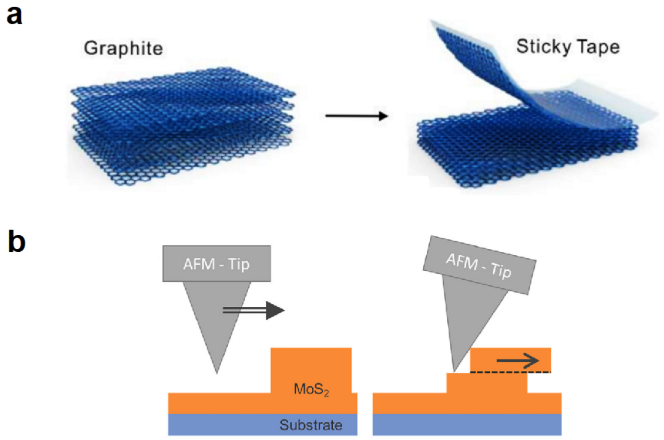

Figure 1.17: (a) Representation of the scotch-tape method used in graphene fabrication. Adapted from Ref 116. (b) Representation of micromechanical cleavage of MoS_2. Adapted from Ref 117. Copyright 2022 American Chemical Society.

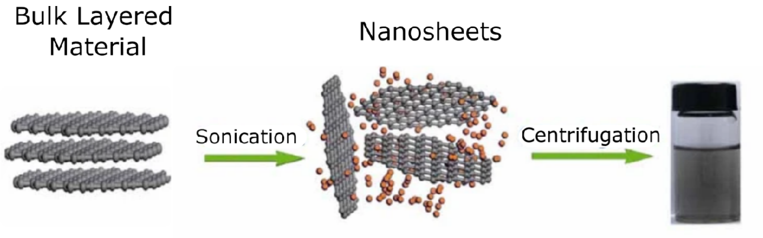

Figure 1.18: Representation of liquid-phase exfoliation route. Adapted from Ref. 119.

nanosheets (at low production rate) with a predetermined number of layers (Figure 1.17b).[118] This production method is able to provide state-of-the-art material, characterized by the best quality in terms of cristallinity and opto-electronic properties, making it the first choice for fundamental research.[118] This is (unfortunately) counterbalanced by the low production rate (few nanosheets per hour), that makes this technique not suitable for industrial applications.

1.3.1.2 Liquid-phase exfoliation

Liquid-phase exfoliation (LPE) is widely used in the production of MX_2 nanosheets and quantum dots. It consist in the dispersion of the bulk powder in the appropriate solvent, followed by ultrasonication and size-selective centrifugation (Figure 1.18).[119–121] As demonstrated by the extensive work of Coleman *et al.*[120–122] this simple yet powerful technique permits to obtain high quality few-layer nanosheets at high rate; however it requires an extensive use of solvents and size-selective precipitation to isolate the final product. The ultrasonication produces cavitational bubbles in the solvent, whose collapse generates shock waves responsible for the exfoliation/fragmentation of the bulk material.[123] Generally, LPE method doesn't features surfactants, meaning that the exfoliated material can restack together into bulk if an appropriated solvent is not used.[124] In order to avoid the restacking process it is necessary a solvent which solubility parameter matches the one of the material,[125,126] resulting in a stable colloidal dispersion or, alternatively, the use of appropriate ligands. This method, possessing an high material output and being widely accessible, is one of the preferred method to obtain TMDs nanosheets. On the downside, this method is not able to produce single nanosheets, which makes it suitable for applications where monolayer thickness is not required.[118]

1.3.1.3 Chemical intercalation and exfoliation

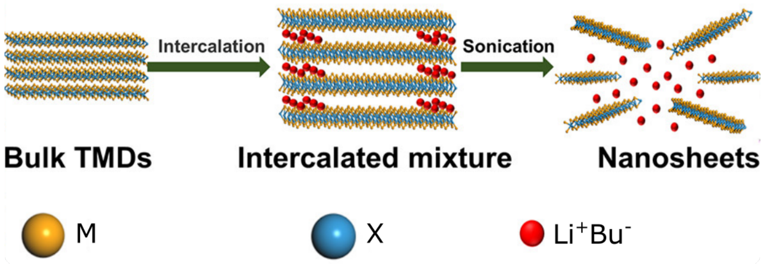

Figure 1.19: Representation of the chemical intercalation and exfoliation of bulk TMDs. Adapted from Ref. 127.

Intercalation of atoms or molecules between the stacked layers is another wide used technique to exfoliate TMDs. Alkali metals, polymers, and organometallic molecules are common intercalating agents;[128] however they can act as electron donors, transferring electrons to the metal's d orbital and triggering a phase transition from 2H-MX_2 to 1T-MX_2.[129] Among all different intercalating agents, lithium is one of the most used, due to its high reduction potential and high mobility in the interlayer space.[130] Organolithium compounds are often used in the intercalation process, such as *n*-buthyllithium and *tert*-buthyllithium; typically the MX_2 powder is immersed in $\sim$ 1.5 M *n*-buthyllithium solution in hexane for several days under inert atmosphere. The Li^+*n*-Bu^- specie reacts with the nanosheets, yielding to an electron transfer from the *n*-Bu^- to the nanosheet, forcing the Li^+ ions to intercalate to balance the charge. As a result, the interlayer gap expands, forming the Li_xMX_2. The exfoliation step is then achieved by the addition of water; it reacts with the the Li ions forming LiOH and H_2, which leads to the separation of the MX_2 layers.[131] Despite the possibility of producing high amounts of monolayer MX_2 (according to the extension of the intercalation), the major downsides are the necessity of an inert atmosphere and the polytype conversion, requiring an annealing post-treatment to restore the semiconducting phase.[132]

1.3.2 Bottom-up

1.3.2.1 Chemical Vapour Deposition

Chemical Vapor Deposition (abbreviated CVD) is the most widely bottom-up approach used in the synthesis of millimeter[134] and wafer-scale poly- and single-crystalline TMDs with high crystalline quality, scalable lateral size and thickness.[135,136] The system features a tube furnace, in which the metal (such as MO_x, MCl_5, metal films, metal hexacarbonyl $M(CO)_6$) and chalcogenide precursor reacts on the surface of a substrate at high temperature (from 150 °C to 600 °C depending on the chalcogen precursor), using Ar or N_2 as carrier gas[133] (Figure 1.20). Due to the 3-fold symmetry of MX_2, the growing process is characterized by the formation of triangular islands, that merges together forming a continuous film.[137] Studies on the formation of these islands in WS_2 growth revealed that the process starts with the formation of a small thick triangle formed by WO_yS_{2-y} and WS_{2+x}, where the metal species are in the +6 and +4 oxidation state.[138] The growth of further islands is promoted by the triangle apexes; the final result is the formation of a bigger island with WS_2

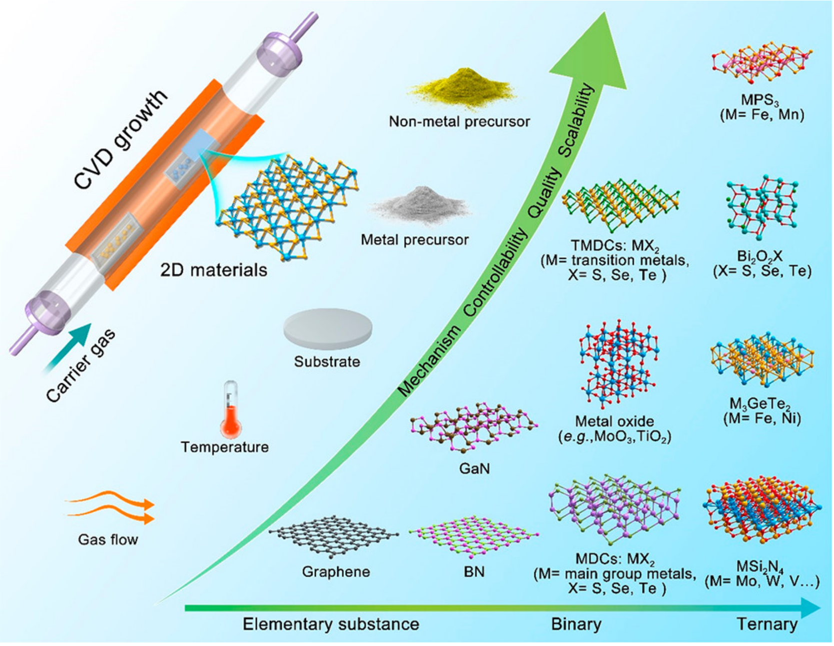

Figure 1.20: Schematic representation of the key parameters involved in the CVD growth of 2D materials. Reproduced from Ref. 133.

composition, with W in +4 oxidation state.

The lateral size of CVD grown MX$_2$ nanosheets is limited by the substrate size;[136] however the control over the thickness and film homogeneity is not trivial;[139] this is attributed to the lack of control over the initial deposition of the metal precursor a well as the poor diffusibility of the deposited metal atoms, causing the presence of unreacted metal atoms.[136] This has been partially overcome using H$_2$S as chalcogen precursor;[140] however the issue of disordered and small crystalline domain remains. These criticalities have been overcame by the metal organic chemical vapor deposition (MOCVD) and atomic layer deposition (ALD), in which the reaction is carried in using gaseous precursors, instead of relying on the *in situ* vaporization.[123,141] The use of gas-phase reagents allows an more efficient control on the precursor concentration (which is correlated to the partial pressure in the growth chamber), making the growth kinetic less sensitive to the substrate.[142] Carefully tuning the experimental parameter permits to obtain continuous monolayer films with grain size of 10 µm and well-stitched intergrain boundaries.[142] Differently than

MOCVD, ALD growth cycle alternates the feeding into the chamber of metal and chalcogen precursor (with a chamber purge between each step to remove unreacted precursor and prevent precursor mixing),[141] yielding to a precise control of the substrate coverage and film thickness during the growth, and producing high quality MX_2 films. This production method is widely used due to the possibility of thickness (and composition) control and the high quality of the produced nanosheets, plus the scalability of the method; however it requires expensive equipment as well as potentially dangerous chemicals, such as metal carbonyl precursors.

1.3.2.2 Colloidal synthesis

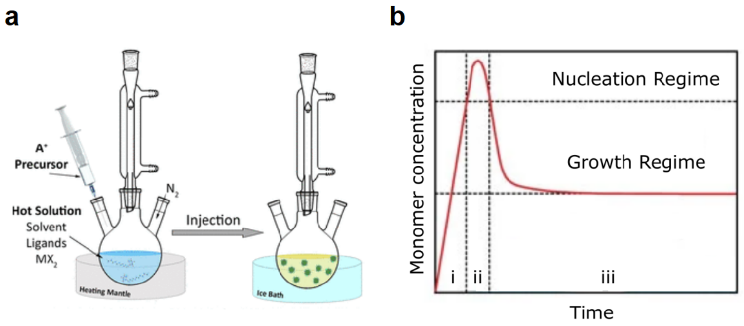

Figure 1.21: (a) Representation of a colloidal synthesis setup. Adapter from Ref 143. (b) Evolution of precursor concentration during typical hot-injection synthesis. Adapted from Ref. 144.

Colloidal synthesis is part of the wet chemical synthesis family, and involves chemical reactions in a liquid medium (water or organic solvents) at high temperature. Compared to the other wet chemical methods, colloidal synthesis are run at high temperature (typically $\sim$ 300 °C) for a short reaction time ($\sim$ 1h). The colloidal synthesis mechanism has been rationalized by LaMer and Dinegars model,[145] which involves (i) the formation of monomers in the solution, whose concentration arises above the supersaturation level, yielding to (ii) a saturation level at which the activation energy for nucleation can be overcome, starting the burst nucleation process that (iii) reduces the monomer concentration, ending the self - nucleation event (Figure 1.21). The nuclei enters in the growth stage, where no further nucleation events are triggered and the remaining monomers diffuse on the nuclei surface, promoting its growth. The nanocrystal size,[146] shape,[147,148] crystal phase,[149,150] dimensionality,[23] and properties[151] can be controlled adopting the appropriate ligand.[152,153] Ligands are able to influence the electronic structure of nanocrystals[154–156] (due to the high surface/volume ratio) as well as suppress surface traps, yielding to an increment of the photoluminescence.[69,151] The current state of the art of TMDs colloidal synthesis features several different pathways, such as slow injection method using metal halide or metal organic precursors such as $M(CO)_6$ (M = Mo, W),[157,158] colloidal sacrificial-conversion method using preformed metal oxide nanocrystals,[159] thermal decomposition of single-source precursor (such as $[(NH_4)_2MoS_4)])$[160] or $[(NH_4)_2MoO_4)]$ combined with a chalcogenide source.[161] Chalcogenide sources include elemental chalcogen powder in combination with a reducing agent such as oleylamine,[162] or more reactive species such as carbon disulfide (CS_2),[157] thiol ligands such as 1-dodecanthiol,[163] or chalcogen-containing molecules such as thioacetamide or diphenyl diselenide.[164–166] The effect of ligand and both metal and chalcogen precursors in the synthesis of TMDs have been deeply studied. Jin *et al.*, as an example, reported that the ratio between the metal precursor concentration ($W(CO)_6$) and the ligand concentration (trioctylphosphine oxide) is crucial for the lateral size control of WSe_2 2D-QDs[166] while Jung *et al.* studied the effects of different capping ligands on the anisotropic growth of MSe_2 (M = Mo, W) and on modulating the nanosheet number of layers, finding that an increase of such ratio yields to larger lateral dimensions.[165]Zhou *et al.* focused on the effect of Mo:S ratio on the nanosheets lateral size and the effect of precursors multi-injection on the nanosheet thickness,[164] displaying an increasing of lateral size while increasing the Mo:S ratio and an increasing of layer numbers increasing the number of precursor injections. Chalcogenide precursor reactivity has also been studied by Yoo *et al.*, displaying how highly reactive precursor such CS_2 ultimately yielded to multilayered structures while low reactive precursor such as 1-dodecanthiol ultimately yielded to monolayer nanosheets.[167] Despite being not widely used, colloidal synthesis is a valid method for the synthesis of TMDs, able to provide control over material thickness, composition, crystal phase, and shape (similarly to CVD method), with an high material output and the possibility of upscaling for industrial applications. On the downside, this method can't produce yet nanosheets with quality comparable to CVD method, which makes its choice as synthetic method less favorite in comparison to CVD.

1.4 Thesis Outline

This thesis is divided as follows:
In Chapter 2 we will discuss the colloidal synthesis of MoS_2 and $MoSe_2$, its optimization via Design Of Experiment approach and the resulting materials.
In Chapter 3 we will discuss the evolution of the synthetic protocol of MoS_2 to reduce its lateral size and the effect of the new protocol on the characteristics of the material.
In Chapter 4 we will move on from molybdenum-based TMDs to tungsten-based TMDs, translating the results obtained by the master student Diem Van Hamme on the synthesis of WS_2 on the colloidal synthesis of WSe_2.
Chapter 5 will discuss the preliminary results on the colloidal synthesis of $MS_xSe_{(2\text{-}x)}$ (M = Mo, W) alloys and $MoSe_2$/MoS_2 heterostructure.

2

Colloidal Synthesis of Fluorescent MoX_2 (X = S, Se) Nanosheets Via a Design Of Experiments Approach[1]

---

[1] *Partly adapted from:* **Pippia, G.**, Rousaki A, Barbone M. *et al.*; Colloidal Continuous Injection Synthesis of Fluorescent MoX_2 (X = S, Se) Nanosheets as a First Step Toward Photonic Applications. *ACS Applied Nano Material*, **2022**, 5, 8, 10311–10320

Author contributions

The findings in this chapter have been publishes in:
Colloidal Continuous Injection Synthesis of Fluorescent $\mathbf{MoX_2}$ (X = S, Se) Nanosheets as a First Step Toward Photonic Applications; **Gabriele Pippia**, Anastasia Rousaki, Matteo Barbone, Jonas Billet, Rosaria Brescia, Anatolii Polovitsyn, Beatriz Martín-García, Mirko Prato, Francesco De Boni, Marko M. Petrić, Amine Ben Mhenni, Isabel Van Driessche, Peter Vandenabeele, Kai Müller, and Iwan Moreels.
A. Rousaki performed the Raman measurements, R. Brescia provided the HR-TEM images and the diffraction pattern assignation, M. Prato and F. De Boni performed the XPS analysis, M. Barbone, M. M. Petrić, and A. Ben Mhenni performed the sample encapsulation and the cryo-photoluminescence spectroscopy on the sample. G. Pippia and I. Moreels wrote the manuscript.

2.1 Prologue

As described in Chapter 1, MoS_2 and $MoSe_2$ peculiar properties makes them technologically relevant and several synthetic strategies have been developed to achieve high-quality materials. Beside all the methods, wet chemistry can provide an high material production in the cheapest way; however it often yields to low quality material. In this Chapter we explore the colloidal synthesis of these two materials, the strategy applied in the optimization process and the resulting properties of the optimized samples.

2.2 Introduction

The colloidal synthesis of MoS_2 and $MoSe_2$ have been widely explored, with several different strategies reported in literature;[23, 160, 165, 168–173] however no photoluminescence is reported for materials obtained via colloidal route. This depends on the quality of the material itself, that (in case of colloidal synthesis) is affected by different critical issues, such as multilayer thickness, presence of mixed 1T/2H phase, and surface defects. In order to minimize this is necessary a methodic study of the synthesis optimization, to find the best combination of factors that can yield to materials with superior properties. In our study we apply the Design of Experiment method for a statistical study of the parameters involved in the synthesis protocol, assess their statistical relevance in the system, and build a prediction model of the effect on the system of the reaction parameters. Using the acquired knowledge, we then proceed on the final optimization of the sample, obtaining MoS_2 nanosheets that displays superior qualities, with a thickness distribution of 1-2 layer thickness, and photoluminescent properties at both cryogenic and room temperature. Finally, we translate the MoS_2 protocol on the synthesis of $MoSe_2$ nanoflowers, obtaining a material that, similar to MoS_2, shows superior qualities, monolayer thickness, and photoluminescence at room and cryogenic temperature.

2.2.1 Design of Experiment: an overview

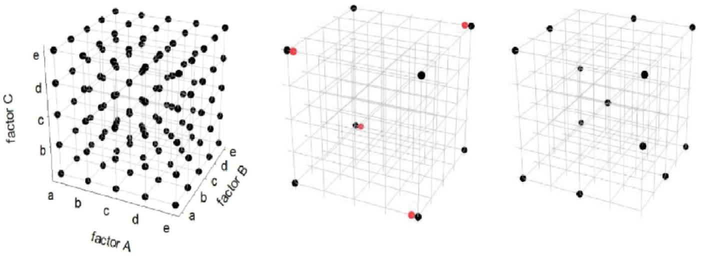

Full factorial Design (FD)

Plackett-Burman Design

Definitive Screening Design (DSD)

Figure 2.1: Representation of Full factorial Design, Plackett-Burman design, and Definitive Screening Design for $k = 3$. The lines intersections represent the possible combinations of the factors, while the black dots represents the investigated combinations. For the Plackett-Burman design, the red dots are tests repeated on some combinations to reach the minimum number of tests according to the specific design. Adapted from Ref. 174.

Optimizing a process is a well-known time consuming task usually based on trial-and-error approach, called One Variable At the Time (OVAT) approach. In simple terms, the OVAT approach is an iterative approach based on changing the variable of a process while keeping the other ones constant and evaluate the change in the outcome. Clearly, more variables are involved in the process, more experimental runs are needed to find the right combination of factors that yields to an improvement of the process. An alternative to this (standard) approach is given by the Design of Experiment (DOE), a statistical method created more than 80 years ago by Fisher for the agricultural industry.[175] As general concept, DOE method has the purpose to find the correlation between the factors k involved in a process and the outcome (*i.e.*, response) of the process itself via statistical analysis, using a set of controlled experiments. The first DOE design is the Full Factorial Design (FD), a type of design based on the combination of all the factors involved in a process;[175] since then new types of design have been made, such as the fractional factorial design,[176] the Plackett-Burman design,[177] the optimal design,[178] the definitive screening design (DSD)[179] to cite few of them. Each design differs for the number of experimental runs required to extract the impact of the factor on the response, going from 2^k for the full factorial design to the $2k + 1$ for the definitive screening design,[174] and only recently literature have started to give some guidelines about the design choice for an optimal application.[174, 180] Different designs takes into account different effects of the factors on the responses. As an example, FD design considers only the main effect and the two factors interaction on the response while different designs such as DSD are able to consider the quadratic effect of the factors in the response. The ability of DOE of evaluating the effect of the single factors as well as the effect of combinations of factors on the response evolution permits to acquire, compare to the classic OVAT approach, wider knowledge about the system using less experimental points. Furthermore, the use of DOE permits a mathematical modelling of the system via linear regression model, considering the main factors, two-factors combination and quadratic effect in the process.[180, 181] DOE designs can be coupled to the Response Surface Methodology (RSM), that can be used to expand the regression equation. It is based on the assumption that the response function (*i.e.*, surface) can be approximated by a Taylor expansion series and that the surface curves around the optimal point, requiring the incorporation of cross products terms into the equation (Equation 2.1).[174]

$$Y_i = \beta_0 + \sum_{j=1}^{m} \beta_j X_{i,j} + \sum_{j=1}^{m-1} \sum_{k=j+1}^{m} \beta_j k X_{i,j} X_{i,k} + \sum_{j=1}^{m} \beta_j j X_{i,j}^2 + \epsilon_i \tag{2.1}$$

where Y_{i} is the response variable in the i^{th} experiment, $\mathrm{X}_{\mathrm{i,j}}$ is the j^{th} factor on the same i^{th} experiment, m represents the number of factors, β_0 to β_{mm} are the model coefficients, and ϵ_i is the random error. In particular the DSD design, developed in 2011 by Jones and Nachtsheim, is capable of analysing the influence of different input factors within a predefined reaction space, using the fewest experimental runs.[179, 180] This design is an orthogonal three-level design, able to accommodate several factors with fewer runs,[179, 182] with a number of runs equals to $2k + 1$ with k as number of factors, showing high accuracy;[180] however to avoid performance degradation a minimum of 13 runs are recommended.[180] The limited number of runs required by the DSD design makes it suitable for the screening of several factors at the same time, to individuate the main factors involved in the process. To shed some light, several articles about the different designs (such as full and fractional factorial design, Taguchi design, Plackett-Burman design, central composite design) have been published recently, comparing the different designs and their performance on different study cases.[174, 180, 183] From these studies, DSD design have been indicate as valid alternative to other designs for system featuring an high number of factors, since it is able to accurately estimate not only main factors and two-factors interactions, but also quadratic effects present in the system, something not possible with all designs.[180] Moreover, DSD requires a low number of experimental runs compared to the other designs, making it intrinsically more efficient if compared to other designs. DSD (and in general all different DOEs) required some previous knowledge about the target system. This step is crucial for the success of the DOE; in fact a sufficient knowledge of the system permits to recognize all potential factors involved in the process, yielding to a more effective screening and to a more successful outcome. DOEs factors are screened only for limited values of ranges chosen by the user; this determines the factor space (and response space) that will be accessible by the design and its efficiency on finding the optimal response.

2.3 Experimental Results

Materials. Molybdenum pentachloride ($MoCl_5$, 99.99%, Sigma-Aldrich), elemental sulfur ($\geq$ 99.95%, Sigma-Aldrich) and selenium ($\geq$ 99.99%, Strem Chemicals), 1,2-dichlorobenzene (*o*-DCB, 99%, Acros Organics) and chloroform are used without any purification. 1-octadecene (ODE, Sigma-Aldrich) and oleylamine (OLA, 80-90% Acros Organics) are dried using calcium hydride, distilled and stored under nitrogen until further use.

General DOE 2H-MoS_2 Synthesis. The synthesis is performed under nitrogen using standard Schlenk line techniques. All amounts and temperatures used are mentioned in Table 2.1. As an example, in a 25 mL three-neck flask, a solution of OLA and sulfur is degassed under vacuum. After degassing, the temperature is raised and a solution of $MoCl_5$ in ODE (0.05 g in 3 mL of ODE, sonicated until complete dissolution) is injected using a syringe pump. After 1 h, the MoS_2 solution is cooled and the product is purified three times using a mixture of hexane/isopropanol, toluene/isopropanol and dichlorobenzene/isopropanol respectively, followed by centrifugation at 5000 rpm to collect the sample. The nanosheets are finally dispersed in *o*-DCB.

Optimized 2H-MoS$_2$ Nanosheet Synthesis. The synthesis is performed under nitrogen using standard Schlenk line technique. In a 25 ml three-neck flask a solution of OLA (15 mL) and sulfur (41 mg) is degassed under vacuum (120 °C, 150 min). After degassing, the temperature is raised up to 300 °C and a solution of MoCl$_5$ in ODE (0.017 g in 1 mL, sonicated until complete dissolution) is injected at 9 mL h^{-1} using a syringe pump. After injection, 10 mL of fresh OLA from the glovebox is injected in the MoS$_2$ solution and a water bath is used to cool it. The product is purified as described above, and finally dispersed in *o*-DCB.

Optimized 2H-MoSe$_2$ Nanosheet Synthesis. The synthesis is performed under nitrogen using standard Schlenk line techniques. In a 25 ml three-neck flask, a solution of OLA (15 mL) and selenium (10 mg) is heated up to 290 °C and a solution of MoCl$_5$ in ODE (0.017 g in 1 mL, sonicated until complete dissolution) is injected at 12 mL h^{-1} using a syringe pump. After the injection, the solution is cooled using a water bath. The product is purified three times using a mixture of toluene/isopropanol/acetone, hexane/isopropanol and chloroform/isopropanol respectively, followed by centrifugation at 5000 rpm to collect the sample. The nanosheets are finally dispersed in chloroform.

Characterization methods. Samples for transmission electron microscopy (TEM) were prepared by drop-casting of a suspension onto ultrathin C/holey C/Cu TEM grids. High resolution transmission electron microscopy (HR-TEM) images were acquired on an image-Cs-corrected JEM-2200FS TEM (JEOL), operated at 200 kV. Bright-field TEM images were acquired on a JEOL JEM-1011 microscope operating at an accelerating voltage of 100 kV. Raman spectra were collected with a Bruker Optics “Senterra” dispersive Raman spectrometer. The spectrometer is coupled to an Olympus BX51 microscope and to a thermoelectrically cooled charge coupled device (CCD) detector, operating at -65 °C. The point measurements were conducted on dried droplets on glass slides and by using the 532 nm laser of the Raman system. The experimental conditions selected were as follows: 5 or 10 accumulations of 10 s, 3–5 cm^{-1} spectral resolution, 40–1540 cm^{-1} spectral range, 50 µm pinhole-type aperture, ×50 (NA: 0.75) magnification objective (corresponding to a less than 4 µm spot size) and a 0.20% laser power (corresponding approx. to 0.12 mW). Ultraviolet–Visible (UV-Vis) absorption spectra of MoS$_2$ nanosheets in *o*-DCB (chloroform for MoSe$_2$) were recorded using a PerkinElmer Lambda 950 spectrometer using a 1 cm path length quartz cuvette. Photoluminescence spectra were measured using a custom-made confocal microscope in backscattering geometry. To encapsulate the colloidal MoS_2 nanosheets, a MoS_2 suspension was spin-coated on a Si/SiO_2 chip with previously exfoliated hBN (HQgraphene). A second hBN sheet was transferred on top of selected bottom hBN crystals by means of a conventional dry-transfer method.[184] The excitation laser beam is focused on the sample by an objective with numerical aperture NA = 0.75 to a diffraction-limited spot. For cryogenic measurements, a He-flow cryostat (Cryovac) was used, and the emitted light was directed to a spectrometer (Horiba, 300 grooves/mm) coupled to a nitrogen-cooled CCD. XPS analyses were carried out using a Kratos Axis UltraDLD spectrometer. Data were acquired using a monochromatic Al Kα source, operated at 20 mA and 15 kV. High resolution spectra were acquired at pass energy of 20 eV, energy step of 0.1 eV, and take-off angle of 0° with respect to sample normal direction.

2.3.1 General Colloidal Synthesis Protocol

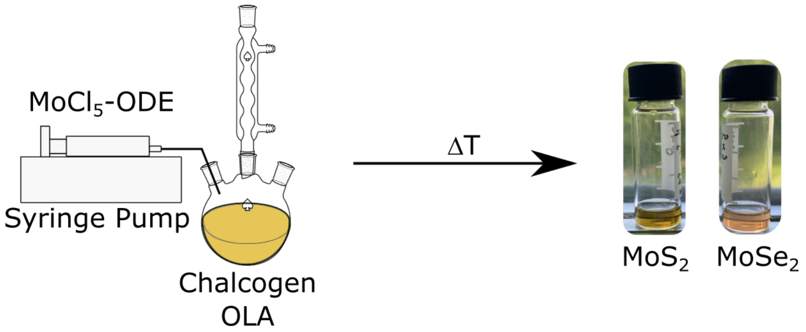

Figure 2.2: Schematic representation of the reaction protocol used in this work.

The general colloidal synthesis protocol used for the synthesis of MoS_2 and $MoSe_2$ nanosheets features the slow injection of a metal chloride ($MoCl_5$) - 1-octadecene (ODE) solution in a hot solution of oleylamine (OLA) and elemental chalcogen under inert atmosphere (Figure 2.2). OLA is used in colloidal synthesis of nanoparticles and TMDs as capping ligand and mild reducing agent;[162] in fact a mixture of OLA and elemental sulfur can react with metal precursors leading to metal disulfide nanocrystals, and a similar effect is reported for OLA and selenium mixtures. A high reaction temperature is required to overcome the energy barrier of ∼ 400 meV between the two phases,[185] and to achieve the 2H polytype.

2.3.2 Definitive Screening Design Setup

For the synthesis optimization we used the DSD design since it requires the lowest number of experimental runs (as explained in section 2.2.1). In our experiments, we kept the molybdenum precursor concentration, ODE volume, and total reaction time constant to keep the design relatively simple. We chose to vary six input factors: reaction temperature (X_1), sulfur concentration, (X_2) precursor injection rate (X_3), OLA volume (X_4), OLA degassing time (X_5), and OLA degassing temperature (X_6) (Table 2.1). The first three factors were chosen as they may directly impact the nanosheet growth and final crystal phase.[132, 186, 187] In addition, the amount of OLA may be linked to the colloidal stability in solution[188] and an *in situ* H_2S formation,[162] while the OLA degassing temperature and time are expected to influence the concentration of oxygen and water in the reaction environment. The factor ranges (Table 2.1) used for DSD design were based on initial syntheses and available literature data. These ranges are crucial for the good success of the design; in fact it is necessary that all (or at least most of) the experiments have a successful outcome, *i.e.,* there are sufficient experimental data to include in the analysis. For the DSD, we executed a total of 13 experiments, and for each run we collected seven aliquots to monitor the evolution of the samples over time.

Table 2.1: Input factors X_i (i = [1,6]) used for the syntheses, and associated S/Mo molecular ratio[2]

Run no.	X_1 [°C]	X_2 [mL]	X_3 [mmol]	X_4 [mL·h^{-1}]	X_5 [°C]	X_6 [min]	S/Mo ratio
1	300	15	3.75	6	160	150	20.5
2	300	3	2.25	3	100	30	12.3
3	320	9	2.25	6	160	30	12.3
4	280	9	3.75	3	100	150	20.5
5	320	3	3	3	160	150	16.4
6	280	15	3	6	100	30	16.4
7	320	15	2.25	4.5	100	150	12.3
8	280	3	3.75	4.5	160	30	20.5
9	320	15	3.75	3	130	30	20.5
10	280	3	2.25	6	130	150	12.3
11	320	3	3.75	6	100	90	20.5
12	280	15	2.25	3	160	90	12.3
13	300	9	3	4.5	130	90	16.4

---

[2] X_1: Reaction temperature, X_2: OLA volume, X_3: Sulfur concentration, X_4: Injection rate, X_5 degassing temperature, and X_6: Degassing time.

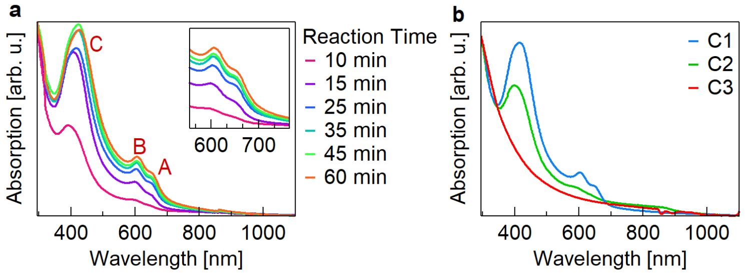

Figure 2.3: (a) Sample evolution during synthesis (synthesis run no. 1). Aliquots were taken between 10 and 60 min. A, B, and C mark the different features that can be observed when synthesizing 2H-MoS_2. Inset: zoom into the band gap region. (b) Representative absorption spectra of the three categories to which the DOE synthesis runs can be allocated. (C1: run no. 12, C2: run no. 10, C3: run no. 5). C1 corresponds to 2H-MoS_2, C2 to a mixture of 2H and 1T, and C3 to 1T MoS_2.

2.3.3 Characterization of DSD experimental runs

All samples are first characterized using UV-Vis spectroscopy, a common technique used for either polytype determination and thickness estimation. As explained in section 1.2.3, 1T and 2H polytype are characterized by a different electronic structure that translates, for 1T-MoS_2, in a featureless UV-Vis absorption spectrum, characterized by a monotonic increasing in absorption[189] while 2H-MoS_2 displays three distinctive absorption features. Taking as example the absorption spectrum of the aliquots of synthesis run no. 1, we see the appearance of three absorption (A, B and C) peaks after 10-15 min of reaction (Figure 2.3a), characteristic for the formation of semiconductor 2H-MoS_2. Longer reaction times yields to a progressive red shift (*i.e.*, shift towards lower energies) of these features (Figure 2.3a). This shift is thickness and area-dependent[23,47] and it can be used to determine nanosheet thickness and size.[122]

Initial inspection of the spectra of the final sample of all runs, taken after 60 min of reaction (Figure 2.4), shows that they can generally be categorized in three different sets, by the exciton peak sharpness: category C1 includes all samples when all the excitonic (A, B) transitions are well defined; category C2 contains the samples where only the C absorption peak is well defined, while C3 category includes all samples where no absorption features are recognizable (Figure 2.3b).

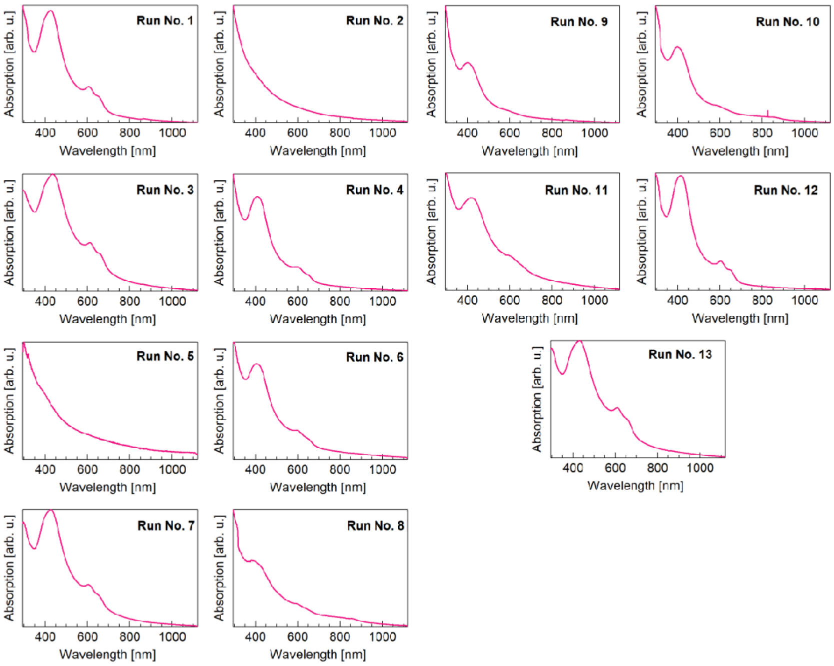

Figure 2.4: UV-Vis spectra of all the 60 min aliquots used in the DSD design.

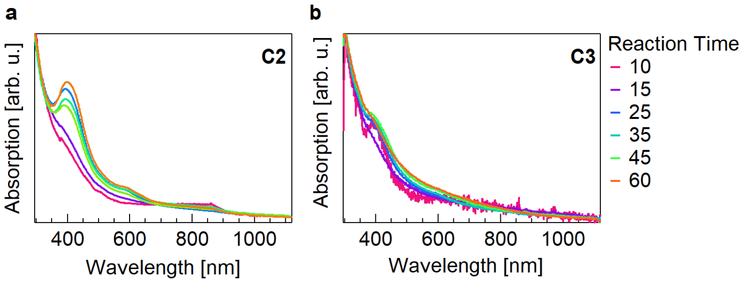

Figure 2.5: UV-Vis absorption spectral evolution of sample C2 (a) and C3 (b)

A close look on the C2 and C3 sample temporal evolution (Figure 2.5) shows for category C2 a similar trend of C1 (Figure 2.3a), with the first aliquots displaying a featureless spectrum that evolves similarly to C1, with broader A and B features. On the other hand, C3 sample displays only a featureless spectrum for all the aliquots, typical of 1T-MoS$_2$.

We further investigate the nature of sample C1 and C3 using X-ray photoelectron spectroscopy (XPS). This technique is able to probe the chemical environment surrounding a specific atom, *i.e.*, determine its chemical state. In case of TMDs, XPS is able to distinguish the different chemical state of metal and chalcogenide in metallic and semiconducting polytype (Figure 2.6).[32]

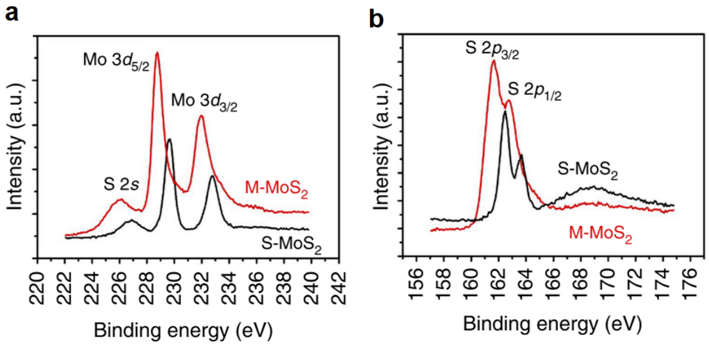

Figure 2.6: XPS spectra of Mo 3d (a) and S 2p (b) for metallic (M) MoS$_2$ and semiconducting (S) MoS$_2$. Adapted from Ref. 32.

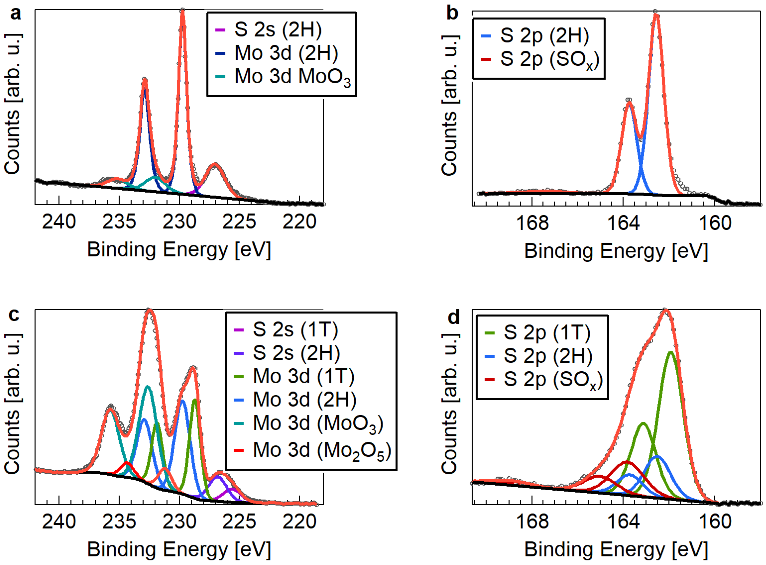

Figure 2.7: XPS spectra of Mo 3d and S 2p regions of sample C1 (a, b), and sample C3 (c, d). Sample C1 is representative of the 2H polytype, displays only the signals associated to this polytype while sample C3 (c and d) are characterized by the presence of both polytype with a 2H:1T ratio of 56.7:43.1 as well as a stronger signals associated to molybdenum oxides.

From the XPS spectra reported in Figure 2.7 we can see that sample C1 shows only the presence of the semiconducting polytype as well as the presence of oxides (Figure 2.7a and b) while sample C3 (Figure 2.7c and d) displays a high metallic polytype component as well as the presence of different oxides defects. We can then conclude that the synthesis parameters influence not only the nanosheet dimensions but also the crystal structure, where the 2H phase is obtained running the reaction at 300°C using a large excess of sulfur and OLA.

Table 2.2: Responses Y_i retrieved from the DOE experiments.

Run no.	A exciton position [nm]	Background scattering	Absorption sharpness	Type
1	657	0.262	1.09	C1
2	665	0.608	0.91	C3
3	664	0.352	1.05	C1
4	654	0.350	1.01	C1
5	665	0.713	0.93	C3
6	652	0.418	1.00	C2
7	659	0.361	1.03	C1
8	650	0.579	0.95	C3
9	643	0.498	0.87	C2
10	642	0.568	0.93	C2
11	659	0.500	1.00	C2
12	653	0.228	1.11	C1
13	661	0.330	1.06	C1

2.3.4 DSD modelling

In order to statistically analyze the results, it is necessary to introduce some metrics to evaluate the quality of the synthesized nanosheets. In an ideal synthesis the MoS$_2$ nanosheets are only a monolayer thick, of uniform dimensions, and with acceptable lateral sizes and dispersibility in the final solvent. These requirements are represented by a minimized wavelength for the A exciton absorption (due to the correlation between band gap energy and number of layers),[46, 190] spectrally narrow absorption peaks (absorption peaks of different thicknesses overlaps showing a broader peak as a result), and a low scattering background (large and/or aggregated nanosheets increases the scattering contribute in the absorption spectrum),[191] respectively. We therefore decided to optimize these three responses Y_i (i = 1, 2, 3) of the final material. The scattering background is represented by the ratio of the absorbance at 750 nm and the absorbance at the position of the A exciton. The spectral position of the A exciton is calculated by second derivative analysis, after subtracting the scattering background from the spectra, subtracting from all the spectrum the absorbance value at 1120 nm. For the absorption peak linewidth we use the ratio of the maximum peak absorbance at the spectral position of the B exciton transition and the absorbance at the following local minimum, which lies at slightly higher energy, as a proxy. We rely on the B exciton transition, as it is more pronounced that the A exciton transition (Figure 2.3a). A full overview of all responses Y_i is shown in Table 2.2. These responses are fitted to a quadratic surface, *i.e.*, the fit considers both linear and quadratic dependencies on input factors, X_i, ${X_\mathrm{i}}^2$, and $X_\mathrm{i}{\cdot}X_\mathrm{j}$. Importantly, the model yields a p-value for each input factor, *i.e.*, an indication of the probability that the observed data comes from the null hypothesis, in this case that there is no correlation between the observed values and the factors. A threshold of 0.05 is typically chosen; if the p-value is below this threshold then the null hypothesis has to be rejected, *i.e.*, there is no influence of the respective factor on the responses. For each Y_i, the model then finally yields an expression that predicts Y_i from the input factors (X_i, ${X_\mathrm{i}}^2$, $X_\mathrm{i}{\cdot}X_\mathrm{j}$) that are statistically relevant.

Table 2.3: Coefficients and associated p-values of the main interaction factors, two-factors interactions and quadratic effects for A exciton position.

	Factor	p-value
$X_1 \cdot X_2$	Reaction T · OLA volume	0.00006
$X_1 \cdot X_3$	Reaction T · Sulfur concentration	0.00010
X_1	Reaction T	0.00022
${X_1}^2$	Reaction T · Reaction T	0.00052
X_3	Sulfur concentration	0.00666
X_2	OLA volume	0.01363

2.3.4.1 A exciton modelling

For the analysis of the A exciton position λ_A, six factors have been identified as statistically relevant: reaction temperature (X_1), OLA volume (X_2) and sulfur concentration (X_3), as well as the combinations, ${X_1}^2$, $X_1 \cdot X_2$ and $X_1 \cdot X_3$. The associated p-value of each factor is reported in Table 2.3. The modelling yields to the following expression:

$$\begin{aligned}\lambda_A = 661 + 3.9\cdot(\frac{(X_1-300)}{20}) - 1.7\cdot(\frac{(X_2-9)}{6}) - 2\cdot(\frac{(X_3-3)}{0.75})\\ -6.9\cdot(\frac{(X_1-300)}{20})^2 - 5.667\cdot(\frac{(X_1-300)}{20})\cdot(\frac{(X_2-9)}{6})\\ -5.167\cdot(\frac{(X_1-300)}{20})\cdot(\frac{(X_3-3)}{0.75})\end{aligned} \tag{2.2}$$

The Equation 2.2 can give some insights into the response of the A exciton position upon variation of the different input factors. An increase in reaction temperature leads to a red shift of the A exciton position, while an increase of the chalcogen and ligand concentrations results in a blue shift (*i.e.*, a shift towards shorter wavelength). Hence, a reduced reaction temperature, in combination with high concentrations of OLA and chalcogen precursors are ideal conditions to obtain thin samples, with a blue shifted A exciton peak. At the same time, the precursor injection rate, OLA degassing time, and OLA degassing temperature have no significant impact on the peak position.

2.3.4.2 A exciton sharpness modelling

Absorption sharpness analysis yields to 4 factors, divided in three main factors (OLA volume, reaction temperature and injection rate) and a two-factors interaction (reaction temperature·precursor injection rate). The model shows a low R^2 (0.72) and a p-value of 0.0243, making it statistically significant but with poor fitting capacity. Of the 4 factors (reported with the respective coefficient in Table 2.4), two are greatly above the p-value threshold , however they are kept due to heredity effect. The prediction expression is reported in Equation 2.3.

$$\begin{aligned}S = 0.997 + 0.013\cdot(\frac{(X_1-300}{20})) + 0.039\cdot(\frac{(X_2-9}{6}))\\ +0.023\cdot(\frac{(X4-4.5)}{1.5})\\ +0.054\cdot(\frac{(X1-300)}{20})\cdot(\frac{(X4-4.5)}{1.5})\end{aligned} \tag{2.3}$$

Table 2.4: Coefficients and associated *p*-values of the main factors and two-factor interactions for the peak sharpness.

	Factors	p-value
$X_1 \cdot X_4$	Reaction T · Injection rate	0.0120
X_2	OLA volume	0.0306
X_4	Injection rate	0.1605
X_1	Reaction T	0.4177

As visible in 2.3), all factors have little effect on the increase of peak sharpness, with the reaction temperature having the smallest effect. However, due to the positive coefficient of all factors, an increase of their values yields to and increase of peak sharpness.

2.3.4.3 Background scattering modelling

The scattering background depends on the OLA volume, precursor injection rate, reaction temperature, OLA degassing temperature and OLA degassing time, as well as the two-factor interaction reaction temperature·precursor injection rate and two quadratic dependencies of reaction temperature and OLA degassing temperature (Table 2.5). As the previous case, two factors shows a p-value higher than 0.05, however they are kept in the prediction model due to heredity effect. The prediction expression is reported in Equation 2.4

Table 2.5: Coefficients and associated p-values of the main factors and two-factor interactions for the background scattering.

	Factors	p-value
X_2	OLA volume	0.00009
$X_1 \cdot X_4$	Reaction T · Injection rate	0.00031
X_4	Injection rate	0.01678
X_1	Reaction T	0.02007
${X_5}^2$	Degassing T · Degassing T	0.03049
${X_1}^2$	Reaction T · Reaction T	0.04413
X_6	Degassing time	0.05637
X_5	Degassing T	0.23928

$$
\begin{aligned}
B = 0.363 + 0.028 \cdot (\frac{(X_1 - 300)}{20}) - 0.120 \cdot (\frac{(X_2 - 9)}{6}) \\
-0.030 \cdot (\frac{(X_4 - 4.5)}{1.5}) - 0.010 \cdot (\frac{(X_5 - 130)}{30}) \\
-0.020 \cdot (\frac{(X_6 - 90)}{60}) + 0.046 \cdot (\frac{(X_1 - 300)}{20}) \cdot (\frac{(X_1 - 300)}{20}) \\
-0.111 \cdot (\frac{(X_1 - 300)}{20}) \cdot (\frac{(X_4 - 4.5)}{1.5}) \\
+0.059 \cdot (\frac{(X_5 - 130)}{30}) \cdot (\frac{(X_5 - 130)}{30})
\end{aligned}
\tag{2.4}
$$

The prediction model 2.4 features many different factors; a quick look revels that an increase of reaction temperature and degassing time yields to an increase on the background scattering. On the other hand, increasing the other factor values yields to a reduction of the background scattering.

2.3.5 Testing the prediction model

The prediction of the model is tested running a synthesis with parameters that are optimized toward a maximal blue shift of the A exciton position, a reduced Rayleigh scattering background, and sharp absorption features. The model proposed the following reaction conditions: a reaction temperature of 280 °C, OLA volume of 9 mL, sulfur concentration of 2.26 mmol, an OLA degassing time and temperature of 150 min at 160 °C, and a precursor injection rate of 6 mL·h^{-1}. From this synthesis we acquired aliquots at the end of the reaction (60 min) and at the end of the injection of the Mo precursor (30 min). The experimental responses are compared to the predicted ones in Table 2.6.

Table 2.6: Comparison between predicted responses from DOE and experimental responses.

	A exciton position [nm]	Background scattering parameter	Peak sharpness
Predicted results	647 ± 1	0.49 ± 0.02	0.98 ± 0.03
Experimental results (30 min reaction)	653	0.40	1.03
Experimental results (60 min reaction)	654	0.50	0.95

We can observe that the experimental value of the A exciton position is close to the predicted value. Note that this prediction was based on all values for the A exciton position, including those below 650 nm (see Table 2.2). In hindsight (cfr. below), these values (run no. 9 and run no. 10) show an A exciton position below the one expected even for a monolayer sample; however, during the DOE run we did not discriminate between values, yielding a slightly underestimated prediction compared to what can be obtained experimentally even for a monolayer. The background scattering parameter prediction and peak sharpness are accurate for the 60 min aliquot. In conclusion, our model is able to predict the experimental conditions for which the thinnest possible MoS_2 nanosheet sample can be synthesized. Regarding the evolution of the sample during reaction, the A exciton peak position merely red shifts by 1 nm between 30 min and

60 min, indicating no further growth in thickness after the end of the precursor injection. The background scattering does further increase, suggesting a continued lateral growth of the nanosheets. This is accompanied by a decrease in peak sharpness. This outcome was used as a basis to make a final improvement of Y_{i}.

The final protocol features the slow injection (9 mL h^{-1}) of a solution of $MoCl_5$ (17 mg) dispersed in 1 mL of ODE into an hot solution (300 °C) of OLA (15 mL) and elemental sulfur (41 mg), degassed for 150 min at 120 °C under vacuum. The obtained sample, after three purification steps (using a mixture of hexane/isopropanol, toluene/isopropanol and dichlorobenzene/isopropanol respectively, followed by centrifugation at 5000 rpm to collect the sample), have been redispersed in *o*-DCB and characterized. We obtained a sample with A exciton absorption at 653 nm (Figure 2.8a), a background scattering parameter of 0.35, and a peak sharpness of 1.06, indeed slightly improving on the previous sample (Table 2.6). The latter corresponds to a full width at half maximum (FWHM) of 36 nm. As LPE literature typically reports A exciton positions around 660 nm, pertaining to mixtures of different thicknesses,[122, 192, 193] we are clearly superseding the state-of-the-art in solution-based TMDs. We then proceeded to a further experimental study of the samples. High resolution transmission electron microscopy (HR-TEM) images of the sample were acquired by our collaborator in IIT (Istituto Italiano di Tecnologia) to evaluate the crystal phase (Figure 2.8b). Via Fast Fourier Transform on the HR-TEM image it is possible to retrieve the diffraction pattern of the nanosheets, which can be used to assign the corresponding crystal phase of the sample. HR-TEM and its Fast Fourier Transform (FFT, Figure 2.8c) clearly confirms the 2H-MoS_2 semiconducting polytype phase, similar to what reported for samples obtained via LPE.[193]

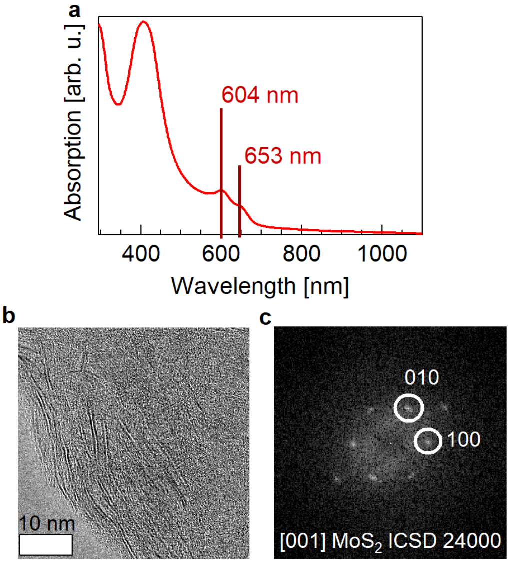

Figure 2.8: (a) UV-Vis absorption spectrum of MoS$_2$ nanosheets prepared via the optimized synthesis, including A and B exciton positions. (b) High Resolution TEM image of MoS$_2$. (c) FFT of the HR-TEM image, indexed as [001]-oriented semiconducting MoS$_2$ (MoS$_2$-4H, ICSD 24000).

To assess the MoS$_2$ thickness, we used Raman spectroscopy. This technique is used in thickness and polytype determination, as metallic and semiconducting polytypes are characterized by different Raman modes (Figure 2.9a). Specifically, the semiconducting polytype is characterized by the presence of two first-order intralayer phonon modes specific Raman modes, $E^1{}_{2g}$ (corresponding to the in-plane vibrational mode) and A_{1g} (corresponding to the out-of-plane vibrational mode) (Figure 2.9b) which position is thickness-dependent, probably due to a change in the long-range Coulomb interactions changing the number of layers.[194] In the optimized MoS$_2$ (Figure 2.10a) the two modes lie at 405.2 cm^{-1} and 384.5 cm^{-1} respectively (Figure 2.8a) while the FWHM of the modes amounts to 5.5 cm^{-1} and 6.6 cm^{-1} for $E_{2g}{}^1$ and A_{1g} respectively. In a highly crystalline sample these values are around 2.1 - 2.7 cm^{-1} and 3 cm^{-1} for $E_{2g}{}^1$ and A_{1g} respectively.[194, 195] A further broadening is usually observed in defective MoS$_2$.[196] Support for these defects can be observed via vibrational modes at 227 cm^{-1} and 996 cm^{-1}, related to sample disorder[196] or the

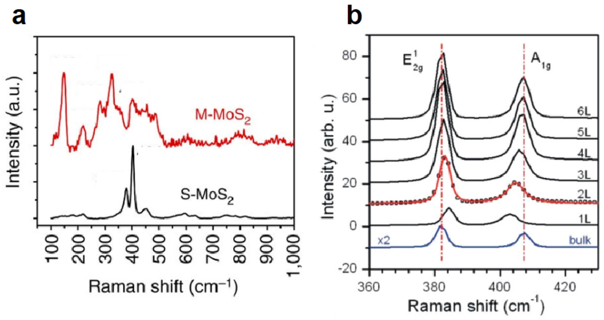

Figure 2.9: (a) Raman spectra of 1T-MoS_2 (red trace) and 2H-MoS_2 (black trace). Adapted from Ref. 32. (b) Evolution of Raman modes position with number of layers. Adapted from Ref. 194. Copyright 2010 American Chemical Society.

presence of MoO_3, respectively;[197] however, the suppressed mode at 996 cm^{-1} suggest the presence of vacancies rather than MoO_3 (Figure 2.8a).[196] As introduced before, the two Raman modes are sensitive to the MoS_2 thickness. Literature data shows that, going from bulk to a monolayer, $E_{2g}{}^1$ blue shifts (stiffens) while A_{1g} red shifts (softens), yielding a frequency spacing of 25 cm^{-1} for bulk that decreases to 21.3±1.2 cm^{-1} for a bilayer and 18.9±1.2 cm^{-1} for a monolayer (Figure 2.10b).[194, 198–201] The ranges for the mode spacing reported in literature prevents a quantitative assessment of number of layers present in our sample, however, from an average mode spacing of 20.8±0.2 cm^{-1} of our optimized sample, we can estimate that we indeed synthesized a sample that consists at the most of a mixture of mono- and bilayer nanosheets. This is consistent with the A exciton position lying at 653 nm, which is close to the value of 650 nm reported in literature for a MoS_2 monolayer.[202]

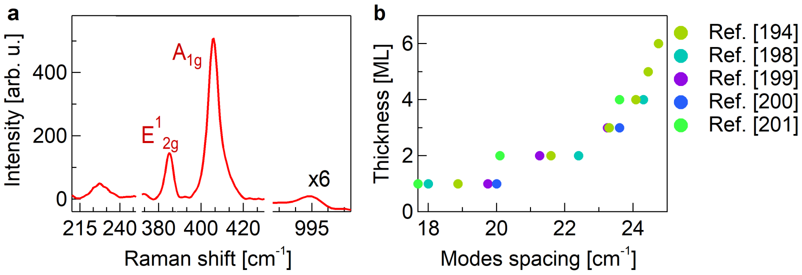

Figure 2.10: (a) Raman spectrum (excitation wavelength of 532 nm) of optimized MoS_2 sample, indicating $E_{2g}{}^1$ and A_{1g} modes of colloidal 2H-MoS_2 at 405 cm^{-1} and 384 cm^{-1}. The mode at 227 cm^{-1} is associated to sample disorder, while a minor contribution from a MoO_x mode can be observed at 996 cm^{-1}. (b) Correlation between $E_{2g}{}^1$ and A_{1g} mode spacing, and number of layers, using literature data.[194, 198–201]

2.3.6 From MoS_2 to $MoSe_2$

To demonstrate the general applicability of our synthesis approach, the optimized protocol from the MoS_2 synthesis was further adapted to the synthesis of 2H-$MoSe_2$. In order to reduce the number of input factors involved, the degassing step involving OLA and chalcogen was removed, instead using distilled OLA stored over molecular sieves in a glovebox. For the synthesis, we set the reaction temperature to 290°C, using an injection rate of 12 mL h^{-1} and 10 mg of elemental selenium as chalcogenide precursor; all the remaining parameters were kept the same, as well as the purification procedure. The resulting nanosheets displays two excitonic absorption peaks, here red shifted compared to MoS_2 due to the smaller $MoSe_2$ band gap. As shown by the TEM image (Figure 2.11a, inset), our $MoSe_2$ adopts a nanoflower morphology. HRTEM images and their FFTs are compatible with trigonal prismatic $MoSe_2$ (Figure 2.11b), confirming the semiconducting phase.[203, 204] The absorption spectrum (Figure 2.11c) shows the A and B exciton at 784 nm and 699 nm, with a FWHM of 66 nm and 50 nm respectively. As for the MoS_2, the $MoSe_2$ excitonic peaks are thickness-sensitive; literature reports a progressive blue shift of the A exciton absorption features, going from 815 nm in a 6 layer sample to 795 nm for a monolayer.[46] Our $MoSe_2$ sample shows an A exciton position slightly blue shifted compared to what is reported in literature for monolayer samples, indicating a monolayer thickness.

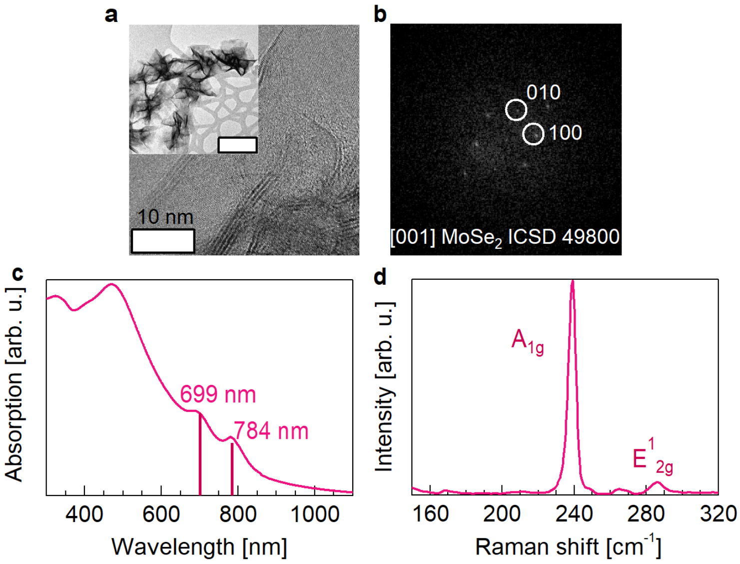

Figure 2.11: (a) HR-TEM image of the $MoSe_2$ sample, with the inset showing the nanoflower overall shape in a bright-field TEM image (scalebar: 100 nm). (b) FFT of the HR-TEM image, indexed as a [001]-oriented hexagonal $MoSe_2$ ($MoSe_2$-4H, ICSD 49800). (c) UV-Vis absorption spectrum of colloidal 2H-$MoSe_2$, indicating the A and B exciton positions at 784 nm and 699 nm, respectively. (d) Raman spectrum of $MoSe_2$, showing two Raman modes A_{1g} and $E_{2g}{}^1$.

Similar to MoS_2, Raman spectroscopy can also be used to determine the number of layers in a $MoSe_2$ sample. While for MoS_2 the modes spacing is the benchmark to determine the thickness, for $MoSe_2$, both the modes position and the amplitude ratio of the Raman modes is thickness-dependent, with the amplitude ratio $I(A_{1g})/I(E_{2g}{}^1)$ equal to 23.1 for a monolayer, reducing to 4.9 for a 10 layer sample, while the A_{1g} ($E_{2g}{}^1$) mode shifts from 243 cm^{-1} to 241 cm^{-1} (from 284 cm^{-1} to 287 cm^{-1}) going from bulk to a monolayer.[118,205] Here, the $E_{2g}{}^1$ and A_{1g} Raman modes (Figure 2.11d) are centered at 286 cm^{-1} and 239 cm^{-1}, respectively, with a amplitude ratio of 17.8 and an average mode spacing of 47.5±0.8 cm^{-1}. Both the modes amplitude ratio, and modes position suggests that we are close to a monolayer thickness.[46]

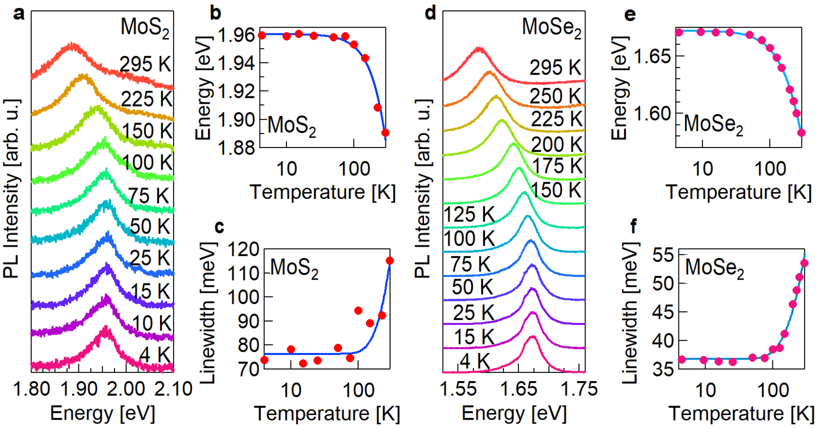

Figure 2.12: (a) Evolution of PL spectra of hBN encapsulated MoS$_2$ from 4 K to room temperature. (b) O'Donnell-Chen plot of hBN encapsulated MoS$_2$. (c) Evolution of emission linewidth with the temperature. (d) Evolution of PL spectra of hBN encapsulated MoSe$_2$ going from 4 K to room temperature. (e) O'Donnell-Chen plot of hBN encapsulated MoSe$_2$. (f) Evolution of emission linewidth with the temperature.

2.3.7 Cryo-photoluminescence of MoS$_2$ and MoSe$_2$

As last step of characterization, we investigated the fluorescence properties of both samples. These study has been done thanks to our collaboration with the Walter Schottky Institut at the Technische Universität München. Fluorescent TMDs are usually obtained via mechanically exfoliated bulk crystals[19] or CVD,[206] however literature reports examples of fluorescent TMDs obtained via colloidal synthesis or LPE methods. Samples obtained via LPE method are usually able to show fluorescence after extensive separation processes (to increase the monolayer fraction)[120] and different treatments such as annealing (used to restore the 2H phase)[132] or chemical treatments to suppress defects.[207] Literature reports about fluorescent colloidal TMDs includes pristine[208] and chemically treated colloidal WS$_2$ nanosheets,[209] as well as quantum dots (QDs).[25,166,210,211] Samples with the highest optical quality require encapsulating mechanically cleaved single-layer TMD flakes between few-nm thick hexagonal boron nitride (hBN) crystals, an insulator.[212] Encapsulation with hBN is a common procedure used to protect layered materials from electric and dielectric fluctuations of the local environment[213] and avoid sample degradation.[214,215] This leads to reduced exciton linewidth, lower electrostatic doping, and enhanced homogeneity.[212,213]

To compare the optical properties of our colloidal TMDs to their state-of-the-art solid-state counterparts, our colloidal samples were also encapsulated in hBN, and photoluminescence (PL) spectra were collected at various temperatures ranging between 4 K and 295 K. In Figure 2.12, we report the evolution of the PL spectra with temperature for both samples, as well as the associated shift in band gap and variation of the linewidth. Both samples show a progressive blue shift (*i.e.*, shift toward higher energy) and line width narrowing going from 295 K to 4 K. The 4 K emission energy is consistent for large monolayers, with values of 1.96 eV for MoS_2 and 1.68 eV for $MoSe_2$, reported for neutral excitons[212,213,216] The temperature dependence of the band gap is fitted with the O'Donnell-Chen[217] model:

$$E_g(T) = E_0 - S\langle\hbar\omega\rangle[coth\left(\frac{\langle\hbar\omega\rangle}{2kT}\right) - 1] \tag{2.5}$$

For MoS_2 ($MoSe_2$) we obtained an E_0 of 1.96 eV (1.67 eV), an electron-phonon coupling constant S of 2.37 (2.46) and an average phonon energy $\langle\hbar\omega\rangle$ of 25 meV (17 meV). These values are in good agreement with the literature.[218–221] The excitonic linewidth of MoX_2 includes the intrinsic line width Δ_0, and a contribution from acoustic Δ_{AC} and LO Δ_{LO} phonon coupling that increases with temperature, yielding the following temperature dependence:

$$\Delta(T) = \Delta_0 + \Delta_{AC}T + \Delta_{LO}\frac{1}{(\exp{(E_{LO}/k_BT)} - 1)} \tag{2.6}$$

The parameter E_{LO} is the LO phonon energy (here taken as the energy of the Raman mode ${E_{2g}}^1$); this is 47.7 meV and 29.6 meV for MoS_2 and $MoSe_2$, respectively. For both fits Δ_{AC} is fixed to zero. As a result, we found that for MoS_2 $\Delta_0 = 76\pm2$ meV, and $\Delta_{LO} = 210\pm24$ meV, while for $MoSe_2$ $\Delta_0 = 38.6\pm0.2$ meV, and $\Delta_{LO} = 39.7\pm0.9$ meV. Both samples display a QE in the order of 10^{-7}, several order of magnitude lower than mechanically exfoliated monolayer samples, reported as 10^{-3}.[18] Interestingly, our $MoSe_2$ monolayer exhibits a substantially narrower emission linewidth than the MoS_2 monolayer, suggesting that the latter might be more suitable for further application in opto-electronic or photonic devices.

2.4 Conclusions

In this chapter we explored the colloidal synthesis of MoS_2 and its optimization using the Design of Experiments approach. Using only 13 runs, we were able to screen the main factors involved in the synthesis and ultimately perform an optimization on the synthesis itself. Using UV-Vis and Raman spectroscopy we assess the semiconducting nature of the sample and we determine a significant monolayer yield in the sample. We then extended the synthesis on the selenide counterpart, obtaining $MoSe_2$ sample possessing significant monolayer yield. The two samples showed photoluminescence at cryogenic temperatures, with $MoSe_2$ clearly showing narrower emission features, thus providing a pathway toward further improvement based on the DOE approach. On longer term, this can lead to colloidal TMDs being a viable, scalable, and cost effective alternative to other TMD synthesis approaches.

3

Synthesis of Laterally Confined MoS_2

Author contributions

G. Pippia performed the synthesis, B. Martín-García performed the Raman and photoluminescence spectroscopy on the sample.

3.1 Prologue

In Chapter 2 we explored the application of Design Of Experiments method on the colloidal synthesis of MoS_2 and its adaptation on $MoSe_2$. In this chapter the colloidal synthesis of MoS_2 is further refined to reduce the lateral dimensions of the nanosheets, leading to an exciton blue shift, an improved exciton peak sharpness and background, and photoluminescence.

3.2 Introduction

As seen in Chapter 2, colloidal synthesis of MoS_2 (and in general of TMDs) usually yields to nanosheets with variable thickness and lateral sizes in the order of hundreds of nanometers.[23,157,173,222] While the thickness-dependent quantum confinement effect is well-known for TMDs, the raising of MoS_2-based 2D quantum dots started the interest on the effect of the lateral dimension on the band gap energy.[166,223,224] Similar to QDs, the reduction of (lateral) size in 2D-QDs yields to a blue shift of the PL energy due to a weak quantum confinement effect on the lateral dimensions (Figure 3.1a).[223,224]

Such blue shift increases while decreasing the lateral size of the

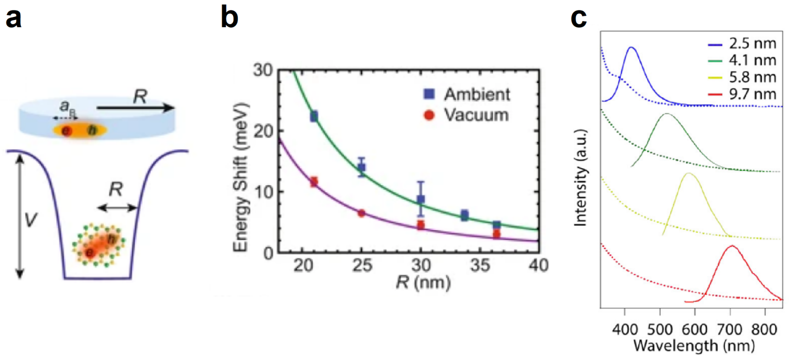

Figure 3.1: (a) Representation of a 2D confinement of excitons of Bohr radius in a potential well of radius R. (b) Size dependent exciton energy shift of MoS_2 2D-QDs measured in ambient (blue square) and vacuum (red circle) conditions. Adapted from Ref. 223. (c) UV-Vis absorption (dot) and PL spectra (solid) of the colloidal solutions of WSe_2 2D-QDs. Adapted from Ref. 166. Copyright 2016 American Chemical Society.

2D-QD, with small shifts in case of relatively large lateral sizes (Figure 3.1b) that become greater approaching the exciton Bohr radius (Figure 3.1c), opening new perspectives in the band gap tunability of TMDs. Here, we modify the synthesis protocol reported in Chapter 2 to reduce the lateral size of MoS_2 nanosheets and achieve a weak lateral quantum effect. The resulting nanosheets displays lateral size in the order of tens of nm, improved absorption excitonic features, a lower background scattering and narrow photoluminescence.

3.3 Experimental Results

Materials. Molybdenum pentachloride ($MoCl_5$, 99.99%, Sigma-Aldrich) and elemental sulfur ($\geq$ 99.95%, Sigma-Aldrich) were used without further purifications. 1-octadecene (ODE, Sigma-Aldrich) and oleylamine (OLA, 80-90% Acros Organics) were purified and stored in glovebox until further use.

Colloidal synthesis of lateral confined MoS_2 . The synthesis is performed under nitrogen using standard Schlenk line techniques. In a 25 mL three-neck flask a solution of OLA (15 mL) and elemental sulfur (0.13 mmol) is heat up to 300 °C. In the meantime, 0.065 mmol of $MoCl_5$ are sonicated in 3 mL of ODE until complete dissolution; the solution is then injected into the hot S-OLA solution at 10 mL h^{-1} using a syringe pump. After the injection, the reaction is cooled down using a water bath and subsequently purified three times using a mixture of toluene/isopropanol/acetone, hexane/isopropanol and chloroform/isopropanol respectively, followed by centrifugation at 5000 rpm to collect the sample. The nanosheets are then redispersed in chloroform and stored in a fridge until further use.

Characterization methods. Bright-field TEM images were acquired on a JEOL JEM-1011 microscope operating at an accelerating voltage of 100 kV. The samples were prepared by drop-casting of the suspension onto ultrathin C/holey C/Cu TEM grids. Micro-Raman data were acquired using a Renishaw inVia confocal Qontor instrument. The samples were measured on a Si/SiO_2 substrate with a 532 nm laser under a 50x magnification objective and 2400 l/mm diffraction grating. The laser power did not exceed 1 mW to avoid degradation of the samples. Low temperature was accomplished by liquid nitrogen cooling, maintaining the temperature and pressure at 80K and 10^{-6} bar. Ultraviolet-Visible (UV-Vis) absorption spectra of MoS_2 nanosheets dispersed in chloroform were recorded using a

PerkinElmer Lambda 950 spectrometer using a 1 cm path length quartz cuvette.

3.3.1 General Synthesis Protocol

Similar to the synthesis described in Chapter 2, the synthesis features the slow injection of a $MoCl_5$-ODE solution in a hot solution of elemental S and OLA. While most of the colloidal protocol reported in literature includes an high stoichiometric excess of sulfur,[23] in our synthesis we kept the exact molar ratio (2:1 S:Mo). The stoichiometric amount of sulfur is reported to influence the nanosheet size; in fact an increase of S concentration translates in larger nanosheets.[164] In this case, the synthesis is performed using the OVAT approach on the DOE-based protocol reported in Chapter 2.

3.3.2 Sample Characterization

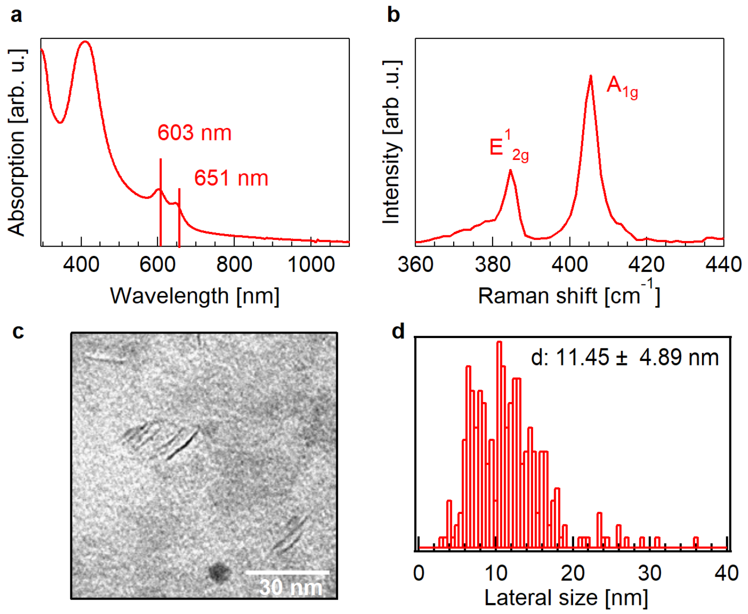

Figure 3.2: (a) UV-Vis absorption spectrum of the synthesized MoS_2 with highlighted the A and B exciton positions. (b) $E^{1}{}_{2g}$ and A_{1g} Raman modes of the aforementioned sample. (c) Lateral size distribution of MoS_2 nanosheets. d) TEM picture of the aforementioned sample (scalebar = 30 nm).

The MoS_2 sample is characterized by UV-Vis absorption spectroscopy (Figure 3.2a). Similar to what saw in Chapter 2, the spectrum displays two excitonic features associated to the 2H polytype, namely A and B exciton, centred at 651 nm and 603 nm respectively, with the A exciton position close to the band gap energy of monolayer MoS_2.[19] A quick comparison with the exciton position of the DOE optimized samples shows that in this case the exciton positions are blue shifted of ~3 nm and ~1 nm for A and B exciton respectively. The two excitons are characterized by a sharp spectral shape (FWHM of 37 nm and 26 nm for A and B exciton respectively), with values similar to the FWHM of the DOE optimized sample. A closer look on the background scattering (calculated as ratio between absorption value at 750 nm and of the A exciton) reveals that the value of background scattering is 0.21, almost 1/3 lower than the optimized MoS_2 sample. This reduction in background translated to visually sharper peaks in the UV-Vis spectrum; furthermore the background scattering is correlated to lateral size dimension, suggesting a reduction of the latter.

The Raman spectrum (Figure 3.2b) displays the two modes, *i.e.*, $E^1{}_{2g}$ and A_{1g} modes centred at 384.7 cm^{-1} and 405.2 cm^{-1} respectively, with a mode spacing of 20.5 cm^{-1} indicating a mixture of mono- and bilayer nanosheets.[225] This is similar to the spacing reported for the DOE optimized sample (20.8 cm^{-1}).

Using TEM we sized the standing edges of the nanosheets (Figure 3.2c), finding an average size of 11.45 nm ± 4.89 nm. MoS_2 nanosheets obtained via exfoliation presents lateral sizes in the order of hundreds of nm;[122] small size colloidal MoS_2 quantum dots (QDs) and nanosheets are present in literature, with values around 10-30 nm.[164, 226, 227] To further confirm the influence of the lateral size on the A exciton position we synthesize and size different samples obtained with the same S:Mo ratio (Figure 3.3, samples from A to E), adding two samples from previous experimental work (samples F and G). Samples A-C, and E are obtained with the protocol reported in the Experimental Section; D is the sample studied in this work, F is the MoS_2 sample discussed in Chapter 2 while sample G uses a similar protocol as samples A-E, with 1 mL of ODE and a S:Mo ratio of 3. The resulting data shows a clear red shift of the A exciton with the lateral size. This possible weak confinement on the lateral size have been already explored for MoS_2 QDs, showing an increase in photoluminescence energy decreasing the QD size.[223, 224]

Finally, we collect the photoluminescence spectrum of the laterally

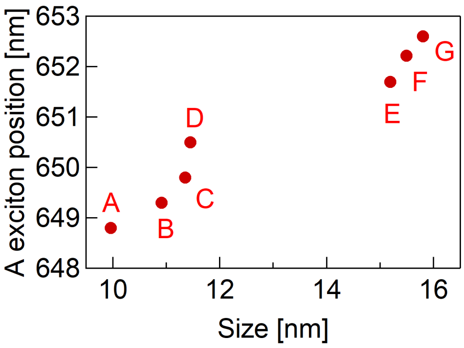

Figure 3.3: Correlation between lateral size dimension of MoS_2 nanosheets and the relative A exciton position.

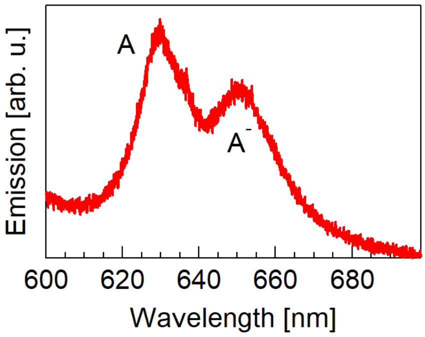

Figure 3.4: Photoluminescence spectrum of lateral confined MoS_2 collected at 80K.

confined MoS_2 at 80K (Figure 3.4). We collect the spectrum at low temperature in order to suppress nonradiative recombination and be reasonably sure to observe photoluminescence. The spectrum is characterized by the presence of two different peaks, a (neutral) exciton (labelled A) and a trion (an exciton featuring an additional electron or hole labelled A^-). We assigned the latter to a negative trion and not to the B transition due to the not sufficient difference in energy between the two photoemissions. Notably, in our sample trion and neutral exciton emissions are well separated, while similar samples shows a single peak generated by the overlapping of the two emissions.[228] The A and A^- are centred at 629 nm (1.97 eV) and 649 nm (1.91 eV) respectively. The difference between trion and neutral exciton energy is the trion binding energy,[229, 230] estimated to be ~60 meV (the 10% of the A exciton binding energy[231]); however literature reports values of 18-30 meV.[43, 224, 230] The FWHM of neutral exciton and trion are 42 meV and 66 meV respectively, similar to what reported in literature.[223, 232] The FWHM here reported is lower than the one of hBN encapsuled MoS_2 sample (∼75 meV) discussed in Chapter 2, suggesting a lower defect density.

3.4 Conclusions

In this chapter we explored the colloidal synthesis of laterally confined MoS_2, starting from the colloidal protocol discussed in chapter 2. Reducing the S:Mo stoichiometric ratio to 2, we obtained semiconducting MoS_2 sample showing blue shifted and sharp excitonic features, a lower background scattering, and sample composition of mono- and bilayers, as determined by UV-Vis and Raman spectroscopy. Morever, via TEM imaging, we determined a lateral size between 10 and 20 nm. Further characterization via PL spectroscopy revealed photoluminescence at 80K, composed by neatly separated neutral and trion excitons, and an energy closed to the MoS_2 monolayer band gap energy. This further development reinforces the idea of colloidal synthesis as viable, scalable, and cost effective route on the production of TMDs nanocrystals.

4

Colloidal Synthesis of Tungsten Disulfide and Diselenide Nanosheets

Author contributions on WS_2

The findings on the WS_2 synthesis optimization have been published in: **A colloidal route to semiconducting tungsten disulfide nanosheets with monolayer thickness**; **Gabriele Pippia**, Diem Van Hamme, Beatriz Martín-García, Mirko Prato, Iwan Moreels. D. Van Hamme performed the synthesis and the initial data analysis, B. Martín-García performed the Raman spectroscopy, M. Prato performed the XPS measurements on the samples. G. Pippia completed the data analysis and with I. Moreels wrote the manuscript.

Acknoledgments

I want to thank Katrien Haustraete for providing the HR-TEM images of the WS_2 sample.

Author contributions on WSe_2

G. Pippia performed the synthesis, B. Martín-García performed the Raman spectroscopy while M. Prato performed the XPS measurement on the sample.

4.1 Prologue

*While in the previous chapters we explored the colloidal synthesis of MoS_2 and $MoSe_2$, here we explore the colloidal synthesis of WSe_2. Starting from the work of the master student Diem Van Hamme on the colloidal synthesis of WS_2 nanosheets, we develop a synthesis protocol for the colloidal synthesis of WSe_2 with monolayer thickness. In the first part are shortly reported the findings on the DOE optimization of WS_2 synthesis, while in the second part will be discussed the synthesis of WSe_2 nanosheets. For a more complete discussion about the results of the DOE optimization of WS_2 synthesis, please refer to the article "A colloidal route to semiconducting tungsten disulfide nanosheets with monolayer thickness", **Nanoscale**, 2022, **14**, 15859-15868.*[233]

4.2 Introduction

Tungsten-based TMDs possess have arise the interests of research community due similar properties compared to Mo-based TMDs. The larger (and heavier) metal atom gives to WX_2 (X = S, Se, Te) peculiar properties, such as smaller effective electron and hole masses[234] (making WS_2 the first TMD achieving population inversion)[235] and stronger spin-orbit coupling compared to the Mo counterpart (426 meV for WS_2 and 148 meV for MoS_2 respectively), making it and a potential candidate as laser gain material[236] and for spin field-effect transistors.[36] The large metal radius influences longitudinal acoustic phonon limited electron mobility; calculation have shown that WS_2 possess high electron mobility compared to MoS_2 (1100 cm^2 V^{-1} s^{-1} and 340 cm^2 V^{-1} s^{-1} respectively),[237] essential for applications involving logic devices (such as transistors). The colloidal synthesis of tungsten-based TMDs have been characterized by the difficulty of obtaining the semiconducting polytype. Only in 2014 the colloidal synthesis of WS_2 reached a breakthrough when Mahler *et al.* reported the synthesis of semiconductor WS_2 via colloidal route.[222] This have been possible via activation of the tungsten precursor using oleic acid (OA) and hexamethyldisilazane (HMDS), (similarly to what seen in the synthesis of GeS and GeSe)[238] which coordinate the tungsten precursor, ultimately lowering the activation energy for the semiconductor polytype formation.[222] This protocol ultimately yielded in 2021 the publication of an article of the micro-photoluminescence of colloidal WS_2 nanosheets.[208] At the same time, WSe_2 have been subject of different investigations due to the similarities with WS_2 properties.[239–241] WSe_2 can be found as 1T (metallic) or 2H (semiconducting) polytype; the semiconductor displays an indirect band gap of 1.20 eV as bulk and a direct band gap of 1.65 eV as monolayer,[118] a phonon-limited carrier mobility of 705 $cm^2\ V^{-1}\ s^{-1}$,[237] and a spin-orbit coupling of 0.46 eV; making it suitable for different applications such as photodetectors,[242] field-effect transistors,[243] and spintronics.[244]

4.3 Experimental Results

Materials. Elemental selenium ($\geq$ 99.99%, Strem Chemicals), elemental sulfur ($\geq$99.95%, Sigma-Aldrich), tungsten hexachloride (WCl_6, $\geq$ 99.9%, Sigma-Aldrich), hexamethyldisilazane (HMDS, $\geq$ 99.9%, Sigma-Aldrich) were used without further purifications. Oleylamine (OLA, 80%-90%, Acros Organics), 1-octadecene (ODE, 90%, Alfa Aesar), oleic acid (OA, 90%, Sigma-Aldrich), were purified and stored in glovebox until used.

General DOE 2H-WS_2 synthesis. The synthesis is performed under nitrogen using standard Schlenk line techniques. All amounts and temperatures are reported in Table 4.1. In the typical synthesis, 0.028 mmol WCl_6 is dispersed in 1 mL anhydrous ODE and OA while, in a second vial, elemental sulfur in 15 mL of anhydrous OLA is mixed together; both solutions are then sonicated for 20 min until complete dissolution. The sulfur precursor is transferred into a 25 mL three neck flask and heated up to the selected temperature. Subsequently, 0.2 mL of HMDS is added to the tungsten precursor solution; the final solution is then injected into the hot S-OLA solution at a selected injection speed using a syringe pump. The reaction mixture is held at the selected temperature during the injection, and after that, it is rapidly cooled down to room temperature. The product is purified three times using a mixture of toluene/isopropanol/acetone, hexane/isopropanol and chloroform/isopropanol, respectively, followed by centrifugation at 5000 rpm to collect the sample. The nanosheets are finally dispersed in chloroform and stored in a fridge until further use.

Monolayer-optimized 2H-WS_2 nanosheet synthesis. The synthesis is performed under nitrogen using standard Schlenk line techniques. In the typical synthesis, 0.028 mmol WCl_6 is dispersed in 1 mL anhydrous ODE and 0.160 mL of OA while, in a second vial, 0.106 mmol of elemental sulfur in 15 mL of anhydrous OLA is mixed together; both solutions are then sonicated for 20 min until complete dissolution. The sulfur precursor is transferred into a 25 mL three neck flask and heated up to 320 °C. Subsequently, 0.2 mL of HMDS is added to the tungsten precursor solution; the final solution is then injected into the hot S-OLA solution at 8 mL h^{-1} using a syringe pump. The reaction mixture is held at the selected temperature during the injection and after that, it is rapidly cooled down to room temperature. The product is purified three times using a mixture of toluene/isopropanol/acetone, hexane/isopropanol and chloroform/isopropanol, respectively, followed by centrifugation at 5000 rpm to collect the sample. The nanosheets are finally dispersed in chloroform and stored in the fridge until further use.

Background-optimized 2H-WS_2 nanosheet synthesis. The synthesis is performed under nitrogen using standard Schlenk line techniques. In the typical synthesis, 0.028 mmol WCl_6 is dispersed in 1 mL anhydrous ODE and 0.240 mL of OA while, in a second vial, 0.106 mmol of elemental sulfur in 15 mL of anhydrous OLA is mixed together; both solutions are then sonicated for 20 min until complete dissolution. The sulfur precursor is transferred into a 25 mL three neck flask and heated up to 310 °C. Subsequently, 0.2 mL of HMDS is added to the tungsten precursor solution; the final solution is then injected into the hot S-OLA solution at 2 mL h^{-1} using a syringe pump. The reaction mixture is held at the selected temperature during the injection and after that, it is rapidly cooled down to room temperature. The product is purified three times using a mixture of toluene/isopropanol/acetone, hexane/isopropanol and chloroform/isopropanol, respectively, followed by centrifugation at 5000 rpm to collect the sample. The nanosheets are finally dispersed in chloroform and stored in the fridge until further use.

Optimized 2H-WSe_2 Nanosheets Synthesis. The synthesis is performed under nitrogen using standard Schlenk line techniques. 0.02 mmol WCl_6 dispersed in 3 mL anhydrous ODE and 0.24 mL of OA while, in a second vial, elemental selenium (0.044 mmol) in 15 mL of anhydrous OLA are mixed together; both solution are then sonicated for 40 min until complete dissolution. The selenium precursor is transferred into a 25 mL three neck flask and heated up at 315 °C. Subsequently, 0.2 mL of HMDS is added to the tungsten precursor solution; this final solution is then injected into the hot Se-OLA solution at a 7.5 mL h^{-1} using a syringe pump. The reaction mixture is held at the selected temperature during all the injection; after it is rapidly cooled to room temperature. The product is purified as described above. The nanosheets are finally dispersed in chloroform and stored in the fridge until further use.

Characterization methods. Bright-field TEM images were acquired on a JEOL JEM-1011 microscope operating at an accelerating voltage of 100 kV. The samples were prepared by drop-casting of the suspension onto ultrathin C/holey C/Cu TEM grids. High-resolution TEM images were acquired on a JEOL JEM-2200FS operating at an acceleration voltage of 200 kV. The samples were prepared by drop-casting of the suspension onto ultrathin C/holey C/Cu TEM grids.

Micro-Raman data were acquired using a Renishaw inVia confocal Qontor instrument. The samples were measured on a SiO_2/Si substrate with a 532 nm laser under a 50x magnification objective and 2400 l/mm diffraction grating. The laser power did not exceed 1 mW to avoid degradation of the samples. Ultraviolet-Visible (UV-Vis) absorption spectra of WX_2 nanosheets dispersed in chloroform were recorded using a PerkinElmer Lambda 950 spectrometer using a 1 cm path length quartz cuvette. X-ray photoelectron spectroscopy (XPS) measurements were recorded on a Kratos Axis UltraDLD spectrometer using a monochromatic Al-K_α source operated at 20 mA and 15 kV. High resolution spectra are acquired at pass energy of 10 eV, energy step of 0.1 eV and take-off angle of 0 degrees with respect to sample normal direction. The analysis area is 300 x 700 micron. The samples are prepared by dropcasting the solutions onto a freshly cleaved highly oriented pyrolytic graphite (HOPG) and the energy scale is calibrated on W $4f_{7/2}$ peak of WO_3, set at 35.8 eV. The fitting was done with the CasaXPS software.[245]

4.3.1 Colloidal Synthesis Protocol

The colloidal synthesis protocol is similar to the one reported by Frauendorf *et al.*[208] The synthesis features the slow injection of a solution containing tungsten hexachloride (WCl_6), OA and HMDS in a hot solution of OLA and elemental Se. Both OA and HMDS, according to Mahler *et al.* are necessary in order to obtain the semiconducting polytype.[222] The OA and HMDS used are based on the work of the master student Diem Van Hamme on the optimization of the colloidal synthesis of WS_2. In the following sections are briefly reported the findings of the DSD optimization and the results of this work.

4.3.2 DSD modelling on WS_2 colloidal synthesis

The results reported in this section have been obtained, under my supervision, by the master student Diem Van Hamme during her master thesis project and have been used as starting point for the synthesis of WSe_2 nanosheets. The colloidal protocol of WS_2 is similar to what reported for the WSe_2 synthesis, with the use of elemental sulfur instead of selenium. For a more complete discussion about the results of this work, please refer to the original work.[233]

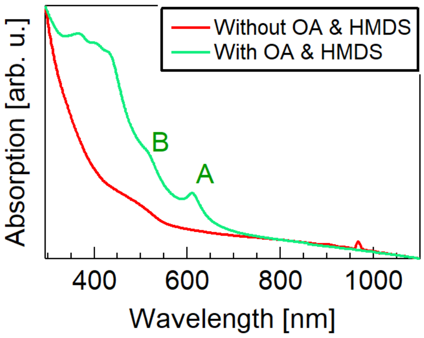

Figure 4.1: Absorption spectra of synthesized WS_2 with (green) and without (red) OA and HMDS. The labels A and B indicates the exciton peaks arising from the K point of the Brillouin zone.

4.3.2.1 Definitive Screening Design

For the application of the DSD design (see section 2.2.1 for details on the design) on the WS_2 synthesis we selected the following factors: reaction temperature, precursor injection rate, S/W and OA/W molar ratio. The reaction time is not taken into account explicitly but embedded in the injection rate parameter, (*i.e.*, reaction is stopped at the end of the precursor injection). The first three factors are chosen as they may impact the WS_2 nanosheet growth and the final crystal phase.[164,246] The OA/W ratio, is necessary to achieve the desired polytype.[222] Tungsten concentration, ODE and OLA volume and HMDS/W ratio are kept fixed. The total number of runs used in this DSD analysis are 13, the minimum amount required to avoid performance degradation. The full list of experimental runs is reported in Table 4.1

Table 4.1: Input factor X_i (i = [1, 4]) and responses Y_i retrieved from the DOE experiments. used in the DSD. X_1 = Reaction temperature, X_2 = Injection rate, X_3 = S/W molecular ratio, and X_4 = OA/W molecular ratio. Y_1 = A exciton position, Y_2 = A exciton linewidth, and Y_3 = Background Absorption.

Run No.	X_1 [°C]	X_2 [mL·h^{-1}]	X_3	X_4	Y_1 [nm]	Y_2	Y_3
1	320	8	4	30	610.5	0.95	0.45
2	320	2	6	30	615.4	1.01	0.35
3	320	8	8	10	608.9	0.93	0.55
4	315	8	8	30	608.8	0.92	0.52
5	310	2	4	30	609.0	0.97	0.40
6	310	8	4	20	611.3	0.96	0.50
7	315	5	6	20	611.2	0.95	0.43
8	315	2	4	10	615.4	0.98	0.40
9	310	8	6	10	610.8	0.92	0.64
10	320	5	4	10	612.9	1.00	0.39
11	320	2	8	20	615.9	1.01	0.36
12	310	5	8	30	611.9	0.98	0.46
13	310	2	8	10	609.3	0.94	0.56

A typical 2H-WS$_2$ absorption spectrum is characterized by the presence of the A and B exciton features (Figure 4.1) that arises from the transition from the K point in the Brillouin zone from the valence to the conduction band. For this design we select the same metrics used for the MoS$_2$ optimization discussed in Chapter 2, *i.e.*, the A exciton peak wavelength λA is obtained via second-derivative analysis while its linewidth is evaluated indirectly by calculating the ratio between the maximum peak absorbance and the absorbance of the local minimum at the high energy side of the exciton. The background absorption/scattering is quantified by dividing the absorbance at 790 nm by the absorbance at A exciton position. In Table 4.1 we report the factors of all the DOE runs and the relative responses. In order to avoid model overfitting, we decided to minimize the Bayesian Information Criterion (BIC),[247] keeping at the same time a low corrected Akaike Information Criterion (AICc).[248]

4.3.2.2 A exciton position modelling

For the DSD analysis of the A exciton position λA we excluded the results of run no. 12 as it was listed as an outlier. We identified four different input factors as statistically relevant: the reaction temperature (X_1), injection rate (X_2), as well as their combination $X_1 \cdot X_2$, and the product $X_2 \cdot X_4$ of injection rate and OA/W ratio (X_4). The p-values associated to the single factors are reported in Table 4.2.

Table 4.2: Associated *p*-values of the main factors interaction as well as two-factor interactions for A exciton positions.

Factors		p-value
$X_1 \cdot X_2$	Reaction temperature · Injection rate	0.0001
X_2	Injection rate	0.0001
X_1	Reaction temperature	0.00019
$X_2 \cdot X_4$	Injection rate · OA/W ratio	0.00025
X_4	OA/W ratio	0.16234

As the two-factor product $X_2 \cdot X_4$ is statistically relevant, DSD includes also X_4 in the prediction expression, which reads as follows:

$$\begin{aligned}\lambda_A = 611.33 + 0.871 \cdot (\frac{(X_1 - 315)}{5}) - 1.2 \cdot (\frac{(X_2 - 5)}{3})\\ -0.171 \cdot (\frac{(X_4 - 20)}{10}) - 1.6 \cdot (\frac{(X_1 - 315)}{5}) \cdot (\frac{(X_2 - 5)}{3})\\ +0.9 \cdot (\frac{(X_2 - 5)}{3}) \cdot (\frac{(X_4 - 20)}{10})\end{aligned} \tag{4.1}$$

This expression yields the spectral position of the A exciton as a function of the input parameters X_i, expressed as the difference between the parameter value and the mean value of the range used in the DSD (see Table 2.1), normalized to half the width of the respective range (as 3 values are taken per range, see Table 2.1). As such, the prefactor (e.g. 0.871 for factor X_1), immediately shows the impact of each factor, with larger values indicating a stronger effect. Hence, equation (4.1) can give insight into the influence of the different factors on the spectral position of the A exciton. This is visualized using a contour plot that include the effect on the A exciton position of the factors found statistically relevant (Figure 4.2). For instance, decreasing the reaction temperature (X_1, panel a) leads to a blue shift (*i.e.*, shift towards shorter wavelength) of the A exciton absorption peak, independent of the injection rate (panel a) and at medium to high concentration of OA (panel b) compared to W. However, another region of blue shifted exciton absorption is found combining high reaction temperature and high injection rate (panel a); the same type of region can be found having high injection rate and low OA concentration compared to W. Both may be due to an increased nucleation rate induced by the larger precursor concentrations and higher temperature, limiting further growth into multilayers. As X_4 is associated with a small prefactor of 0.171, and was deemed not statistically relevant, we omit it from a further discussion. Surprisingly, S/W ratio seems to not have any statistically relevant effect on the A exciton position.

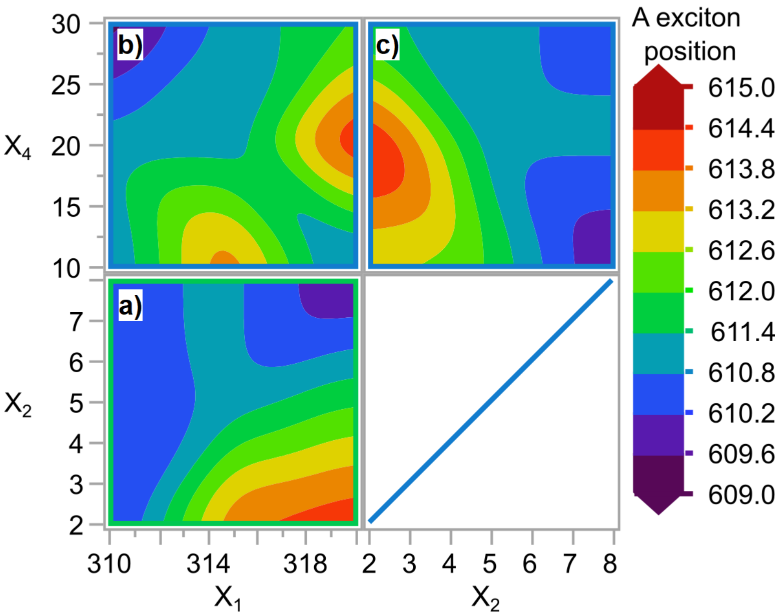

Figure 4.2: Contour plot of peak sharpness variation with reaction temperature, injection rate, and S/W ratio.

4.3.2.3 A exciton sharpness modelling

The same procedure is then applied for the exciton sharpness and absorption background models, discarding run no. 12 as it is identified as an outlier. The exciton sharpness model counts six factors, consisting in three main factors (injection rate, reaction temperature and S/W ratio), one two-factors interaction (reaction temperature · injection rate), and two quadratic interactions (reaction temperature · reaction temperature and S/W ratio · S/W ratio). The prediction expression is reported in Equation 4.2, while the associated *p*-values are reported in Table 4.3.

Table 4.3: Factors interactions and relative *p*-values for A exciton sharpness model.

	Factors	*p*-values
X_2	Injection rate	0.00010
X_1	Reaction temperature	0.00083
$X_1 \cdot X_2$	Reaction temperature · Injection rate	0.00172
X_3	S/W ratio	0.00210
$X_1 \cdot X_3 \cdot X_1$	Reaction T · Reaction T	0.03209
$X_3 \cdot X_3$	S/W · S/W	0.03560

$$
\begin{aligned}
S = 0.940 + 0.0157 \cdot (\frac{(X_1 - 315)}{5}) - 0.0228 \cdot (\frac{(X_2 - 5)}{3}) \\
-0.0128 \cdot (\frac{(X_3 - 6)}{2}) + 0.0128 \cdot (\frac{(X_1 - 315)}{5}) \cdot (\frac{(X_1 - 315)}{5}) \\
-0.0158 \cdot (\frac{(X_1 - 315)}{5}) \cdot (\frac{(X_2 - 5)}{3}) \\
+0.0141 \cdot (\frac{(X_3 - 6)}{2}) \cdot (\frac{(X_3 - 6)}{2})
\end{aligned}
\tag{4.2}
$$

The contour plot of the peak sharpness is shown in Figure 4.3. Sharper peaks are obtained at low injection rate (X_2) and high temperature (X_1) (panel a), almost independently of S concentration compared to W (X_3, panel b). A region of high sharpness is found to be, at low injection rates, almost independent of the S/W ratio (panel c). This

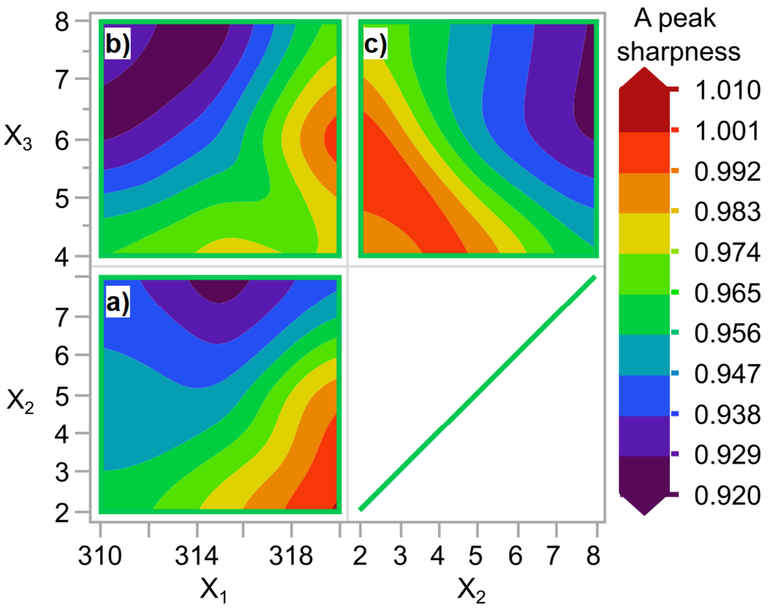

Figure 4.3: Contour plot of peak sharpness variation with reaction temperature, injection rate, and S/W ratio.

may be explained by the longer reaction time associated to a lower injection rate, as well as the energy provided by the high temperature to overcome the barrier energy between the 1T and 2H phase.

4.3.3 Background scattering modelling

As last, we analyzed the background absorption. The model counts a total of 7 factors, featuring 4 main factor interaction (injection rate, reaction temperature, OA/W, S/W), 2 two-factor interaction (reaction temperature · OA/W and OA/W · S/W), and 1 quadratic interaction (OA/W · OA/W). The prediction expression is reported in Equation 4.3, while the associated p-values are reported in Table 4.4.

Table 4.4: Factors interactions and relative p-value for background scattering model.

	Factors	p-values
X_2	Injection rate	0.00002
X_1	Reaction temperature	0.00006
X_4	OA/W ratio	0.00015
X_3	S/W ratio	0.00027
$X_4 \cdot X_4$	OA/W · OA/W	0.00367
$X_1 \cdot X_4$	Reaction T · OA/W	0.00473
$X_4 \cdot X_3$	OA/W · S/W	0.01122

$$\begin{aligned} B = 0.432 - 0.0445 \cdot (\frac{(X_1 - 315)}{5}) - 0.0364 \cdot (\frac{(X_4 - 20)}{10}) \\ +0.0595 \cdot (\frac{(X_2 - 5)}{3}) + 0.0317 \cdot (\frac{(X_3 - 6)}{2}) \\ +0.0212 \cdot (\frac{(X_1 - 315)}{5}) \cdot (\frac{(X_4 - 20)}{10}) \\ +0.0406 \cdot (\frac{(X_4 - 20)}{10}) \cdot (\frac{(X_4 - 20)}{10}) \\ -0.0172 \cdot (\frac{(X_4 - 20)}{10}) \cdot (\frac{(X_3 - 6)}{2}) \end{aligned} \tag{4.3}$$

The background scattering showed in Figure 4.4 features, in this case all the factors involved in the synthesis, as they are listed as statistically relevant. Low background scattering regions are characterized by high reaction temperature and low injection rate (panel

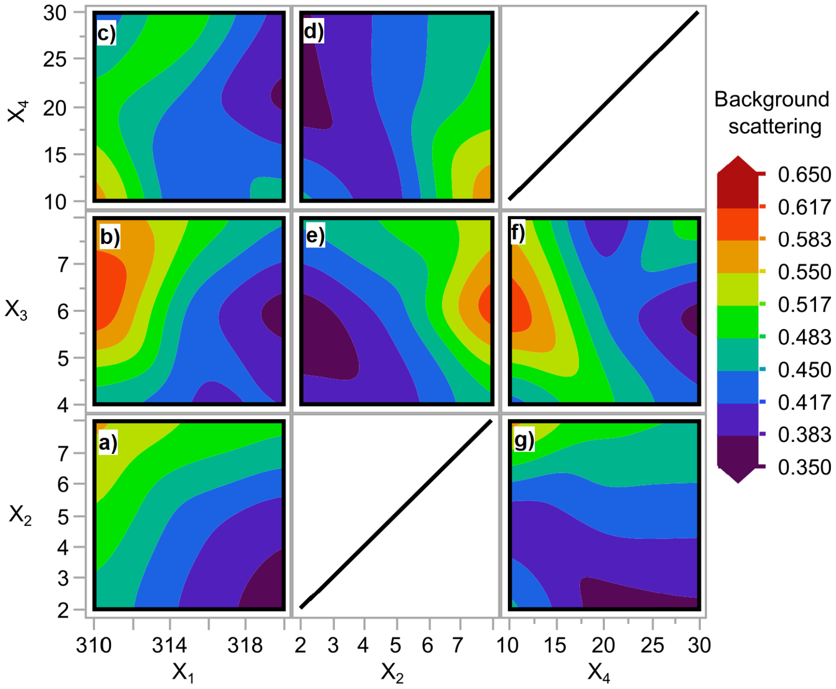

Figure 4.4: Contour plot of background scattering variation with reaction temperature, injection rate, S/W ratio, and OA/W ratio.

a), independently of S/W and OA/W ratios (panel b and c respectively).

4.3.3.1 Testing the prediction models

Confronting all the contour plots for the different responses, it is clear that finding common reaction conditions for all three responses is not trivial. Furthermore, single responses can have more than one optimal region, making complicated the selection of single values. For this reason we decide to combined the prediction models for the three different responses to obtain experimental conditions that leads, in order of importance, to the lowest A exciton position, a sharp exciton feature, and a reduced background absorption. This order of importance has been chosen considering, as explicated before, the meaning of these metrics. The prediction model suggested the following reaction conditions: reaction temperature of 320 °C, injection rate of 8 mL h^{-1}, S/W ratio of 4, and OA/W ratio of 20. The synthesis is carried out and the experimental responses are compared to the model prediction (Table 4.5).

Table 4.5: Comparison between predicted and experimental responses of A exciton position optimized sample.

	A exciton position [nm]	A exciton peak sharpness	Background absorption parameter
Predicted results	609.4	0.957	0.415
Experimental results	609.7	0.949	0.512

The experimental values are in good agreement with the prediction model, with A exciton position and sharpness near to a perfect match; the largest discrepancy concerns the background absorption parameter.

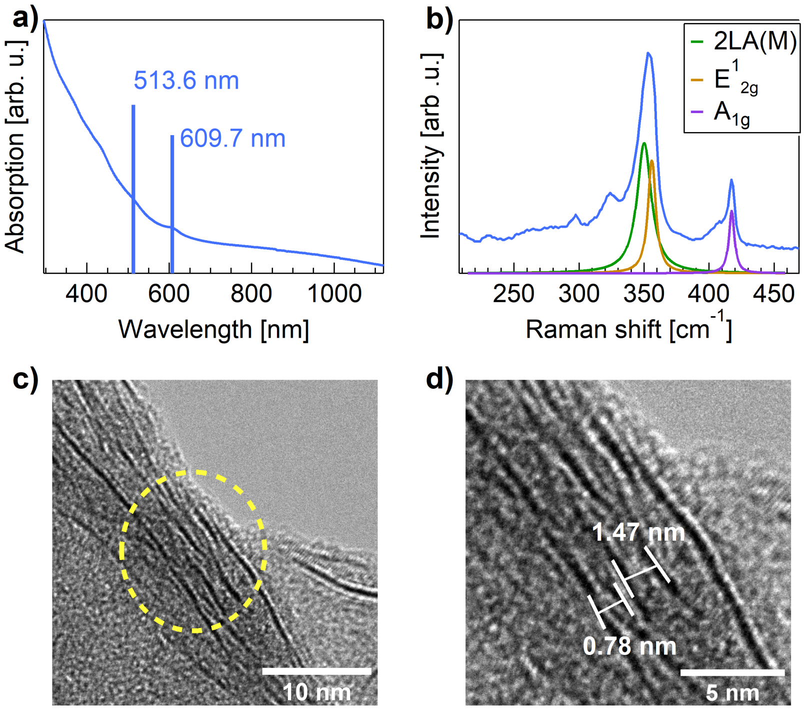

Figure 4.5: a). UV-Vis absorption spectrum of A exciton positon optimized sample with highlighted the A and B exciton positions. b). Raman spectrum (excitation source: 532 nm) of the aforementioned sample with the 2LA(M), E$^1{}_{2g}$, and A$_{1g}$ modes components. c). HR-TEM image of the aforementioned sample with highlighted the edges of the nanosheeets. d) Magnification of panel c with highlighted the distance between the single sheets.

The A exciton absorption peak is center at 609.7 nm with a calculated sharpness of 0.949 and a background absorption parameter of 0.512. Our sample shows an A and B exciton positions centered at 609.7 nm and 513.6 nm respectively (Figure 4.5a); the A exciton value is similar to what already reported for colloidal monolayer WS$_2$[208, 222, 249] while our sample shows a blue shifted B exciton compared to analogue samples. The splitting energy between the two exciton (as a consequence of the strong spin-orbit coupling in W atoms[37]) is 96.1 nm (~387 meV), in line to what observed in CVD[250] as well as colloidal WS$_2$ nanosheets.[208]

Trying to determining the best combination of factors, we found a second suitable optimization synthesis that can yield to blue shifted

A exciton, sharp peak and lower background absorption. As stated before, this is not unusual, since the contour plots shows the existence of more of one possible region with optimal responses. In this optimization, however, we focused on the reduction of the background absorption scattering. This is correlated to the nanosheet size as well as the metallic (1T) WS_2 spectral contribution to the overall absorption spectrum. We followed these experimental conditions: reaction temperature of 310 °C, injection rate of 2 mL h^{-1}, S/W ratio of 4, and OA/W ratio of 30. The synthesis is carried out as the precedent and the comparison between predicted and experimental responses are reported in Table 4.6.

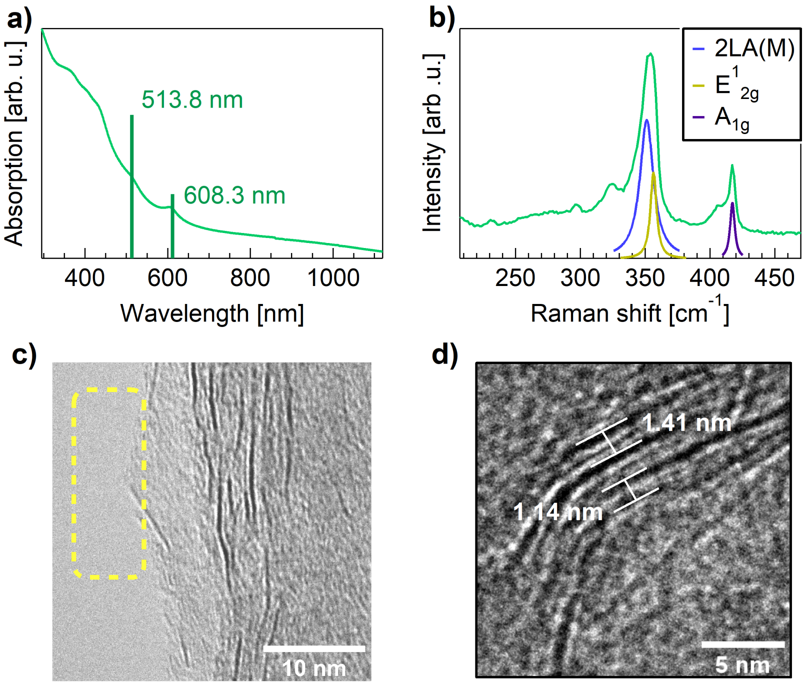

Figure 4.6: a). UV-Vis absorption spectrum of background optimized sample with highlighted the A and B exciton positions. b). Raman spectrum (excitation source: 532 nm) of the aforementioned sample with the 2LA(M), $E^1{}_{2g}$, and A_{1g} modes components. c). HR-TEM image of the aforementioned sample with highlighted the edges of the nanosheeets. d) Magnification of panel c with highlighted the distance between the single sheets.

Table 4.6: Comparison between predicted and experimental responses of background optimized sample.

	A exciton position [nm]	A exciton peak sharpness	Background absorption parameter
Predicted results	609.0	0.971	0.385
Experimental results	608.3	1.003	0.385

As the exciton-optimized WS_2, the background-optimized shows in the UV-Vis absorption spectrum the presence of the A and B exciton peaks, centered at 608.3 nm and 513.8 nm respectively (Figure 4.6a). Furthermore, their position is slightly blueshifted compared to the previous sample; however this can be attributed to the reduced background contribution on the overall spectrum.

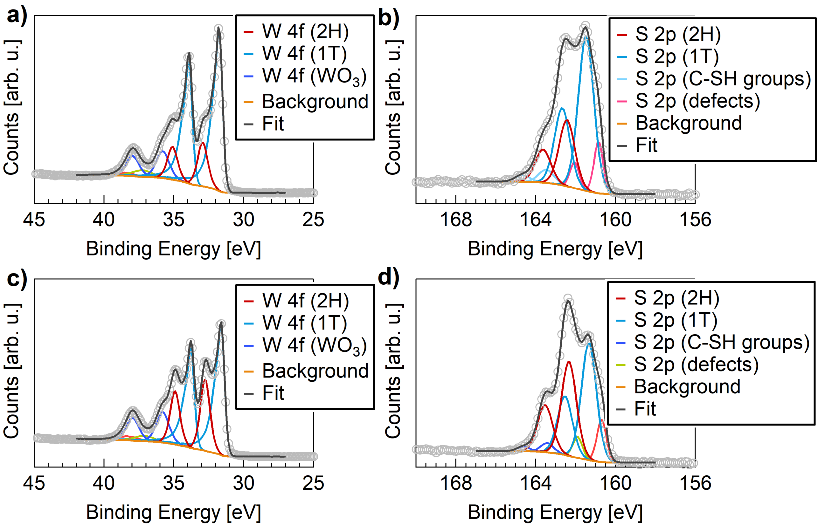

Figure 4.7: XPS spectra of W 4f and W 5p (a) and S 2p (b) core levels of A exciton-optimized WS_2 nanosheets. XPS spectra of W 4f and W 5p (c) and S 2p (d) core levels of background-optimized WS_2 nanosheets.

In order to elucidate this difference in background contribution, we performed XPS on the samples over the energy regions typical of W 4f and S 2p peaks (Figure 4.7a–c). In both, we observed the presence of W signals (Figure 4.7a–c) attributable to both the 2H (32.9 eV and 35.1 eV)[222,251] and 1T (31.8 eV and 33.9 eV)[222,251] polytypes as well as the signals associated with WO_3 (centered at 35.8 eV and

38.0 eV)[222] traceable back to a condensation reaction between OA and OLA.[252] In Figure 4.7b and d we report the S 2p signals of WS_2, finding signals associated with 2H (162.5 eV and 163.7 eV) and 1T polytypes (161.5 eV and 162.7 eV) and S 2p signals associated with thiol species.[253,254] A low binding energy S 2p doublet is also present (components at 160.8 eV and 162.0 eV) in both samples; its position matches the one of the other metal sulfides. However, since we did not observe any trace of contamination in the investigated samples, we tentatively assign this doublet to under-coordinated S, in analogy to what has been reported for defective graphene in the literature.[255] Interestingly, while we observed the same types of signals for both samples in the W and S regions, we can conclude that the second optimized sample, synthesized at lower temperature, yields a noticeable decreased contribution of the 1T polytype, as the relative intensities of the associated W 4f and S 2p peaks are lower. Hence, even if we were not able to fully suppress the formation of the 1T polytype, it is clear that, while a monolayer of WS_2 can be formed under both optimized conditions (at both high and low temperature), only the synthesis at a lower temperature yields a sample with reduced formation of the 1T polytype. This is also translated into a lower contribution of the metallic phase to the overall absorption spectrum, yielding reduced background scattering and sharper excitonic features compared to the exciton optimized sample. The two polytypes are separated by an energy barrier of 490 meV,[256] confirming that a higher temperature favors an increase of the metallic polytype in the ensemble, and syntheses that aim to obtain WS_2 in monolayer form and in the 2H semiconducting polytype should be performed at lower temperature. Such a decrease in metallic polytype may be justified by the different reaction times for the two samples. In fact, the reaction time of the background optimized sample is four times longer than the A exciton optimized sample, yielding a greater metallic-to-semiconducting conversion compared to the A exciton optimized sample.

4.3.4 WSe_2 Synthesis

Starting from the findings discussed in the previous section, we then translate the synthesis of WS_2 into its selenide counterpart, changing the chalcogen source and adapting the reaction parameters.

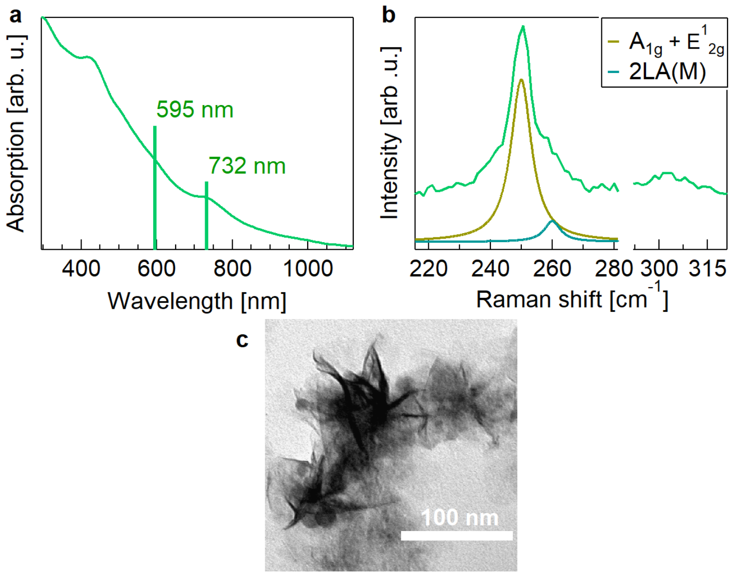

Figure 4.8: (a) UV-Vis absorption spectrum of WSe_2 sample with highlighted the A and B exciton positions. (b). Raman spectrum (excitation source: 532 nm) of the aforementioned sample with the 2LA(M), $E^1{}_{2g}$, and A_{1g} modes components and the $B^1{}_{2g}$ mode region. (c). Bright-field TEM image of the aforementioned sample.

As expected by a semiconductor TMDs, the UV-Vis absorption spectrum displays the presence of the excitons A and B, centered at 732 nm and 595 nm respectively (Figure 4.8a) with an difference of 137 nm ($\sim$ 395 meV). This energy gap between A and B exciton is greater than what saw for $MoSe_2$ sample in Chapter 2 and, as said in Section 1.2.3, it depends on the strong spin-orbit coupling of tungsten atoms. CVD and mechanically exfoliated monolayer samples displays similar values, with A and B exciton positions of $\sim$747 nm and 602 nm respectively and an A-B splitting of $\sim$400 meV.[46,257] Raman spectroscopy is used to determine sample thickness. WSe_2 displays the typical modes associated to semiconductor polytype, such as 2LA(M)

(second-order longitudinal acoustic Raman mode), $E^1{}_{2g}$, and A_{1g}. As seen for $MoSe_2$ these modes are thickness dependent; moreover a fourth mode, $B^1{}_{2g}$ mode is present only for multilayer samples.[258–260] In a monolayer WSe_2 the two modes $E^1{}_{2g}$ and A_{1g} overlap in a single mode centered at 250 cm^{-1}, starting then diverging while increasing the number of layers[258] while the 2LA(M) mode shows a ~5 cm^{-1} shift towards higher wavenumbers decreasing the layer number; with a Raman shift of ~261 cm^{-1} in a monolayer.[258]
In our sample we found the $E^1{}_{2g}$, and A_{1g} overlapped in a single mode centered at 249.8 cm^{-1}, and the 2LA(M) mode at 260.1 cm^{-1} (Figure 4.8b). A close look on the 290 cm^{-1}-320 cm^{-1} region reveals a small peak centered at 302 cm^{-1} that can't be assigned to the $B^1{}_{2g}$ mode; this mode in fact shows up in bilayers at ∼ 308.5 cm^{-1}, shifting then to higher wavenumbers increasing the layer number.[258] As a result, it is possible to confirm the monolayer nature of the sample. We then explore the sample morphology via TEM imaging (Figure 4.8c) revealing a nanoflower shape, similar to what found in literature for colloidal WSe_2.[239, 240] The last characterization is XPS to determine the presence of oxides and metallic polytype. We found the presence of W signals (Figure 4.9a) associated to either 2H (32.9 eV and 35.1 eV)[222, 251] and 1T (31.8 eV and 33.9 eV)[222, 251] polytype as well as signals associated to WO_3 (centered at 35.8 eV and 38.0 eV).[222] The presence of WO_3 can be traced back to a condensation reaction between OA and OLA; reactions involving metal halides and OLA-OA have been used in the synthesis of metal oxide nanocrystals.[252] The Se (Figure 4.9b) region shows signals associated to 2H (54.3 eV and 55.1 eV)[261] as well as 1T (55.3 eV and 56.1 eV)[262] while the light blue signals centered at 53.5 eV and 54.4 eV can be associated to selenides[263] as well as WSe_3 species.[264]

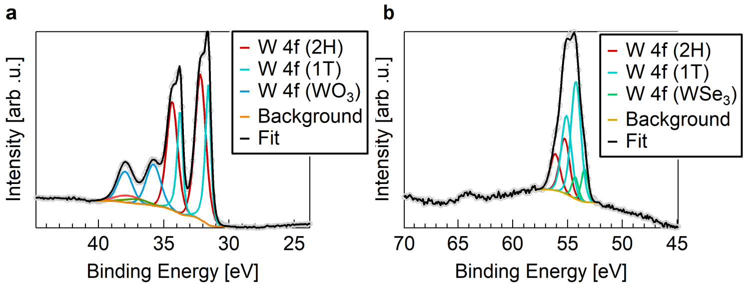

Figure 4.9: XPS spectra of W (a) and Se (b) core levels of WSe_2 nanoflowers.

4.4 Conclusions

In this chapter we have explored the colloidal synthesis of WS_2 and WSe_2 nanosheets. Starting from the WS_2 colloidal synthesis protocol and using the previous knowledge obtained by the work of the master student Diem Van Hamme on the optimization of the colloidal synthesis of WS_2 nanosheets, we translated the protocol on the synthesis of WSe_2 nanosheets. Using UV-Vis absorption spectroscopy, Raman spectroscopy, and TEM, we demonstrated the successful synthesis of semiconducting WSe_2 with monolayer thickness. We explored the sample composition via XPS spectroscopy, finding out the presence of oxides as well as metallic polytype in the sample, which presence ultimately quenches its photoluminescence. Undoubtedly, the synthetic protocol requires further optimization towards either oxides and metallic polytype reduction, nevertheless this can be considered a valuable first step on a colloidal synthesis of monolayer WSe_2.

5

Colloidal Synthesis of $MS_xSe_{(2-x)}$ (M = Mo, W) alloys and $MoS_2/MoSe_2$ heterostructure

5.1 Prologue

In this chapter we will explore some preliminary results on the colloidal synthesis of $MS_xSe_{(2\text{-}x)}$ *(M = Mo, W) alloys and heterostructures. As preliminary results, the main focus is on the synthesis itself, without any further step towards composition and thickness optimization. The use of colloidal synthesis opens a cheap way for the production of* $MS_xSe_{(2\text{-}x)}$ *alloys and heterostructures.*

5.2 Introduction

As discussed in Section 1.2.6, TMDs properties can be tailored in different ways, such as doping, lateral and thickness quantum confinement, and strain engineering. Alloying is a common approach used to tailor material properties, with their composition determining electron band structure and properties. For instance, the continuous insertion of Se in MoS_2 results in a continuous shift of the band gap energy from 1.90 eV to 1.58 eV for pristine $MoSe_2$ and from 2.0 eV to 1.65 eV for W-based TMDs.[84,85] Similar effect is observed in the SOC energy, that monotonically increases from ∼140 meV for pristine MoS_2 to ∼220 meV for pristine $MoSe_2$.[265] As a result, $MS_xSe_{(2\text{-}x)}$ alloys often displays superior qualities compared to their pristine counterparts, such as valley polarization at room temperature,[265] superior quality towards HER reactions[93] or photodetectors with superlinear dependence on light intensity.[92]

Heterostructures are another common way to combine different material properties in a single system. As mentioned in pag. 14 of the introduction, heterostructures are classified according to the relative band alignment of the constituent materials (Type I, *quasi*-Type-II and Type II) and on the type of heterojunction adopted (lateral or vertical heterostructure). According to the heterostructure typology, $MoS_2/MoSe_2$ heterostructure is found to be Type-II in vertical heterostructures[266–270] and Type-I in lateral heterostructures;[271,272] similar band alignment behavior has been found for MoS_2/WSe_2 lateral and vertical heterostructures.[273–275] Moreover, vertical heterostructure band gap transition often shifts from direct to indirect due to stacking effect.[276] Such Type-II systems are characterized by the formation of interlayer excitons with radiative and valley longer than for intralayer excitons,[269,277,278] making them suitable for optoelectronic applications.[270,279] Here we explore the colloidal synthesis of $MoS_xSe_{(2\text{-}x)}$ and $WS_xSe_{(2\text{-}x)}$ starting from the protocols showed in

Chapter 2 and Chapter 4. Moreover, here we also report some tentative of $MoSe_2/MoS_2$ lateral heterostructures.

5.3 $MS_xSe_{(2-x)}$ (M = Mo, W) alloy

5.3.1 Experimental Section

Materials. Molybdenum pentachloride ($MoCl_5$, 99.99%, Sigma-Aldrich), tungsten hexachloride (WCl_6, $\geq$ 99.9%, Sigma-Aldrich), elemental sulfur ($\geq$ 99.95%, Sigma-Aldrich) and selenium ($\geq$ 99.99%, Strem Chemicals), chloroform, and hexamethyldisilazane (HMDS, $\geq$ 99.9%, Sigma-Aldrich) are used without any purification. 1-octadecene (ODE, Sigma-Aldrich), oleic acid (OA, 90%, Sigma-Aldrich), and oleylamine (OLA, 80-90% Acros Organics) are dried using calcium hydride, distilled and stored under nitrogen until further use.

Colloidal Synthesis of $MoS_xSe_{(2-x)}$ alloy. The synthesis is performed under nitrogen using standard Schlenk line techniques. In a 25 ml three-neck flask, a solution of OLA (15 mL), sulfur (10 mg) and selenium (30 mg) is heated up to 290 °C and a solution of $MoCl_5$ in ODE (0.021 g in 1 mL, sonicated until complete dissolution) is injected at 9 mL h^{-1} using a syringe pump. After the injection, the solution is cooled using a water bath. The product is purified three times using a mixture of toluene/isopropanol/acetone, hexane/isopropanol and chloroform/isopropanol respectively, followed by centrifugation at 5000 rpm to collect the sample. The nanosheets are finally dispersed in chloroform and stored in the fridge until further use.

Colloidal Synthesis of $WS_xSe_{(2-x)}$ alloy. The synthesis is performed under nitrogen using standard Schlenk line techniques. 12 mg of WCl_6 are dispersed in 3 mL anhydrous ODE and 0.24 mL of OA while, in a second vial, elemental sulfur (1.6 mg) and selenium (3.3 mg) in 15 mL of anhydrous OLA are mixed together; both solution are then sonicated for 40 min until complete dissolution. The selenium precursor is transferred into a 25 mL three neck flask and heated up at 320 °C. Subsequently, 0.2 mL of HMDS is added to the tungsten precursor solution; this final solution is then injected into the hot S-OLA solution at a 13 mL h^{-1} using a syringe pump. The reaction mixture is held at the selected temperature during all the injection; after it is rapidly cooled to room temperature. The product is purified three times using a mixture of toluene/isopropanol/acetone, hexane/isopropanol and chloroform/isopropanol respectively, followed by centrifugation at 5000 rpm to collect the sample. The nanosheets are finally dispersed in chloroform and stored in the fridge until further use.

Characterization methods. Bright-field TEM images were acquired on a JEOL JEM-1011 microscope operating at an accelerating voltage of 100 kV (for $MoS_xSe_{(2\text{-}x)}$) and on a JEOL JEM-2200FS transmission electron microscope operating at an accelerating voltage of 200 kV (for $WS_xSe_{(2\text{-}x)}$). The samples were prepared by drop-casting of the suspension onto ultrathin C/holey C/Cu TEM grids. Raman spectra were collected with a Bruker Optics 'Senterra' dispersive Raman spectrometer. The spectrometer is coupled to an Olympus BX51 microscope and to a thermoelectrically cooled charge coupled device (CCD) detector, operating at -65 °C. The point measurements were conducted on dried droplets on glass slides and by using the 532 nm laser of the Raman system. The experimental conditions selected were: 5 accumulations of 10 seconds, 3–5 cm^{-1} spectral resolution, 60–1560 cm^{-1} spectral range (40-1540 cm^{-1} for $WS_xSe_{(2\text{-}x)}$), 50 µm pinhole-type aperture, ×50 (NA: 0.75) magnification objective (corresponding to a less than 4 µm spot size) and a 0.20 % laser power (corresponding approx. to 0.12 mW). Ultraviolet-Visible (UV-Vis) absorption spectra of the alloyed nanosheets in chloroform were recorded using a PerkinElmer Lambda 950 spectrometer with a 1 cm path length quartz cuvette.

5.3.2 $MoS_xSe_{(2\text{-}x)}$ alloy

5.3.2.1 Sample Characterization

The UV-Vis spectrum of $MoS_xSe_{(2\text{-}x)}$ (Figure 5.1a) reveals a spectral shape similar to $MoSe_2$ (see Chapter 2), with the presence of the two excitonic features associated to the A and B optical transitions located at 765 nm and 682 nm respectively. A comparison with monolayer $MoSe_2$ spectrum (Figure 5.1b) shows a blue shift of 19 nm and 17 nm respectively; this is associated to the presence of S in the structure.[80] The analysis of the Raman spectrum of $MoS_xSe_{(2\text{-}x)}$ reveals in the region 200 cm^{-1}-300 cm^{-1} the presence of two Raman modes associated to alloyed $MoS_xSe_{(2\text{-}x)}$, located at 229 cm^{-1} and 252 cm^{-1} respectively. These two modes derives from the splitting of the A_{1g} mode of $MoSe_2$ due to the different environment around the Mo atoms,[85,86] which distance decreases while increasing the composition in Se (Figure 5.2). While in $MoSe_2$ the A_{1g} mode splits with the presence of S, in MoS_2 the two modes $E^1{}_{2g}$ and A_{1g} spacing in-

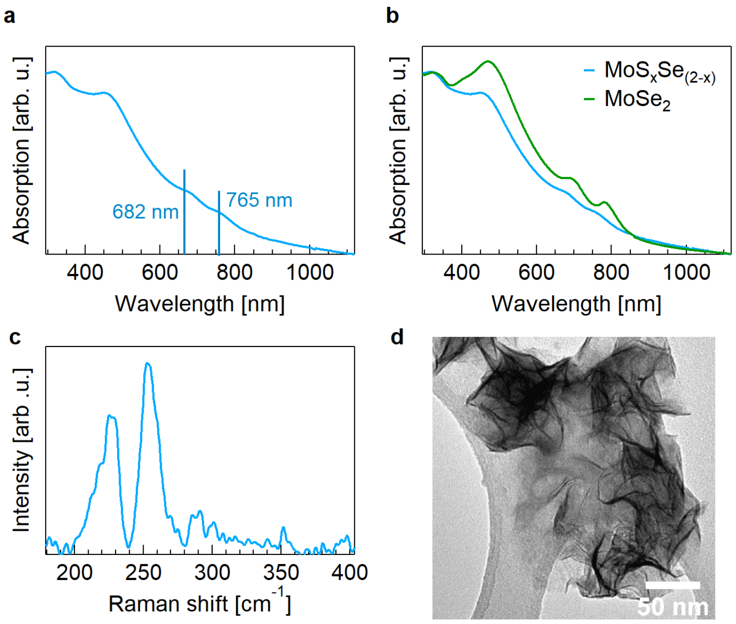

Figure 5.1: (a) UV-Vis absorption spectrum of $MoS_xSe_{(2-x)}$ alloy. (b) Comparison with $MoSe_2$ UV-Vis spectrum. (c) Raman spectrum of $MoS_xSe_{(2-x)}$ alloy. (d) TEM image of the aforementioned sample.

creases due to lattice distortion and strain effect generated by the larger Se atomic radius compared to S atomic radius.[85,91] The sample is further analyze via TEM imaging, to assess the morphology of the sample. The sample displays nanoflower morphology, similar to what seen for $MoSe_2$ nanocrystals, in accordance with the Raman spectrum, suggesting a high composition is Se.

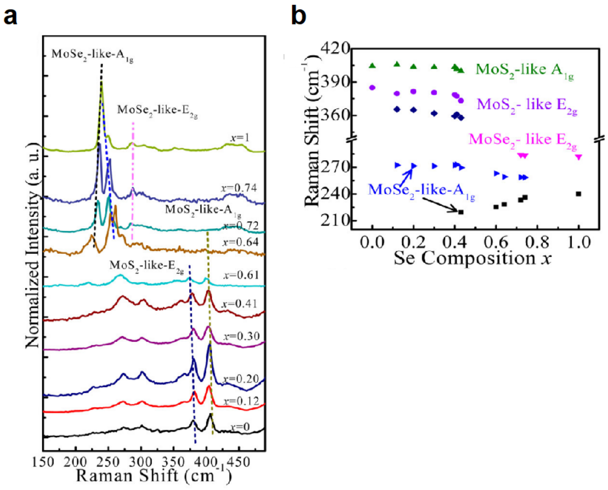

Figure 5.2: (a) Evolution of Raman spectrum with S:Se ratio in MoS$_x$Se$_{(2\text{-}x)}$. (b) Evolution of Raman modes position with Se composition. Adapted from Ref. 86. Copyright 2015 American Chemical Society.

5.3.3 WS$_x$Se$_{(2\text{-}x)}$ alloy

5.3.3.1 Sample Characterization

In Figure 5.3a is reported the UV-Vis spectrum of WS$_x$Se$_{(2\text{-}x)}$ alloy. The sample is characterized by the presence of A and B excitons, located at 690 nm and 565 nm respectively. The exciton energies are blue shifted of 42 nm and 30 nm respectively compared to the monolayer WSe$_2$ sample discussed in Chapter 4, suggesting the presence of S into the structure, similarly to what observed for analogue colloidal samples in literature.[79,87]
Further characterization by Raman spectroscopy reveals the presence of a single A$_{1g}$ Raman mode located at 257 cm^{-1} (assigned to W-Se modes, green region of the spectrum) an E$^1{}_{2g}$ and A$_{1g}$ mode located at 354 cm^{-1} and 406.5 cm^{-1} respectively (assigned to W-S modes, yellow region of the spectrum) and another A$_{1g}$ mode located at 380 cm^{-1} assigned to a S-W-Se mode; this is consistent with monolayer CVD[280–282] and colloidal[79] samples reported in literature. Unfortunately, no study on the Raman variation with thickness is present in literature, making not possible to estimate sample thickness.

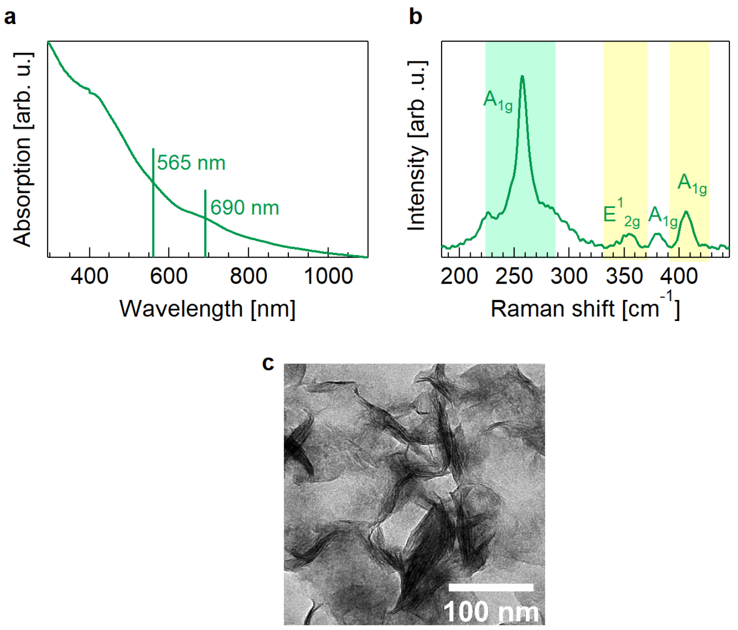

Figure 5.3: (a) UV-Vis absorption spectrum of $WS_xSe_{(2\text{-}x)}$ sample with highlight the two excitons. (b) Raman spectrum of the aforementioned sample with in green the spectral region associated to WSe_2 and in yellow the spectral region associated to WS_2 modes. (c) TEM image of the aforementioned sample.

5.4 MoS_2 /$MoSe_2$ heterostructure

5.4.1 Experimental Section

Materials. Molybdenum pentachloride ($MoCl_5$, 99.99%, Sigma-Aldrich), elemental sulfur ($\geq$ 99.95%, Sigma-Aldrich), and selenium ($\geq$ 99.99%, Strem Chemicals) and chloroform are used without any purification. 1-octadecene (ODE, Sigma-Aldrich), and oleylamine (OLA, 80-90% Acros Organics) are dried using calcium hydride, distilled and stored under nitrogen until further use.

Part I. Colloidal Synthesis of $MoSe_2$. The synthesis is performed under nitrogen using standard Schlenk line techniques. In a 25 ml three-neck flask, a solution of OLA (7 mL) and selenium (10 mg) is heated up to 260 °C and a solution of $MoCl_5$ in ODE (18 mg in 1 mL, sonicated until complete dissolution) is injected at 6 mL h^{-1} using a syringe pump. After the injection, the solution is cooled using a water bath.

Part II. Colloidal Synthesis of $MoSe_2/MoS_2$ heterostructure. To the raw product of Part I, a solution of OLA (7 mL) and sulfur (4 mg) is added in the flask; the resulting solution is heated up to 280 °C and a solution of $MoCl_5$ in ODE (18 mg in 3 mL, sonicated until complete dissolution) is injected at 30 mL h^{-1} using a syringe pump. After the injection, the flask is cooled down using a water bath and the product is purified three times using a mixture of toluene/isopropanol/acetone, hexane/isopropanol and chloroform/isopropanol respectively, followed by centrifugation at 5000 rpm to collect the sample. The nanosheets are finally dispersed in chloroform and stored in the fridge until further use.

Characterization methods. Bright-field TEM images were acquired on a JEOL JEM-1011 microscope operating at an accelerating voltage of 100 kV. Energy-dispersive X-ray spectroscopy (EDS) was carried out with a JEOL EX 24065 JGP. The samples were prepared by drop-casting of the suspension onto ultrathin C/holey C/Cu TEM grids. Raman spectra were collected with a Bruker Optics 'Senterra' dispersive Raman spectrometer. The spectrometer is coupled to an Olympus BX51 microscope and to a thermoelectrically cooled charge coupled device (CCD) detector, operating at -65 °C. The point measurements were conducted on dried droplets on glass slides and by using the 532 nm laser of the Raman system. The experimental conditions selected were: 5 accumulations of 10 seconds, 3–5 cm^{-1} spectral resolution, 60–1560 cm^{-1} spectral range, 50 µm pinhole-type aperture, ×50 (NA: 0.75) magnification objective (corresponding to a less than 4 µm spot size) and a 0.20 % laser power (corresponding approx. to 0.12 mW). Ultraviolet-Visible (UV-Vis) absorption spectra of the nanosheets in chloroform were recorded using a PerkinElmer Lambda 950 spectrometer with a 1 cm path length quartz cuvette.

5.4.1.1 Colloidal Synthesis Protocol

The synthesis strategy consist in the combination of the protocols reported in Chapter 2, divided in two different steps: I) the synthesis of $MoSe_2$, followed by (II) the synthesis of MoS_2. A similar approach have been recently published by Hwang *et al.* on the synthesis of $MoSe_2/WSe_2$ heterostructures.[98]

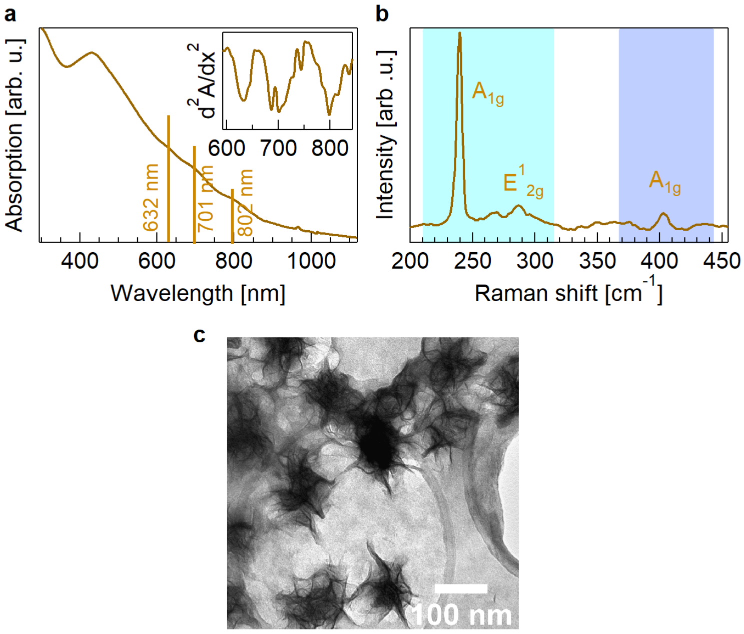

Figure 5.4: (a) UV-Vis absorption spectrum of $MoS_2/MoSe_2$ heterostructure. Inset: second derivative of the 600-850 nm region of the spectrum. (b) Raman spectrum of the aforementioned sample, with in cyan the $MoSe_2$ region and in light blue the MoS_2 region of the spectrum. (c) TEM image of $MoS_2/MoSe_2$ heterostructure.

5.4.1.2 Sample Characterization

The UV-Vis spectrum of the sample displays the presence of 3 different excitonic features, located at 802 nm, 701 nm, and 632 nm (Figure 5.4a). These features are clearly visible in the second derivative of the UV-Vis absorption spectrum (Figure 5.4a, inset); the first two peaks (802 nm and 701 nm) can be associated to the A and B exciton of $MoSe_2$ while the 632 nm can be associated to a red shifted MoS_2 B exciton. Ideally, a perfect heterostructure should shows the features associated to each component,[283–285] however the colloidal protocol can lead to some degree of alloying in both components.

The Raman spectrum (Figure 5.4b) features the modes of both materials, as reported in literature for CVD $MoSe_2/MoS_2$ heterostructures.[98, 269, 286, 287] The cyan region of the spectrum (associated to $MoSe_2$) displays the A_{1g} and $E^1{}_{2g}$ modes, centred at 239.5 cm^{-1} and

287.5 cm^{-1} respectively. The lack of A_{1g} splitting suggest a pure $MoSe_2$ component and not an alloy. The light blue region (associated to MoS_2) reveals the presence of a weak mode at 403 cm^{-1}, assigned to the A_{1g} mode. The lack of $E^1{}_{2g}$ mode and the low intensity of A_{1g} modes suggest the presence of an high defective MoS_2 nanosheet.[196] To visualize the sample composition we performed energy-dispersive X-ray spectroscopy (EDX or EDS) mapping on the sample (Figure 5.5). This technique is based on the emission of a characteristic x-Ray from the element after being irradiated with high-energy electrons. When irradiated, an inner-shell electron from the atoms is removed, leaving a vacancy that is filled by an outer-shell electron. This electron transition causes an energy emission (X-rays in this case) which energy is characteristic of the atom, permitting a mapping of the composition of the sample. In Figure 5.5a is reported the bright-field TEM image of the sample, while in Figure 5.5b and c the EDS mapping of the same spot. The mapping shows that S is distributed across all over the sample while Se is mostly concentrated in the regions where nanoflowers are present; the mapping in combination with Raman modes shape suggests the presence of an heterostructure rather than an alloyed sample.

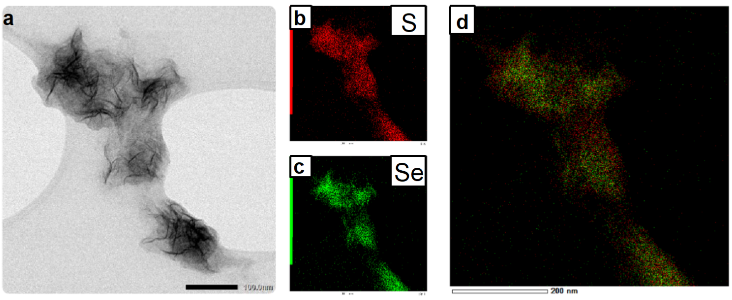

Figure 5.5: Energy-dispersive X-ray spectroscopy of $MoSe_2/MoS_2$ heterostructure. (a) Bright-field TEM image of $MoSe_2/MoS_2$ heterostructure (scalebar: 100 nm). (b) sulfur composition of the selected spot. (c) selenium composition of the selected spot. (d) Overlap of the regions showed in figure b and c (scalebar: 200 nm)

5.4.2 Conclusions

In this chapter we preliminary explored the colloidal synthesis of $MS_xSe_{(2-x)}$ (M = Mo, W) alloys and $MoSe_2/MoS_2$ heterostructure. In the case of $MS_xSe_{(2-x)}$ alloys, using the pre-existent colloidal protocols for MoS_2 and WSe_2 synthesis and adding a second chalcogenide, we obtained the alloyed materials. Using UV-Vis and Raman spectroscopy, we confirmed the semiconducting nature of both samples, with the absorption spectrum displaying the typical excitonic features expected for the semiconducting polytype, with energies in between MoS_2 and $MoSe_2$ (for $MS_xSe_{(2-x)}$) band gaps and between WS_2 and WSe_2 band gaps for $WS_xSe_{(2-x)}$, as expected for alloyed samples. In addition, the presence of the two Raman modes for $MoS_xSe_{(2-x)}$ (derived from the splitting of the A_{1g} mode of $MoSe_2$ due to the S doping) and both modes from the sulfide and selenide species for $WS_xSe_{(2-x)}$ confirms this attribution. Moreover, we preliminary explored the colloidal synthesis of $MoSe_2/MoS_2$ heterostructure, combining the synthesis protocols of the pristine materials reported in Chapter 2. Using UV-Vis absorption and Raman spectroscopy we confirmed the presence of pristine MoS_2 and $MoSe_2$ in the sample with the appropriate semiconducting polytype. The absorption spectrum showed the presence of three different excitonic features, ascribed to MoS_2 and $MoSe_2$ while the Raman spectrum displayed the modes associated to the pristine materials, excluding the presence of alloys. Via EDX mapping we found the presence of overlapping regions covered by the two chalcogenide species, suggesting a vertical heterostructured material. Despite the early stages of the research, these results suggest how the colloidal synthesis can be, in a long run, a cheap and valid alternative on the production of alloyed and heterostructured nanocrystals.

6

Conclusions and Perspectives

6.1 General Conclusions

While the role of TMDs in technological application is consolidated, the development of a suitable colloidal protocol for the synthesis of such materials is still in early stage. The *leitmotif* of this thesis is the exploration of the colloidal synthesis of G6-TMDs, starting from the colloidal synthesis of MoS_2. The development of a suitable protocol, using the Design Of Experiment approach, yielded to a deeper understanding on the dynamics involved in the synthesis, such as effect of temperature, injection rate, chalcogen precursor, ligand volume, degassing time and degassing temperature on the final properties (and quality) of the nanocrystal, maintaining to a low number of experimental work required. Using such knowledge we ultimately developed an optimized protocol for the synthesis of MoS_2 nanosheets characterized by exciton energy close to monolayer band gap and a sample thickness composition of mono- and bilayer nanosheets. The translation of this protocol to the selenide counterpart yet yielded to $MoSe_2$ nanosheets characterized by excitons energy close to monolayer band gap and monolayer thickness. Moreover, the analysis of MoS_2 and $MoSe_2$ photoluminescence (after hBN encapsulation) at cryogenic and room temperature displayed the presence, for both materials, of an exciton emission centred at 1.96 eV and 1.68 eV respectively (in line with what expected for mono- and bilayer nanosheets) characterized by a progressive red shift in energy and line width broadening going from 4 K to 295 K, with $MoSe_2$ displaying smaller FWHM compared to MoS_2 sample.

Using such protocols as new starting point on our research, we tried to further optimize the synthesis of MoS_2 nanosheets towards the reduction of the lateral dimensions. We simplify the protocol removing the degassing stage and decreasing the S:Mo stoichiometric ratio of the reaction to 2. The resulting nanosheets displayed a lateral size of 11.45 nm ± 4.89 nm, as visible from the small background scattering in the UV-Vis absorption spectrum, and, similarly to the DOE optimized MoS_2, mono- and bilayer nanosheets composition. The absorption spectrum features both A and B excitons, located at 651 nm and 603 nm respectively, are close to what expected for monolayer MoS_2 nanosheets; moreover the comparison with similar samples reveals the presence of a clear trend between lateral size and A exciton position. The nanosheets displayed photoluminescence at 80 K, characterized by a resolved trion and a neutral exciton emission centred at 1.91 eV and 1.97 eV, and a FWHM of 66 meV and 42 meV respectively, suggesting a lower defect density compared to the DOE optimized MoS_2 nanosheets.

These results led us on landing on tungsten-based TMDs. We proceed on exploring the synthesis and optimization of WS_2 and WSe_2 nanosheets, in a similar way done for MoS_2 and $MoSe_2$ samples. The DOE optimization done by the master student Diem Van Hamme on the colloidal synthesis of WS_2 nanosheets provided valuable known-how for the subsequent colloidal synthesis of WSe_2 nanosheets. Starting from the DOE-optimized WS_2 protocol, we were able to synthesize WSe_2 nanosheets characterized by A and B exciton features in the UV-Vis absorption spectrum centred at 732 nm and 595 nm, close to what expected for monolayer WSe_2 nanosheets, and a monolayer thickness. The lack of photoluminescence was investigated by XPS, that revealed the presence of metallic phase as well as oxides. Once again, the colloidal method have been proved to be a suitable method for the production of TMDs. As last part of our journey, we dove into TMDs alloys and heterostructures. Using the optimized protocol developed for Mo- and W-based TMDs, we moved from the pristine materials to their alloys. The two alloys, MoS_xSe_{2-x} and WS_xSe_{2-x}, obtained adding elemental selenium to the sulfide protocols, displayed the expected characteristics from such materials, such as exciton energies in between monolayer MoS_2 and $MoSe_2$ nanosheets, and the presence of specific Raman modes (splitted A_{1g} mode for MoS_xSe_{2-x} and sulfide and selenide modes for WS_xSe_{2-x}). The last chapter of the story is the synthesis of $MoSe_2/MoS_2$ heterostructure, obtained combining the two protocols discussed at the beginning. Such combination resulted in a sample displaying the characteristics of both materials, such as different sets of excitonic features and Raman modes associated to MoS_2 and $MoSe_2$ nanosheets, with confirmation via EDS of the presence of an heterostructured material.

To summarize, the flexibility of colloidal synthesis, assisted by the Design Of Experiment approach, allowed us to (almost) explore the synthesis of the entire G6-TMDs family. The potential of this synthetic pathway on TMD synthesis ultimately explains the interest of the scientific community and the great efforts made on finally understanding (and exploiting) such synthesis method.

6.2 Perspectives - What's next?

After having confirmed the validity of the colloidal synthesis as production method for TMDs, the next step is to focus on further optimization and tuning of their properties. In the following sections we will discuss outlook and perspectives on such materials, focusing on suitable topics for future research work.

6.2.1 Further synthesis optimization via DOE

The optimization of MoS_2 synthesis has displayed the potential of the DOE application on chemical synthesis. The application of such approach on WSe_2 and alloys/heterostructures synthesis can be certainly beneficial, yielding to a deeper understanding on the effect of the synthesis parameters on sample quality and properties, reducing at the same time the amount of experimental work required for the optimization. The same approach can be applied on the already optimized MoS_2 and $MoSe_2$ nanocrystals, centering the DSD framework on the already optimized protocol, to explore the surroundings of the reactions space and find new synthesis conditions that can further improve the material qualities.

6.2.2 Chemical doping to enhance photoluminescence

As introduced in Section 1.2.5, TMDs photoluminescence can be tuned via chemical doping, used to passivate the trap states and reduce the nonradiative recombination, ultimately making possible a near-unity quantum yield in MoS_2.[54] Despite this simple concept, the execution is not trivial (due to the presence of capping ligands on the nanocrystal), thus requiring extensive work on finding a suitable approach on the doping. Literature reports already several different doping protocols with different dopant molecules, however such procedures are often applied on exfoliated or CVD-made TMDs.[65, 71, 72, 288, 289] Initial trials have been done, post-synthesis, using F_4TCNQ dissolved in toluene and dropcasted on deposited MoS_2.[72] Despite the promising results on exfoliated MoS_2 reported in literature, no photoluminescence enhancement has been detected. Nevertheless, a study on the implementation of a doping protocol on the colloidal synthesis of TMDs would be beneficial, opening multiple pathways on colloidal TMDs optoelectronic applications.

6.2.3 TMDs colloidal heterostructures

As saw in Chapter 5 and already reported from Hwang *et al.*,[98] colloidal synthesis can provide a valid pathway for the synthesis of heterostructures, although limited to a core-shell-like structure. While the state-of-the art of such structures involves production techniques as CVD (capable to provide either lateral or vertical heterostructures) or *ex-situ* vertical stacking,[100, 290] few trials are present in literature regarding *in situ* colloidal heterostructures. A DOE study on the synthesis of heterostructure may be possible, optimizing either both stages (core and crown synthesis) or only the crowning stage. In the latter case, a DOE study towards the optimal conditions where a crown can be grown avoiding co-nucleation, retaining at the same time the semiconducting polytype would be beneficial. The factors to include into such design would be the same explored in Chapter 2, adding the concentration of the cores to the factor list. To evaluate the results of such studies, possible metrics that may be used are EDS mapping on single nanocrystals as well as the change in PL; in fact a Type II structure is characterized by a red shifted emission compared to the pristine components as well as by a longer emission lifetime. Overall, further studies on this direction may be beneficial, leading to cheaper and easier way to produce heterostructured materials and boost their technological use.

6.2.4 Extension of the laterally-confined 2D TMDs library

The exploration of the synthesis of laterally-confined MoS_2 in Chapter 3 showed that reduced lateral dimensions yielded to a general improvement of the optoelectronic properties, with the aforementioned sample displaying narrow excitons, lower background scattering and, more importantly, photoluminescence properties characterized by well-resolved trion and neutral exciton emissions. Such results, in addition to the exploratory results reported in literature, makes interesting to further develop efficient strategies to control the lateral dimensions of the nanosheets, as well as expanding such studies to the entire TMDs library.

6.3 Scientific output

Peer reviewed articles

1. G. Pippia; A. Rousaki; M. Barbone; J. Billet; R. Brescia; A. Polovitsyn; B. Martín-García; M. Prato; F. De Boni; M. M. Petrić; A. Ben Mhenni; I. Van Driessche; P. Vandenabeele; K. Müller; and I. Moreels. Colloidal Continuous Injection Synthesis of Fluorescent MoX_2 (X = S, Se) Nanosheets as a First Step Toward Photonic Applications. *ACS Appl. Nano Materials*, 2022, 5, 8, 10311–10320.

2. G. Pippia; D. Van Hamme; B. Martin-Garcia; M. Prato; and I. Moreels. A Colloidal Route to Red Tungsten Disulfide Nanosheets with Monolayer Thickness. *Nanoscale*, 2022, **14**, 15859-15868.

Conference contributions

Oral presentations

1. G. Pippia; A. Rousaki; M. Barbone; J. Billet; R. Brescia; A. Polovitsyn; B. Martín-García; M. M. Petrić; A. Ben Mhenni; I. Van Driessche; P. Vandenabeele; K. Müller; and I. Moreels. Colloidal Synthesis of Fluorescent MoX_2 (X = S, Se) Nanosheets Via a Design of Experiments Approach. *NanoGe Fall Meeting*, **2021**.

2. G. Pippia; A. Rousaki; M. Barbone; J. Billet; R. Brescia; A. Polovitsyn; B. Martín-García; M. M. Petrić; A. Ben Mhenni; I. Van Driessche; P. Vandenabeele; K. Müller; and I. Moreels. Colloidal Synthesis Of Fluorescent MoX_2 (X = S, Se) Nanosheets Via a Design Of Experiments Approach. *NanoGe Spring Meeting*, **2022**.

3. G. Pippia; A. Rousaki; M. Barbone; J. Billet; R. Brescia; A. Polovitsyn; B. Martín-García; M. M. Petrić; A. Ben Mhenni; I. Van Driessche; P. Vandenabeele; K. Müller; and I. Moreels. Colloidal Synthesis of Fluorescent Monolayer MoX_2 (X = S, Se) Nanosheets Via a Design of Experiments Approach. *E-MRS Spring Meeting*, **2022**.

Poster presentations

1. G. Pippia; A. Rousaki; M. Barbone; J. Billet; R. Brescia; A. Polovitsyn; B. Martín-García; M. M. Petrić; A. Ben Mhenni; I. Van Driessche; P. Vandenabeele; K. Müller; and I. Moreels. Colloidal synthesis optimization of mono- and few-layer MoX_2 ($X = S, Se$) nanosheets via design of experiment approach. *ACS SPRING*, **2021**.

Bibliography

[1] Nick Holonyak Jr and S Fo Bevacqua. *Coherent (visible) light emission from* $Ga(As_{1\text{-}x}P_{x})$ *junctions.* Applied Physics Letters, 1(4):82–83, 1962.

[2] Giora Rytwo. *Clay minerals as an ancient nanotechnology: historical uses of clay organic interactions, and future possible perspectives.* Macla, 9:15–17, 2008.

[3] A J Nozik. *Photoelectrochemistry: Applications to Solar Energy Conversion.* Annual Review of Physical Chemistry, 29(1):189–222, 1978.

[4] Z Alfassi, D Bahnemann, and A Henglein. *Photochemistry of colloidal metal sulfides. 3. Photoelectron emission from cadmium sulfide and cadmium sulfide-zinc sulfide cocolloids.* The Journal of Physical Chemistry, 86(24):4656–4657, 1982.

[5] Michael Grätzel. *Photochemical methods for the conversion of light into chemical energy.* Berichte der Bunsengesellschaft für physikalische Chemie, 84(10):981–991, 1980.

[6] AA Onushchenko and AI Ekimov. *Quantum size effect in three dimensional microscopic semiconductor crystals.* JETP lett, 34:345, 1981.

[7] Alexander L Efros and Al L Efros. *Interband absorption of light in a semiconductor sphere.* Sov. Phys. Semicond, 16(7):772–775, 1982.

[8] Tadashi Itoh and Toshio Kirihara. *Excitons in CuCl microcrystals embedded in NaCl.* Journal of Luminescence, 31:120–122, 1984.

[9] R Rossetti, S Nakahara, and Louis E Brus. *Quantum size effects in the redox potentials, resonance Raman spectra, and electronic spectra of CdS crystallites in aqueous solution.* The Journal of Chemical Physics, 79(2):1086–1088, 1983.

[10] Louis Brus. *Electronic wave functions in semiconductor clusters: experiment and theory.* The Journal of Physical Chemistry, 90(12):2555–2560, 1986.

[11] Louis E Brus. *Electron–electron and electron-hole interactions in small semiconductor crystallites: The size dependence of the lowest excited electronic state.* The Journal of chemical physics, 80(9):4403–4409, 1984.

[12] CBea Murray, David J Norris, and Moungi G Bawendi. *Synthesis and characterization of nearly monodisperse CdE (E= sulfur, selenium, tellurium) semiconductor nanocrystallites.* Journal of the American Chemical Society, 115(19):8706–8715, 1993.

[13] Nikolai Gaponik, Dmitri V Talapin, Andrey L Rogach, Kathrin Hoppe, Elena V Shevchenko, Andreas Kornowski, Alexander Eychmüller, and Horst Weller. *Thiol-capping of CdTe nanocrystals: an alternative to organometallic synthetic routes.* The Journal of Physical Chemistry B, 106(29):7177–7185, 2002.

[14] Margaret A Hines and Philippe Guyot-Sionnest. *Synthesis and characterization of strongly luminescing ZnS-capped CdSe nanocrystals.* The Journal of Physical Chemistry, 100(2):468–471, 1996.

[15] Katherine Bourzac et al. *Quantum dots go on display.* Nature, 493(7432):283, 2013.

[16] Freddy T Rabouw and Celso de Mello Donega. *Excited-state dynamics in colloidal semiconductor nanocrystals.* Photoactive Semiconductor Nanocrystal Quantum Dots, pages 1–30, 2017.

[17] K. S. Novoselov, A. K. Geim, S. V. Morozov, D. Jiang, Y. Zhang, S. V. Dubonos, I. V. Grigorieva, and A. A. Firsov. *Electric field effect in atomically thin carbon films.* Science (New York, N.Y.), 306(5696):666–9, 2004.

[18] K. F. Mak, C. Lee, J. Hone, J. Shan, and T. F. Heinz. *Atomically thin MoS(2): a new direct-gap semiconductor.* Physical review letters, 105(13):136805, 2010.

[19] Andrea Splendiani, Liang Sun, Yuanbo Zhang, Tianshu Li, Jonghwan Kim, Chi-Yung Chim, Giulia Galli, and Feng Wang. *Emerging photoluminescence in monolayer MoS2.* Nano letters, 10(4):1271–1275, 2010.

[20] Wonbong Choi, Nitin Choudhary, Gang Hee Han, Juhong Park, Deji Akinwande, and Young Hee Lee. *Recent development of two-dimensional transition metal dichalcogenides and their applications.* Materials Today, 20(3):116–130, 2017.

[21] Nitin Babu Shinde, Beo Deul Ryu, Kalaiarasan Meganathan, Bellarmine Francis, Chang-Hee Hong, S Chandramohan, and Senthil Kumar Eswaran. *Large-scale atomically thin monolayer 2H-MoS2 field-effect transistors.* ACS Applied Nano Materials, 3(8):7371–7376, 2020.

[22] Lunfeng Chen, Hanghang Feng, Rui Zhang, Suhang Wang, Xueyan Zhang, Zhijie Wei, Yuanmin Zhu, Meng Gu, and Chenyang Zhao. *Phase-controlled synthesis of 2H/3R-MoSe2 nanosheets on P-doped carbon for synergistic hydrogen evolution.* ACS Applied Nano Materials, 3(7):6516–6523, 2020.

[23] D. Son, S. I. Chae, M. Kim, M. K. Choi, J. Yang, K. Park, V. S. Kale, J. H. Koo, C. Choi, M. Lee, J. H. Kim, T. Hyeon, and D. H. Kim. *Colloidal Synthesis of Uniform-Sized Molybdenum Disulfide Nanosheets for Wafer-Scale Flexible Nonvolatile Memory.* Advanced materials (Deerfield Beach, Fla.), 28(42):9326–9332, 2016.

[24] Yu Ye, Zi Jing Wong, Xiufang Lu, Xingjie Ni, Hanyu Zhu, Xianhui Chen, Yuan Wang, and Xiang Zhang. *Monolayer excitonic laser.* Nature Photonics, 9(11):733–737, 2015.

[25] Wenxu Yin, Xue Bai, Xiaoyu Zhang, Jia Zhang, Xupeng Gao, and William W. Yu. *Multicolor Light-Emitting Diodes with MoS_2 Quantum Dots.* Particle & Particle Systems Characterization, 36(2), 2019.

[26] Áine Coogan and Yurii K Gun'ko. *Solution-based "bottom-up" synthesis of group VI transition metal dichalcogenides and their applications.* Materials Advances, 2(1):146–164, 2021.

[27] Bhakti Jariwala, Damien Voiry, Apoorv Jindal, Bhagyashree A Chalke, Rudheer Bapat, Arumugam Thamizhavel, Manish Chhowalla, Mandar Deshmukh, and Arnab Bhattacharya. *Syn-*

thesis and characterization of ReS_2 and $ReSe_2$ layered chalcogenide single crystals. Chemistry of Materials, 28(10):3352–3359, 2016.

[28] Manish Chhowalla, Hyeon Suk Shin, Goki Eda, Lain-Jong Li, Kian Ping Loh, and Hua Zhang. *The chemistry of two-dimensional layered transition metal dichalcogenide nanosheets.* Nature chemistry, 5(4):263–275, 2013.

[29] J. A. Wilson and A. D. Yoffe. *The transition metal dichalcogenides discussion and interpretation of the observed optical, electrical and structural properties.* Advances in Physics, 18(73):193–335, 1969.

[30] Chaoyi Yan, Chuanhui Gong, Peihua Wangyang, Junwei Chu, Kai Hu, Chaobo Li, Xuepeng Wang, Xinchuan Du, Tianyou Zhai, Yanrong Li, et al. *2D group IVB transition metal dichalcogenides.* Advanced Functional Materials, 28(39):1803305, 2018.

[31] Fuhua Li and Qing Tang. *Modulating the electronic structure and in-plane activity of two-dimensional transition metal dichalcogenide (MoS2, TaS2, NbS2) monolayers by interfacial engineering.* The Journal of Physical Chemistry C, 124(16):8822–8833, 2020.

[32] Xiumei Geng, Weiwei Sun, Wei Wu, Benjamin Chen, Alaa Al-Hilo, Mourad Benamara, Hongli Zhu, Fumiya Watanabe, Jingbiao Cui, and Tar-pin Chen. *Pure and stable metallic phase molybdenum disulfide nanosheets for hydrogen evolution reaction.* Nature communications, 7(1):1–7, 2016.

[33] Wei Zhao, Jie Pan, Yuqiang Fang, Xiangli Che, Dong Wang, Kejun Bu, and Fuqiang Huang. *Metastable MoS_2: crystal structure, electronic band structure, synthetic approach and intriguing physical properties.* Chemistry–A European Journal, 24(60):15942–15954, 2018.

[34] Lei Wang, Zhuo Wang, Hai-Yu Wang, Gustavo Grinblat, Yu-Li Huang, Dan Wang, Xiao-Hui Ye, Xian-Bin Li, Qiaoliang Bao, AndrewThye-Shen Wee, et al. *Slow cooling and efficient extraction of C-exciton hot carriers in MoS_2 monolayer.* Nature communications, 8(1):1–8, 2017.

[35] Beom Seo Kim, Jun-Won Rhim, Beomyoung Kim, Changyoung Kim, and Seung Ryong Park. *Determination of the band param-*

eters of bulk 2H-MX2 (M= Mo, W; X= S, Se) by angle-resolved photoemission spectroscopy. Scientific reports, 6(1):1–7, 2016.

[36] Zhiyong Y Zhu, Yingchun C Cheng, and Udo Schwingenschlögl. *Giant spin-orbit-induced spin splitting in two-dimensional transition-metal dichalcogenide semiconductors.* Physical Review B, 84(15):153402, 2011.

[37] JA Reyes-Retana and Felipe Cervantes-Sodi. *Spin-orbital effects in metal-dichalcogenide semiconducting monolayers.* Scientific reports, 6(1):1–10, 2016.

[38] A Carvalho, RM Ribeiro, and AH Castro Neto. *Band nesting and the optical response of two-dimensional semiconducting transition metal dichalcogenides.* Physical Review B, 88(11):115205, 2013.

[39] Lijun Zhang and Alex Zunger. *Evolution of electronic structure as a function of layer thickness in group-VIB transition metal dichalcogenides: emergence of localization prototypes.* Nano Letters, 15(2):949–957, 2015.

[40] Y. Zhang, T. R. Chang, B. Zhou, Y. T. Cui, H. Yan, Z. Liu, F. Schmitt, J. Lee, R. Moore, Y. Chen, H. Lin, H. T. Jeng, S. K. Mo, Z. Hussain, A. Bansil, and Z. X. Shen. *Direct observation of the transition from indirect to direct bandgap in atomically thin epitaxial MoSe2.* Nature nanotechnology, 9(2):111–5, 2014.

[41] Abe D Yoffe. *Low-dimensional systems: quantum size effects and electronic properties of semiconductor microcrystallites (zero-dimensional systems) and some quasi-two-dimensional systems.* Advances in Physics, 42(2):173–262, 1993.

[42] Ben G Yacobi. *Semiconductor materials: an introduction to basic principles.* Springer Science & Business Media, 2003.

[43] Changjian Zhang, Haining Wang, Weimin Chan, Christina Manolatou, and Farhan Rana. *Absorption of light by excitons and trions in monolayers of metal dichalcogenide Mo S 2: Experiments and theory.* Physical Review B, 89(20):205436, 2014.

[44] RA Neville and BL Evans. *The Band Edge Excitons in 2H-*MoS_2. physica status solidi (b), 73(2):597–606, 1976.

[45] Hongyan Shi, Rusen Yan, Simone Bertolazzi, Jacopo Brivio, Bo Gao, Andras Kis, Debdeep Jena, Huili Grace Xing, and

Libai Huang. *Exciton dynamics in suspended monolayer and few-layer MoS2 2D crystals.* ACS nano, 7(2):1072–1080, 2013.

[46] Y. Niu, S. Gonzalez-Abad, R. Frisenda, P. Marauhn, M. Druppel, P. Gant, R. Schmidt, N. S. Taghavi, D. Barcons, A. J. Molina-Mendoza, S. M. de Vasconcellos, R. Bratschitsch, D. Perez De Lara, M. Rohlfing, and A. Castellanos-Gomez. *Thickness-Dependent Differential Reflectance Spectra of Monolayer and Few-Layer MoS(2), MoSe(2), WS(2) and WSe(2).* Nanomaterials (Basel, Switzerland), 8(9), 2018.

[47] Kevin Synnatschke, Patrick Arthur Cieslik, Andrew Harvey, Andres Castellanos-Gomez, Tian Tian, Chih-Jen Shih, Alexey Chernikov, Elton J. G. Santos, Jonathan N. Coleman, and Claudia Backes. *Length- and Thickness-Dependent Optical Response of Liquid-Exfoliated Transition Metal Dichalcogenides.* Chemistry of Materials, 31(24):10049–10062, 2019.

[48] Tawinan Cheiwchanchamnangij and Walter R. L. Lambrecht. *Quasiparticle band structure calculation of monolayer, bilayer, and bulk* MoS_2. Physical Review B, 85(20), 2012.

[49] Ashwin Ramasubramaniam. *Large excitonic effects in monolayers of molybdenum and tungsten dichalcogenides.* Physical Review B, 86(11):115409, 2012.

[50] Yiling Yu, Yifei Yu, Yongqing Cai, Wei Li, Alper Gurarslan, Hartwin Peelaers, David E Aspnes, Chris G Van de Walle, Nhan V Nguyen, Yong-Wei Zhang, et al. *Exciton-dominated dielectric function of atomically thin MoS2 films.* Scientific reports, 5(1):1–7, 2015.

[51] Guang Yi Jia, Yue Liu, Jing Yu Gong, Dang Yuan Lei, Dan Li Wang, and Zhen Xian Huang. *Excitonic quantum confinement modified optical conductivity of monolayer and few-layered* MoS_2. Journal of Materials Chemistry C, 4(37):8822–8828, 2016.

[52] Gang Wang, Alexey Chernikov, Mikhail M Glazov, Tony F Heinz, Xavier Marie, Thierry Amand, and Bernhard Urbaszek. *Colloquium: Excitons in atomically thin transition metal dichalcogenides.* Reviews of Modern Physics, 90(2):021001, 2018.

[53] Ermin Malic, Malte Selig, Maja Feierabend, Samuel Brem, Dominik Christiansen, Florian Wendler, Andreas Knorr, and Gunnar Berghäuser. *Dark excitons in transition metal dichalcogenides.* Physical Review Materials, 2(1):014002, 2018.

[54] Matin Amani, Der-Hsien Lien, Daisuke Kiriya, Jun Xiao, Angelica Azcatl, Jiyoung Noh, Surabhi R Madhvapathy, Rafik Addou, Santosh Kc, Madan Dubey, et al. *Near-unity photoluminescence quantum yield in MoS2.* Science, 350(6264):1065–1068, 2015.

[55] Jinhua Hong, Zhixin Hu, Matt Probert, Kun Li, Danhui Lv, Xinan Yang, Lin Gu, Nannan Mao, Qingliang Feng, Liming Xie, et al. *Exploring atomic defects in molybdenum disulphide monolayers.* Nature communications, 6(1):1–8, 2015.

[56] Anja Förster, Sibylle Gemming, Gotthard Seifert, and David Tománek. *Chemical and electronic repair mechanism of defects in* MoS_2 *monolayers.* ACS nano, 11(10):9989–9996, 2017.

[57] Arend M Van Der Zande, Pinshane Y Huang, Daniel A Chenet, Timothy C Berkelbach, YuMeng You, Gwan-Hyoung Lee, Tony F Heinz, David R Reichman, David A Muller, and James C Hone. *Grains and grain boundaries in highly crystalline monolayer molybdenum disulphide.* Nature materials, 12(6):554–561, 2013.

[58] Wu Zhou, Xiaolong Zou, Sina Najmaei, Zheng Liu, Yumeng Shi, Jing Kong, Jun Lou, Pulickel M Ajayan, Boris I Yakobson, and Juan-Carlos Idrobo. *Intrinsic structural defects in monolayer molybdenum disulfide.* Nano letters, 13(6):2615–2622, 2013.

[59] Jing Yang, Fabio Bussolotti, Hiroyo Kawai, and Kuan Eng Johnson Goh. *Tuning the conductivity type in monolayer* WS_2 *and* MoS_2 *by sulfur vacancies.* physica status solidi (RRL)–Rapid Research Letters, 14(9):2000248, 2020.

[60] Xixia Zhang, Shanpeng Wang, Chao-Kuei Lee, Cheng-Maw Cheng, Jia-Chi Lan, Xinru Li, Jie Qiao, and Xutang Tao. *Unravelling the effect of sulfur vacancies on the electronic structure of the* MoS_2 *crystal.* Physical Chemistry Chemical Physics, 22(38):21776–21783, 2020.

[61] Linqiu Li, Run Long, and Oleg V Prezhdo. *Why chemical vapor deposition grown MoS2 samples outperform physical vapor de-*

position samples: time-domain ab initio analysis. Nano Letters, 18(6):4008–4014, 2018.

[62] Akash Singh and Abhishek Kumar Singh. *Origin of n-type conductivity of monolayer MoS_2.* Physical Review B, 99(12):121201, 2019.

[63] Kapildeb Dolui, Ivan Rungger, and Stefano Sanvito. *Origin of the n-type and p-type conductivity of MoS_2 monolayers on a SiO_2 substrate.* Physical review B, 87(16):165402, 2013.

[64] Qiang Li, Yinghe Zhao, Chongyi Ling, Shijun Yuan, Qian Chen, and Jinlan Wang. *Towards a comprehensive understanding of the reaction mechanisms between defective MoS_2 and thiol molecules.* Angewandte Chemie International Edition, 56(35):10501–10505, 2017.

[65] Shinichiro Mouri, Yuhei Miyauchi, and Kazunari Matsuda. *Tunable photoluminescence of monolayer MoS_2 via chemical doping.* Nano letters, 13(12):5944–5948, 2013.

[66] Ong Kim Le, Viorel Chihaia, Vo Van On, et al. *N-type and p-type molecular doping on monolayer MoS_2.* RSC advances, 11(14):8033–8041, 2021.

[67] Dong Min Sim, Mincheol Kim, Soonmin Yim, Min-Jae Choi, Jaesuk Choi, Seunghyup Yoo, and Yeon Sik Jung. *Controlled doping of vacancy-containing few-layer MoS2 via highly stable thiol-based molecular chemisorption.* ACS nano, 9(12):12115–12123, 2015.

[68] Emily P Nguyen, Benjamin J Carey, Jian Zhen Ou, Joel van Embden, Enrico Della Gaspera, Adam F Chrimes, Michelle JS Spencer, Serge Zhuiykov, Kourosh Kalantar-zadeh, and Torben Daeneke. *Electronic tuning of 2D MoS2 through surface functionalization.* Advanced Materials, 27(40):6225–6229, 2015.

[69] Arelo OA Tanoh, Jack Alexander-Webber, Ye Fan, Nicholas Gauriot, James Xiao, Raj Pandya, Zhaojun Li, Stephan Hofmann, and Akshay Rao. *Giant photoluminescence enhancement in $MoSe_2$ monolayers treated with oleic acid ligands.* Nanoscale Advances, 3(14):4216–4225, 2021.

[70] Shrawan Roy, Wooseon Choi, Sera Jeon, Do-Hwan Kim, Hyun Kim, Seok Joon Yun, Yongjun Lee, Jaekwang Lee, Young-Min

Kim, and Jeongyong Kim. *Atomic observation of filling vacancies in monolayer transition metal sulfides by chemically sourced sulfur atoms.* Nano Letters, 18(7):4523–4530, 2018.

[71] Hau-Vei Han, Ang-Yu Lu, Li-Syuan Lu, Jing-Kai Huang, Henan Li, Chang-Lung Hsu, Yung-Chang Lin, Ming-Hui Chiu, Kazu Suenaga, Chih-Wei Chu, et al. *Photoluminescence enhancement and structure repairing of monolayer MoSe2 by hydrohalic acid treatment.* Acs Nano, 10(1):1454–1461, 2016.

[72] Shinichiro Mouri, Yuhei Miyauchi, and Kazunari Matsuda. *Chemical doping modulation of nonlinear photoluminescence properties in monolayer MoS2.* Applied Physics Express, 9(5):055202, 2016.

[73] Yongqing Cai, Hangbo Zhou, Gang Zhang, and Yong-Wei Zhang. *Modulating carrier density and transport properties of MoS2 by organic molecular doping and defect engineering.* Chemistry of Materials, 28(23):8611–8621, 2016.

[74] Ye Wang, Amine Slassi, Marc-Antoine Stoeckel, Simone Bertolazzi, Jerôme Cornil, David Beljonne, and Paolo Samorì. *Doping of monolayer transition-metal dichalcogenides via physisorption of aromatic solvent molecules.* The Journal of Physical Chemistry Letters, 10(3):540–547, 2019.

[75] Haiyan Nan, Zilu Wang, Wenhui Wang, Zheng Liang, Yan Lu, Qian Chen, Daowei He, Pingheng Tan, Feng Miao, Xinran Wang, et al. *Strong photoluminescence enhancement of MoS2 through defect engineering and oxygen bonding.* ACS nano, 8(6):5738–5745, 2014.

[76] Sefaattin Tongay, Jian Zhou, Can Ataca, Jonathan Liu, Jeong Seuk Kang, Tyler S Matthews, Long You, Jingbo Li, Jeffrey C Grossman, and Junqiao Wu. *Broad-range modulation of light emission in two-dimensional semiconductors by molecular physisorption gating.* Nano letters, 13(6):2831–2836, 2013.

[77] Saujan V Sivaram, Aubrey T Hanbicki, Matthew R Rosenberger, Glenn G Jernigan, Hsun-Jen Chuang, Kathleen M McCreary, and Berend T Jonker. *Spatially selective enhancement of photoluminescence in MoS2 by exciton-mediated adsorption and defect passivation.* ACS applied materials & interfaces, 11(17):16147–16155, 2019.

[78] Namphung Peimyoo, Weihuang Yang, Jingzhi Shang, Xiaonan Shen, Yanlong Wang, and Ting Yu. *Chemically driven tunable light emission of charged and neutral excitons in monolayer WS2.* ACS nano, 8(11):11320–11329, 2014.

[79] Yifan Sun, Kazunori Fujisawa, Zhong Lin, Yu Lei, Jared S Mondschein, Mauricio Terrones, and Raymond E Schaak. *Low-temperature solution synthesis of transition metal dichalcogenide alloys with tunable optical properties.* Journal of the American Chemical Society, 139(32):11096–11105, 2017.

[80] Yipeng Zhao, Zhe Zhang, and Gang Ouyang. *Band shift of 2D transition-metal dichalcogenide alloys: size and composition effects.* Applied Physics A, 124(4):1–9, 2018.

[81] Chan Gao, Xiaoyong Yang, Ming Jiang, Lixin Chen, Zhiwen Chen, and Chandra Veer Singh. *Machine learning-enabled band gap prediction of monolayer transition metal chalcogenide alloys.* Physical Chemistry Chemical Physics, 24(7):4653–4665, 2022.

[82] Hannu-Pekka Komsa and Arkady V Krasheninnikov. *Two-dimensional transition metal dichalcogenide alloys: stability and electronic properties.* The journal of physical chemistry letters, 3(23):3652–3656, 2012.

[83] Jun Kang, Sefaattin Tongay, Jingbo Li, and Junqiao Wu. *Monolayer semiconducting transition metal dichalcogenide alloys: Stability and band bowing.* Journal of Applied Physics, 113(14):143703, 2013.

[84] LM Xie. *Two-dimensional transition metal dichalcogenide alloys: preparation, characterization and applications.* Nanoscale, 7(44):18392–18401, 2015.

[85] Rahul Sharma, Juhi Pandey, Krishna Rani Sahoo, Kewal Singh Rana, Ravi K Biroju, Wolfgang Theis, Ajay Soni, and Tharangattu N Narayanan. *Spectroscopic correlation of chalcogen defects in atomically thin* $MoS_{2(1-x)}Se_{2x}$ *alloys.* Journal of Physics: Materials, 3(4):045001, 2020.

[86] Qingliang Feng, Nannan Mao, Juanxia Wu, Hua Xu, Chunming Wang, Jin Zhang, and Liming Xie. *Growth of* $MoS_{2(1-x)}Se_{2x}$ *(x= 0.41-1.00) monolayer alloys with controlled morphology by physical vapor deposition.* ACS nano, 9(7):7450–7455, 2015.

[87] Ashkan Shahmanesh, Davide Romanin, Corentin Dabard, Sang-Soo Chee, Charlie Gréboval, Christophe Methivier, Mathieu G Silly, Julien Chaste, Matthieu Bugnet, Debora Pierucci, et al. *2D Monolayer of the 1T'Phase of Alloyed WSSe from Colloidal Synthesis.* The Journal of Physical Chemistry C, 125(20):11058–11065, 2021.

[88] Qixin Deng, Xiaobo Li, Huayan Si, Jinhua Hong, Shiyao Wang, Qingliang Feng, Chen-Xia Hu, Shanshan Wang, Hao-Li Zhang, Kazu Suenaga, et al. *Strong Band Bowing Effects and Distinctive Optoelectronic Properties of 2H and 1T́Phase-Tunable* $Mo_xRe_{1\text{-}x}S_2$ *Alloys.* Advanced Functional Materials, 30(34):2003264, 2020.

[89] Sandhya Susarla, Alex Kutana, Jordan A Hachtel, Vidya Kochat, Amey Apte, Robert Vajtai, Juan Carlos Idrobo, Boris I Yakobson, Chandra Sekhar Tiwary, and Pulickel M Ajayan. *Quaternary 2D transition metal dichalcogenides (TMDs) with tunable bandgap.* Advanced Materials, 29(35):1702457, 2017.

[90] Ji-Hui Yang and Boris I Yakobson. *Unusual negative formation enthalpies and atomic ordering in isovalent alloys of transition metal dichalcogenide monolayers.* Chemistry of Materials, 30(5):1547–1555, 2018.

[91] Qingliang Feng, Yiming Zhu, Jinhua Hong, Mei Zhang, Wenjie Duan, Nannan Mao, Juanxia Wu, Hua Xu, Fengliang Dong, Fang Lin, et al. *Growth of large-area 2D* $MoS_{2(1\text{-}x)}Se_{2x}$ *semiconductor alloys.* Advanced Materials, 26(17):2648–2653, 2014.

[92] Velveth Klee, Edwin Preciado, David Barroso, Ariana E Nguyen, Chris Lee, Kristopher J Erickson, Mark Triplett, Brandon Davis, I-Hsi Lu, Sarah Bobek, et al. *Superlinear composition-dependent photocurrent in CVD-grown monolayer* $MoS_{2(1\text{-}x)}Se_{2x}$ *alloy devices.* Nano letters, 15(4):2612–2619, 2015.

[93] Qiufang Gong, Liang Cheng, Changhai Liu, Mei Zhang, Qingliang Feng, Hualin Ye, Min Zeng, Liming Xie, Zhuang Liu, and Yanguang Li. *Ultrathin* $MoS_{2(1-x)}$ Se_{2x}*alloy nanoflakes for electrocatalytic hydrogen evolution reaction.* Acs Catalysis, 5(4):2213–2219, 2015.

[94] Yu Lei, Srimanta Pakhira, Kazunori Fujisawa, Xuyang Wang, Oluwagbenga Oare Iyiola, Néstor Perea López, Ana Laura Elías, Lakshmy Pulickal Rajukumar, Chanjing Zhou, Bernd Kabius, et al. *Low-temperature synthesis of heterostructures of transition metal dichalcogenide alloys ($W_xMo_{1\text{-}x}S_2$) and graphene with superior catalytic performance for hydrogen evolution.* ACS nano, 11(5):5103–5112, 2017.

[95] Yanfeng Chen, Jinyang Xi, Dumitru O Dumcenco, Zheng Liu, Kazu Suenaga, Dong Wang, Zhigang Shuai, Ying-Sheng Huang, and Liming Xie. *Tunable band gap photoluminescence from atomically thin transition-metal dichalcogenide alloys.* Acs Nano, 7(5):4610–4616, 2013.

[96] Quan Ma, Miguel Isarraraz, Chen S Wang, Edwin Preciado, Velveth Klee, Sarah Bobek, Koichi Yamaguchi, Emily Li, Patrick Michael Odenthal, Ariana Nguyen, et al. *Postgrowth tuning of the bandgap of single-layer molybdenum disulfide films by sulfur/selenium exchange.* Acs Nano, 8(5):4672–4677, 2014.

[97] Celso de Mello Donegá. *Synthesis and properties of colloidal heteronanocrystals.* Chemical Society Reviews, 40(3):1512–1546, 2011.

[98] Yunjeong Hwang and Naechul Shin. *Colloidal Synthesis of MoSe2/WSe2 Heterostructure Nanoflowers via Two-Step Growth.* Materials, 14(23):7294, 2021.

[99] Ruijie Zhang, Menghan Li, Lin Li, Zhongming Wei, Fei Jiao, Dechao Geng, and Wenping Hu. *The More, the Better–Recent Advances in Construction of 2D Multi-Heterostructures.* Advanced Functional Materials, 31(26):2102049, 2021.

[100] Hong Wang, Fucai Liu, Wei Fu, Zheyu Fang, Wu Zhou, and Zheng Liu. *Two-dimensional heterostructures: fabrication, characterization, and application.* Nanoscale, 6(21):12250–12272, 2014.

[101] Tao Chen, Degong Ding, Jia Shi, Guang Wang, Liangzhi Kou, Xiaoming Zheng, Xibiao Ren, Xinfeng Liu, Chuanhong Jin, Jianxin Zhong, et al. *Lateral and vertical MoSe2–MoS2 heterostructures via epitaxial growth: triggered by high-temperature annealing and precursor concentration.* The journal of physical chemistry letters, 10(17):5027–5035, 2019.

[102] Ting Zheng, Yu-Chuan Lin, Yiling Yu, Pavel Valencia-Acuna, Alexander A Puretzky, Riccardo Torsi, Chenze Liu, Ilia N Ivanov, Gerd Duscher, David B Geohegan, et al. *Excitonic dynamics in Janus MoSSe and WSSe monolayers.* Nano Letters, 21(2):931–937, 2021.

[103] Chaoliang Tan, Junze Chen, Xue-Jun Wu, and Hua Zhang. *Epitaxial growth of hybrid nanostructures.* Nature Reviews Materials, 3(2):1–13, 2018.

[104] Atsushi Koma. *Van der Waals epitaxy—a new epitaxial growth method for a highly lattice-mismatched system.* Thin Solid Films, 216(1):72–76, 1992.

[105] KS Novoselov, o A Mishchenko, o A Carvalho, and AH Castro Neto. *2D materials and van der Waals heterostructures.* Science, 353(6298):aac9439, 2016.

[106] Keiji Ueno, Koichiro Saiki, Toshihiro Shimada, and Atsushi Koma. *Epitaxial growth of transition metal dichalcogenides on cleaved faces of mica.* Journal of Vacuum Science & Technology A: Vacuum, Surfaces, and Films, 8(1):68–72, 1990.

[107] RL Anderson. *Germanium-gallium arsenide heterojunctions.* IBM Journal of Research and Development, 4(3):283–287, 1960.

[108] Ke Xu, Yuanfeng Xu, Hao Zhang, Bo Peng, Hezhu Shao, Gang Ni, Jing Li, Mingyuan Yao, Hongliang Lu, Heyuan Zhu, et al. *The role of Anderson's rule in determining electronic, optical and transport properties of transition metal dichalcogenide heterostructures.* Physical Chemistry Chemical Physics, 20(48):30351–30364, 2018.

[109] Matthew Z Bellus, Ming Li, Samuel D Lane, Frank Ceballos, Qiannan Cui, Xiao Cheng Zeng, and Hui Zhao. *Type-I van der Waals heterostructure formed by* MoS_2 *and* ReS_2 *monolayers.* Nanoscale horizons, 2(1):31–36, 2017.

[110] Marco Lattuada and T Alan Hatton. *Synthesis, properties and applications of Janus nanoparticles.* Nano Today, 6(3):286–308, 2011.

[111] Georg Daniel Förster, Magali Benoit, and Julien Lam. *Alloy, Janus and core–shell nanoparticles: numerical modeling of their*

nucleation and growth in physical synthesis. Physical Chemistry Chemical Physics, 21(41):22774–22781, 2019.

[112] Jing Zhang, Shuai Jia, Iskandar Kholmanov, Liang Dong, Dequan Er, Weibing Chen, Hua Guo, Zehua Jin, Vivek B Shenoy, Li Shi, et al. *Janus monolayer transition-metal dichalcogenides.* ACS nano, 11(8):8192–8198, 2017.

[113] Yujin Ji, Mingye Yang, Haiping Lin, Tingjun Hou, Lu Wang, Youyong Li, and Shuit-Tong Lee. *Janus structures of transition metal dichalcogenides as the heterojunction photocatalysts for water splitting.* The Journal of Physical Chemistry C, 122(5):3123–3129, 2018.

[114] Xiangchao Ma, Xin Wu, Haoda Wang, and Yucheng Wang. *A Janus MoSSe monolayer: a potential wide solar-spectrum water-splitting photocatalyst with a low carrier recombination rate.* Journal of Materials Chemistry A, 6(5):2295–2301, 2018.

[115] Liang Dong, Jun Lou, and Vivek B Shenoy. *Large in-plane and vertical piezoelectricity in Janus transition metal dichalchogenides.* ACS nano, 11(8):8242–8248, 2017.

[116] Paul C Uzoma, Huan Hu, Mahdi Khadem, and Oleksiy V Penkov. *Tribology of 2D nanomaterials: A review.* Coatings, 10(9):897, 2020.

[117] Bertold Rasche, Julius Brunner, Tim Schramm, Madhav Prasad Ghimire, Ulrike Nitzsche, Bernd Büchner, Romain Giraud, Manuel Richter, and Joseph Dufouleur. *Determination of Cleavage Energy and Efficient Nanostructuring of Layered Materials by Atomic Force Microscopy.* Nano Letters, 22(9):3550–3556, 2022.

[118] Morasae Samadi, Navid Sarikhani, Mohammad Zirak, Hua Zhang, Hao-Li Zhang, and Alireza Z. Moshfegh. *Group 6 transition metal dichalcogenide nanomaterials: synthesis, applications and future perspectives.* Nanoscale Horizons, 3(2):90–204, 2018.

[119] Wen Qian, Rui Hao, Yanglong Hou, Yuan Tian, Chengmin Shen, Hongjun Gao, and Xuelei Liang. *Solvothermal-assisted exfoliation process to produce graphene with high yield and high quality.* Nano Research, 2(9):706–712, 2009.

[120] C. Backes, B. M. Szydlowska, A. Harvey, S. Yuan, V. Vega-Mayoral, B. R. Davies, P. L. Zhao, D. Hanlon, E. J. Santos, M. I. Katsnelson, W. J. Blau, C. Gadermaier, and J. N. Coleman. *Production of Highly Monolayer Enriched Dispersions of Liquid-Exfoliated Nanosheets by Liquid Cascade Centrifugation.* ACS nano, 10(1):1589–601, 2016.

[121] Claudia Backes, Thomas M Higgins, Adam Kelly, Conor Boland, Andrew Harvey, Damien Hanlon, and Jonathan N Coleman. *Guidelines for exfoliation, characterization and processing of layered materials produced by liquid exfoliation.* Chemistry of materials, 29(1):243–255, 2017.

[122] C. Backes, R. J. Smith, N. McEvoy, N. C. Berner, D. McCloskey, H. C. Nerl, A. O'Neill, P. J. King, T. Higgins, D. Hanlon, N. Scheuschner, J. Maultzsch, L. Houben, G. S. Duesberg, J. F. Donegan, V. Nicolosi, and J. N. Coleman. *Edge and confinement effects allow in situ measurement of size and thickness of liquid-exfoliated nanosheets.* Nature communications, 5:4576, 2014.

[123] Joohoon Kang, Jung-Woo T Seo, Diego Alducin, Arturo Ponce, Miguel Jose Yacaman, and Mark C Hersam. *Thickness sorting of two-dimensional transition metal dichalcogenides via copolymer-assisted density gradient ultracentrifugation.* Nature communications, 5(1):1–7, 2014.

[124] Chih-Jen Shih, Shangchao Lin, Michael S Strano, and Daniel Blankschtein. *Understanding the stabilization of liquid-phase-exfoliated graphene in polar solvents: molecular dynamics simulations and kinetic theory of colloid aggregation.* Journal of the American Chemical Society, 132(41):14638–14648, 2010.

[125] Jonathan N Coleman. *Liquid exfoliation of defect-free graphene.* Accounts of chemical research, 46(1):14–22, 2013.

[126] Pieter Schiettecatte, Anastasia Rousaki, Peter Vandenabeele, Pieter Geiregat, and Zeger Hens. *Liquid-phase exfoliation of rhenium disulfide by solubility parameter matching.* Langmuir, 36(51):15493–15500, 2020.

[127] Jian Zhang, Tianyu Ji, Huihui Jin, Zhe Wang, Ming Zhao, Daping He, Guoqiang Luo, and Boyang Mao. *Mild Liquid-Phase*

Exfoliation of Transition Metal Dichalcogenide Nanosheets for Hydrogen Evolution. ACS Applied Nano Materials, 2022.

[128] E Benavente, MA Santa Ana, F Mendizábal, and G González. *Intercalation chemistry of molybdenum disulfide.* Coordination chemistry reviews, 224(1-2):87–109, 2002.

[129] Ekaterina D Grayfer, Mariia N Kozlova, and Vladimir E Fedorov. *Colloidal 2D nanosheets of MoS_2 and other transition metal dichalcogenides through liquid-phase exfoliation.* Advances in colloid and interface science, 245:40–61, 2017.

[130] GV Rao and MW Shafer. *Intercalation in layered transition metal dichalcogenides.* In Intercalated layered materials, pages 99–199. Springer, 1979.

[131] Per Joensen, RF Frindt, and S Roy Morrison. *Single-layer MoS_2* . Materials research bulletin, 21(4):457–461, 1986.

[132] G. Eda, H. Yamaguchi, D. Voiry, T. Fujita, M. Chen, and M. Chhowalla. *Photoluminescence from chemically exfoliated MoS_2*. Nano letters, 11(12):5111–6, 2011.

[133] Lei Tang, Junyang Tan, Huiyu Nong, Bilu Liu, and Hui-Ming Cheng. *Chemical vapor deposition growth of two-dimensional compound materials: controllability, material quality, and growth mechanism.* Accounts of Materials Research, 2(1):36–47, 2020.

[134] Xingli Wang, Yongji Gong, Gang Shi, Wai Leong Chow, Kunttal Keyshar, Gonglan Ye, Robert Vajtai, Jun Lou, Zheng Liu, Emilie Ringe, et al. *Chemical vapor deposition growth of crystalline monolayer $MoSe_2$* . ACS nano, 8(5):5125–5131, 2014.

[135] Yu-Chuan Lin, Wenjing Zhang, Jing-Kai Huang, Keng-Ku Liu, Yi-Hsien Lee, Chi-Te Liang, Chih-Wei Chu, and Lain-Jong Li. *Wafer-scale MoS_2 thin layers prepared by MoO_3 sulfurization.* Nanoscale, 4(20):6637–6641, 2012.

[136] Qingqing Ji, Yu Zhang, Yanfeng Zhang, and Zhongfan Liu. *Chemical vapour deposition of group-VIB metal dichalcogenide monolayers: engineered substrates from amorphous to single crystalline.* Chemical Society Reviews, 44(9):2587–2602, 2015.

[137] Shanshan Wang, Youmin Rong, Ye Fan, Mercè Pacios, Harish Bhaskaran, Kuang He, and Jamie H Warner. *Shape evolution*

of monolayer MoS_2 crystals grown by chemical vapor deposition. Chemistry of Materials, 26(22):6371–6379, 2014.

[138] Chunxiao Cong, Jingzhi Shang, Xing Wu, Bingchen Cao, Namphung Peimyoo, Caiyu Qiu, Litao Sun, and Ting Yu. *Synthesis and optical properties of large-area single-crystalline 2D semiconductor WS_2 monolayer from chemical vapor deposition.* Advanced Optical Materials, 2(2):131–136, 2014.

[139] Saifeng Zhang, Ningning Dong, Niall McEvoy, Maria O'Brien, Sinéad Winters, Nina C Berner, Chanyoung Yim, Yuanxin Li, Xiaoyan Zhang, Zhanghai Chen, et al. *Direct observation of degenerate two-photon absorption and its saturation in WS_2 and MoS_2 monolayer and few-layer films.* ACS nano, 9(7):7142–7150, 2015.

[140] Youngbin Lee, Jinhwan Lee, Hunyoung Bark, Il-Kwon Oh, Gyeong Hee Ryu, Zonghoon Lee, Hyungjun Kim, Jeong Ho Cho, Jong-Hyun Ahn, and Changgu Lee. *Synthesis of wafer-scale uniform molybdenum disulfide films with control over the layer number using a gas phase sulfur precursor.* Nanoscale, 6(5):2821–2826, 2014.

[141] Lee Kheng Tan, Bo Liu, Jing Hua Teng, Shifeng Guo, Hong Yee Low, and Kian Ping Loh. *Atomic layer deposition of a MoS_2 film.* Nanoscale, 6(18):10584–10588, 2014.

[142] Kibum Kang, Saien Xie, Lujie Huang, Yimo Han, Pinshane Y Huang, Kin Fai Mak, Cheol-Joo Kim, David Muller, and Jiwoong Park. *High-mobility three-atom-thick semiconducting films with wafer-scale homogeneity.* Nature, 520(7549):656–660, 2015.

[143] Javad Shamsi, Alexander S Urban, Muhammad Imran, Luca De Trizio, and Liberato Manna. *Metal halide perovskite nanocrystals: synthesis, post-synthesis modifications, and their optical properties.* Chemical reviews, 119(5):3296–3348, 2019.

[144] Daniel Franke, Daniel K Harris, Ou Chen, Oliver T Bruns, Jessica A Carr, Mark WB Wilson, and Moungi G Bawendi. *Continuous injection synthesis of indium arsenide quantum dots emissive in the short-wavelength infrared.* Nature communications, 7(1):1–9, 2016.

[145] Victor K LaMer and Robert H Dinegar. *Theory, production and mechanism of formation of monodispersed hydrosols.* Journal of the american chemical society, 72(11):4847–4854, 1950.

[146] Alessio Di Giacomo, Carmelita Rodá, Ali Hossain Khan, and Iwan Moreels. *Colloidal synthesis of laterally confined blue-emitting 3.5 monolayer CdSe nanoplatelets.* Chemistry of Materials, 32(21):9260–9267, 2020.

[147] Xiaogang Peng, Liberato Manna, Weidong Yang, Juanita Wickham, Erik Scher, Andreas Kadavanich, and A Paul Alivisatos. *Shape control of CdSe nanocrystals.* Nature, 404(6773):59–61, 2000.

[148] Anne C Berends and Celso de Mello Donega. *Ultrathin one-and two-dimensional colloidal semiconductor nanocrystals: Pushing quantum confinement to the limit.* The journal of physical chemistry letters, 8(17):4077–4090, 2017.

[149] Sandrine Ithurria and Benoit Dubertret. *Quasi 2D colloidal CdSe platelets with thicknesses controlled at the atomic level.* Journal of the American Chemical Society, 130(49):16504–16505, 2008.

[150] Jin Joo, Jae Sung Son, Soon Gu Kwon, Jung Ho Yu, and Taeghwan Hyeon. *Low-temperature solution-phase synthesis of quantum well structured CdSe nanoribbons.* Journal of the American Chemical Society, 128(17):5632–5633, 2006.

[151] Arelo O A Tanoh, Jack Alexander-Webber, James Xiao, Géraud Delport, Cyan A Williams, Hope Bretscher, Nicolas Gauriot, Jesse Allardice, Raj Pandya, Ye Fan, et al. *Enhancing photoluminescence and mobilities in WS2 monolayers with oleic acid ligands.* Nano Letters, 19(9):6299–6307, 2019.

[152] Sean A Fischer, Angela M Crotty, Svetlana V Kilina, Sergei A Ivanov, and Sergei Tretiak. *Passivating ligand and solvent contributions to the electronic properties of semiconductor nanocrystals.* Nanoscale, 4(3):904–914, 2012.

[153] Zhijun Ning, Matyas Molnár, Yun Chen, Peter Friberg, Liming Gan, Hans Ågren, and Ying Fu. *Role of surface ligands in optical properties of colloidal CdSe/CdS quantum dots.* Physical Chemistry Chemical Physics, 13(13):5848–5854, 2011.

[154] Michal Soreni-Harari, Nir Yaacobi-Gross, Dov Steiner, Assaf Aharoni, Uri Banin, Oded Millo, and Nir Tessler. *Tuning energetic levels in nanocrystal quantum dots through surface manipulations.* Nano letters, 8(2):678–684, 2008.

[155] Supriya Saha, Sunandan Sarkar, Sougata Pal, and Pranab Sarkar. *Ligand mediated tuning of the electronic energy levels of ZnO nanoparticles.* RSC advances, 3(2):532–539, 2013.

[156] Nuri Yazdani, Deniz Bozyigit, Kantawong Vuttivorakulchai, Mathieu Luisier, Ivan Infante, and Vanessa Wood. *Tuning electron–phonon interactions in nanocrystals through surface termination.* Nano letters, 18(4):2233–2242, 2018.

[157] Pieter Schiettecatte, Pieter Geiregat, and Zeger Hens. *Ultrafast carrier dynamics in few-layer colloidal molybdenum disulfide probed by broadband transient absorption spectroscopy.* The Journal of Physical Chemistry C, 123(16):10571–10577, 2019.

[158] M. Zhou, Z. Zhang, K. Huang, Z. Shi, R. Xie, and W. Yang. *Colloidal preparation and electrocatalytic hydrogen production of* MoS_2 *and* WS_2 *nanosheets with controllable lateral sizes and layer numbers.* Nanoscale, 8(33):15262–72, 2016.

[159] Rosanna Mastria, Riccardo Scarfiello, Davide Altamura, Cinzia Giannini, Andrea Liscio, Alessandro Kovtun, Giuseppe Valerio Bianco, Giovanni Bruno, Vincenzo Grillo, Amir H Tavabi, et al. *In-plane aligned colloidal 2D WS2 nanoflakes for solution-processable thin films with high planar conductivity.* Scientific reports, 9(1):1–13, 2019.

[160] Y. Pang, M. N. Uddin, W. Chen, S. Javaid, E. Barker, Y. Li, A. Suvorova, M. Saunders, Z. Yin, and G. Jia. *Colloidal Single-Layer Photocatalysts for Methanol-Storable Solar H2 Fuel.* Advanced materials (Deerfield Beach, Fla.), 31(49):e1905540, 2019.

[161] Zhengqing Liu, Na Li, Hongyang Zhao, and Yaping Du. *Colloidally synthesized MoSe2/graphene hybrid nanostructures as efficient electrocatalysts for hydrogen evolution.* Journal of Materials Chemistry A, 3(39):19706–19710, 2015.

[162] Jordan W Thomson, Kaz Nagashima, Peter M Macdonald, and Geoffrey A Ozin. *From sulfur- amine solutions to metal sulfide nanocrystals: peering into the oleylamine- sulfur black box.*

Journal of the American Chemical Society, 133(13):5036–5041, 2011.

[163] Xu Li, Aiwei Tang, Jiantao Li, Li Guan, Guoyi Dong, and Feng Teng. *Heating-up synthesis of MoS2 nanosheets and their electrical bistability performance.* Nanoscale research letters, 11(1):1–7, 2016.

[164] Miao Zhou, Zhuolei Zhang, Keke Huang, Zhan Shi, Renguo Xie, and Wensheng Yang. *Colloidal preparation and electrocatalytic hydrogen production of MoS_2 and WS_2 nanosheets with controllable lateral sizes and layer numbers.* Nanoscale, 8(33):15262–15272, 2016.

[165] W. Jung, S. Lee, D. Yoo, S. Jeong, P. Miro, A. Kuc, T. Heine, and J. Cheon. *Colloidal synthesis of single-layer MSe2 (M = Mo, W) nanosheets via anisotropic solution-phase growth approach.* Journal of the American Chemical Society, 137(23):7266–9, 2015.

[166] H. Jin, M. Ahn, S. Jeong, J. H. Han, D. Yoo, D. H. Son, and J. Cheon. *Colloidal Single-Layer Quantum Dots with Lateral Confinement Effects on 2D Exciton.* Journal of the American Chemical Society, 138(40):13253–13259, 2016.

[167] Dongwon Yoo, Minkyoung Kim, Sohee Jeong, Jeonghee Han, and Jinwoo Cheon. *Chemical synthetic strategy for single-layer transition-metal chalcogenides.* Journal of the American Chemical Society, 136(42):14670–14673, 2014.

[168] Xuanyu Cao, Caiping Ding, Cuiling Zhang, Wei Gu, Yinghan Yan, Xinhao Shi, and Yuezhong Xian. *Transition metal dichalcogenide quantum dots: synthesis, photoluminescence and biological applications.* Journal of Materials Chemistry B, 6(48):8011–8036, 2018.

[169] Junfeng Xie, Jiajia Zhang, Shuang Li, Fabian Grote, Xiaodong Zhang, Hao Zhang, Ruoxing Wang, Yong Lei, Bicai Pan, and Yi Xie. *Controllable disorder engineering in oxygen-incorporated MoS2 ultrathin nanosheets for efficient hydrogen evolution.* Journal of the American Chemical Society, 135(47):17881–17888, 2013.

[170] Zakhele Ndala, Ndivhuwo Shumbula, Siyabonga Nkabinde, Tshwarela Kolokoto, Obakeng Nchoe, Poslet Shumbula,

Zikhona N Tetana, Ella C Linganiso, Siziwe S Gqoba, and Nosipho Moloto. *Evaluating the effect of varying the metal precursor in the colloidal synthesis of MoSe2 nanomaterials and their application as electrodes in the hydrogen evolution reaction.* Nanomaterials, 10(9):1786, 2020.

[171] Saghar Setayeshgar, Masoud Karimipour, Mehdi Molaei, Masoud Rohani Moghadam, and Sepideh Khazraei. *Synthesis of scalable 1T/2H–MoSe2 nanosheets with a new source of Se in basic media and study of their HER activity.* International Journal of Hydrogen Energy, 45(11):6090–6101, 2020.

[172] Chi Zhang, Xing Chen, Zhiwei Peng, Xiaoming Fu, Linyuan Lian, Wei Luo, Jianbing Zhang, Honglang Li, YuHuang Wang, and Daoli Zhang. *Phosphine-free synthesis and shape evolution of MoSe 2 nanoflowers for electrocatalytic hydrogen evolution reactions.* CrystEngComm, 20(18):2491–2498, 2018.

[173] Xiaoli Zhou, Jun Jiang, Tao Ding, Jiajia Zhang, Bicai Pan, Jian Zuo, and Qing Yang. *Fast colloidal synthesis of scalable Mo-rich hierarchical ultrathin* $MoSe_{2\text{-}x}$ *nanosheets for high-performance hydrogen evolution.* Nanoscale, 6(19):11046–11051, 2014.

[174] Aleksandar Jankovic, Gaurav Chaudhary, and Francesco Goia. *Designing the design of experiments (DOE)–An investigation on the influence of different factorial designs on the characterization of complex systems.* Energy and Buildings, 250:111298, 2021.

[175] R. A Fisher. *The design of experiments.* Hafner Press, New York,, 1935.

[176] D.J. Finney. *The fractional replication of factorial arrangements.* Annals of Eugenics, 12(1):291–301, 1943.

[177] Robin L Plackett and J Peter Burman. *The design of optimum multifactorial experiments.* Biometrika, 33(4):305–325, 1946.

[178] Anthony Curtis Atkinson and Alexander N Donev. *Optimum experimental designs*, volume 5. Clarendon Press, 1992.

[179] Bradley Jones and Christopher J Nachtsheim. *A class of three-level designs for definitive screening in the presence of second-order effects.* Journal of Quality Technology, 43(1):1–15, 2011.

[180] Catarina P Santos, Tiago J Rato, and Marco S Reis. *Design of Experiments: A comparison study from the non-expert user's perspective.* Journal of Chemometrics, 33(1):e3087, 2019.

[181] Emily M Williamson, Zhaohong Sun, Lucía Mora-Tamez, and Richard L Brutchey. *Design of Experiments for Nanocrystal Syntheses: A How-To Guide for Proper Implementation.* Chemistry of Materials, 2022.

[182] Chang-Yun Lin and Po Yang. *Response surface methodology using split-plot definitive screening designs.* Journal of Quality Technology, 47(4):351–362, 2015.

[183] J. Gilman, L. Walls, L. Bandiera, and F. Menolascina. *Statistical Design of Experiments for Synthetic Biology.* ACS synthetic biology, 10(1):1–18, 2021.

[184] PJ Zomer, MHD Guimarães, JC Brant, N Tombros, and BJ Van Wees. *Fast pick up technique for high quality heterostructures of bilayer graphene and hexagonal boron nitride.* Applied Physics Letters, 105(1):013101, 2014.

[185] Y. Guo, D. Sun, B. Ouyang, A. Raja, J. Song, T. F. Heinz, and L. E. Brus. *Probing the Dynamics of the Metallic-to-Semiconducting Structural Phase Transformation in* MoS_2 *Crystals.* Nano letters, 15(8):5081–8, 2015.

[186] S. S. Chou, Y. K. Huang, J. Kim, B. Kaehr, B. M. Foley, P. Lu, C. Dykstra, P. E. Hopkins, C. J. Brinker, J. Huang, and V. P. Dravid. *Controlling the metal to semiconductor transition of* MoS_2 *and WS2 in solution.* Journal of the American Chemical Society, 137(5):1742–5, 2015.

[187] X. Guo, Y. Hou, R. Ren, and J. Chen. *Temperature-dependent Crystallization of* MoS_2 *Nanoflakes on Graphene Nanosheets for Electrocatalysis.* Nanoscale research letters, 12(1):479, 2017.

[188] M. A. Boles, D. Ling, T. Hyeon, and D. V. Talapin. *The surface science of nanocrystals.* Nature materials, 15(3):364, 2016.

[189] Subramaniam Jayabal, Jian Wu, Jiaye Chen, Dongsheng Geng, and Xiangbo Meng. *Metallic 1T-*MoS_2 *nanosheets and their composite materials: Preparation, properties and emerging applications.* Materials Today Energy, 10:264–279, 2018.

[190] Wencan Jin, Po-Chun Yeh, Nader Zaki, Datong Zhang, Jerzy T Sadowski, Abdullah Al-Mahboob, Arend M van Der Zande, Daniel A Chenet, Jerry I Dadap, Irving P Herman, et al. *Direct measurement of the thickness-dependent electronic band structure of MoS 2 using angle-resolved photoemission spectroscopy.* Physical review letters, 111(10):106801, 2013.

[191] Arlene O'Neill, Umar Khan, and Jonathan N Coleman. *Preparation of high concentration dispersions of exfoliated* MoS_2 *with increased flake size.* Chemistry of Materials, 24(12):2414–2421, 2012.

[192] Ali Jawaid, Dhriti Nepal, Kyoungweon Park, Michael Jespersen, Anthony Qualley, Peter Mirau, Lawrence F. Drummy, and Richard A. Vaia. *Mechanism for Liquid Phase Exfoliation of* MoS_2. Chemistry of Materials, 28(1):337–348, 2015.

[193] Lucia Muscuso, Sara Cravanzola, Federico Cesano, Domenica Scarano, and Adriano Zecchina. *Optical, Vibrational, and Structural Properties of* MoS_2*Nanoparticles Obtained by Exfoliation and Fragmentation via Ultrasound Cavitation in Isopropyl Alcohol.* The Journal of Physical Chemistry C, 119(7):3791–3801, 2015.

[194] C. Lee, H. Yan, L. E. Brus, T. F. Heinz, J. Hone, and S. Ryu. *Anomalous lattice vibrations of single- and few-layer* MoS_2. ACS nano, 4(5):2695–700, 2010.

[195] Satyaprakash Sahoo, Anand P. S. Gaur, Majid Ahmadi, Maxime J. F. Guinel, and Ram S. Katiyar. *Temperature-Dependent Raman Studies and Thermal Conductivity of Few-Layer* MoS_2. The Journal of Physical Chemistry C, 117(17):9042–9047, 2013.

[196] Sandro Mignuzzi, Andrew J. Pollard, Nicola Bonini, Barry Brennan, Ian S. Gilmore, Marcos A. Pimenta, David Richards, and Debdulal Roy. *Effect of disorder on Raman scattering of single-layer*MoS_2. Physical Review B, 91(19), 2015.

[197] Martin Dieterle, Gisela Weinberg, and Gerhard Mestl. *Raman spectroscopy of molybdenum oxides Part I. Structural characterization of oxygen defects in MoO 3- x by DR UV/VIS, Raman spectroscopy and X-ray diffraction.* Physical Chemistry Chemical Physics, 4(5):812–821, 2002.

[198] Hong Li, Qing Zhang, Chin Chong Ray Yap, Beng Kang Tay, Teo Hang Tong Edwin, Aurelien Olivier, and Dominique Baillargeat. *From Bulk to Monolayer* MoS_2*: Evolution of Raman Scattering.* Advanced Functional Materials, 22(7):1385–1390, 2012.

[199] J. Jeon, S. K. Jang, S. M. Jeon, G. Yoo, Y. H. Jang, J. H. Park, and S. Lee. *Layer-controlled CVD growth of large-area two-dimensional* MoS_2 *films.* Nanoscale, 7(5):1688–95, 2015.

[200] Ayberk Özden, Hüseyin Şar, Aydan Yeltik, Büşra Madenoğlu, Cem Sevik, Feridun Ay, and Nihan Kosku Perkgöz. *CVD grown 2D* MoS_2 *layers: A photoluminescence and fluorescence lifetime imaging study.* physica status solidi (RRL)–Rapid Research Letters, 10(11):792–796, 2016.

[201] K. P. Dhakal, D. L. Duong, J. Lee, H. Nam, M. Kim, M. Kan, Y. H. Lee, and J. Kim. *Confocal absorption spectral imaging of* MoS_2*: optical transitions depending on the atomic thickness of intrinsic and chemically doped* MoS_2. Nanoscale, 6(21):13028–35, 2014.

[202] R. Ganatra and Q. Zhang. *Few-layer* MoS_2*: a promising layered semiconductor.* ACS nano, 8(5):4074–99, 2014.

[203] X. Lu, M. I. Utama, J. Lin, X. Gong, J. Zhang, Y. Zhao, S. T. Pantelides, J. Wang, Z. Dong, Z. Liu, W. Zhou, and Q. Xiong. *Large-area synthesis of monolayer and few-layer MoSe2 films on SiO2 substrates.* Nano letters, 14(5):2419–25, 2014.

[204] Yu Zhao, Hyunjea Lee, Woong Choi, Weidong Fei, and Cheol Jin Lee. *Large-area synthesis of monolayer MoSe2 films on SiO2/Si substrates by atmospheric pressure chemical vapor deposition.* RSC Advances, 7(45):27969–27973, 2017.

[205] S. Tongay, J. Zhou, C. Ataca, K. Lo, T. S. Matthews, J. Li, J. C. Grossman, and J. Wu. *Thermally driven crossover from indirect toward direct bandgap in 2D semiconductors: MoSe2 versus* MoS_2. Nano letters, 12(11):5576–80, 2012.

[206] Guoan Tai, Tian Zeng, Jin Yu, Jianxin Zhou, Yuncheng You, Xufeng Wang, Hongrong Wu, Xu Sun, Tingsong Hu, and Wanlin Guo. *Fast and large-area growth of uniform* MoS_2 *monolayers on molybdenum foils.* Nanoscale, 8(4):2234–2241, 2016.

[207] M. J. Park, S. Gravelsins, J. Son, A. M. van der Zande, and A. A. Dhirani. *A Scalable, Solution-Based Approach to Tuning the Solubility and Improving the Photoluminescence of Chemically Exfoliated* MoS_2. ACS nano, 13(6):6469–6476, 2019.

[208] André Philipp Frauendorf, André Niebur, Lena Harms, Shivangi Shree, Bernhard Urbaszek, Michael Oestreich, Jens Hübner, and Jannika Lauth. *Room Temperature Micro-Photoluminescence Studies of Colloidal WS2 Nanosheets.* The Journal of Physical Chemistry C, 125(34):18841–18848, 2021.

[209] Rosanna Mastria, Anna Loiudice, Jan Vávra, Concetta Nobile, Riccardo Scarfiello, P. Davide Cozzoli, Alessandro Kovtun, Andrea Liscio, Nicola Sestu, Daniela Marongiu, Francesco Quochi, Raffaella Buonsanti, Michele Saba, Arrigo Calzolari, and Aurora Rizzo. *Photoluminescence emission induced by localized states in halide-passivated colloidal two-dimensional WS2 nanoflakes.* Journal of Materials Chemistry C, 9(7):2398–2407, 2021.

[210] S. Mukherjee, R. Maiti, A. K. Katiyar, S. Das, and S. K. Ray. *Novel Colloidal* MoS_2 *Quantum Dot Heterojunctions on Silicon Platforms for Multifunctional Optoelectronic Devices.* Scientific reports, 6:29016, 2016.

[211] H. Jin, B. Baek, D. Kim, F. Wu, J. D. Batteas, J. Cheon, and D. H. Son. *Effects of Direct Solvent-Quantum Dot Interaction on the Optical Properties of Colloidal Monolayer WS2 Quantum Dots.* Nano letters, 17(12):7471–7477, 2017.

[212] F. Cadiz, E. Courtade, C. Robert, G. Wang, Y. Shen, H. Cai, T. Taniguchi, K. Watanabe, H. Carrere, D. Lagarde, M. Manca, T. Amand, P. Renucci, S. Tongay, X. Marie, and B. Urbaszek. *Excitonic Linewidth Approaching the Homogeneous Limit in* MoS_2*-Based van der Waals Heterostructures.* Physical Review X, 7(2), 2017.

[213] J. Wierzbowski, J. Klein, F. Sigger, C. Straubinger, M. Kremser, T. Taniguchi, K. Watanabe, U. Wurstbauer, A. W. Holleitner, M. Kaniber, K. Muller, and J. J. Finley. *Direct exciton emission from atomically thin transition metal dichalcogenide heterostructures near the lifetime limit.* Scientific reports, 7(1):12383, 2017.

[214] X. Cui, G. H. Lee, Y. D. Kim, G. Arefe, P. Y. Huang, C. H. Lee, D. A. Chenet, X. Zhang, L. Wang, F. Ye, F. Pizzocchero, B. S. Jessen, K. Watanabe, T. Taniguchi, D. A. Muller, T. Low, P. Kim, and J. Hone. *Multi-terminal transport measurements of* MoS_2 *using a van der Waals heterostructure device platform.* Nature nanotechnology, 10(6):534–40, 2015.

[215] Sajith Vandana, Vidya Kochat, Jonghoon Lee, Vikas Varshney, Sadegh Yazdi, Jianfeng Shen, Suppanat Kosolwattana, Soumya Vinod, Robert Vajtai, Ajit K. Roy, Chandra Sekhar Tiwary, and P. M. Ajayan. *2D Heterostructure coatings ofhBN-*MoS_2*layers for corrosion resistance.* Journal of Physics D: Applied Physics, 50(4), 2017.

[216] Ashish Arora, Nils Kolja Wessling, Thorsten Deilmann, Till Reichenauer, Paul Steeger, Piotr Kossacki, Marek Potemski, Steffen Michaelis de Vasconcellos, Michael Rohlfing, and Rudolf Bratschitsch. *Dark trions govern the temperature-dependent optical absorption and emission of doped atomically thin semiconductors.* Physical Review B, 101(24), 2020.

[217] K. P. O'Donnell and X. Chen. *Temperature dependence of semiconductor band gaps.* Applied Physics Letters, 58(25):2924–2926, 1991.

[218] J. Pei, J. Yang, R. Xu, Y. H. Zeng, Y. W. Myint, S. Zhang, J. C. Zheng, Q. Qin, X. Wang, W. Jiang, and Y. Lu. *Exciton and Trion Dynamics in Bilayer* MoS_2. Small (Weinheim an der Bergstrasse, Germany), 11(48):6384–90, 2015.

[219] A. Arora, K. Nogajewski, M. Molas, M. Koperski, and M. Potemski. *Exciton band structure in layered MoSe2: from a monolayer to the bulk limit.* Nanoscale, 7(48):20769–75, 2015.

[220] Tsung-Shine Ko, Cheng-Ching Huang, and Der-Yuh Lin. *Optical and Transport Properties of Ni-*MoS_2. Applied Sciences, 6(8), 2016.

[221] J. W. Christopher, B. B. Goldberg, and A. K. Swan. *Long tailed trions in monolayer* MoS_2*: Temperature dependent asymmetry and resulting red-shift of trion photoluminescence spectra.* Scientific reports, 7(1):14062, 2017.

[222] Benoit Mahler, Veronika Hoepfner, Kristine Liao, and Geoffrey A Ozin. *Colloidal synthesis of 1T-*WS_2 *and 2H-*WS_2

nanosheets: applications for photocatalytic hydrogen evolution. Journal of the American Chemical Society, 136(40):14121–14127, 2014.

[223] Guohua Wei, David A Czaplewski, Erik J Lenferink, Teodor K Stanev, Il Woong Jung, and Nathaniel P Stern. *Size-tunable lateral confinement in monolayer semiconductors.* Scientific reports, 7(1):1–8, 2017.

[224] Sergii Golovynskyi, Matteo Bosi, Luca Seravalli, and Baikui Li. *MoS2 two-dimensional quantum dots with weak lateral quantum confinement: Intense exciton and trion photoluminescence.* Surfaces and Interfaces, 23:100909, 2021.

[225] Hong Li, Qing Zhang, Chin Chong Ray Yap, Beng Kang Tay, Teo Hang Tong Edwin, Aurelien Olivier, and Dominique Baillargeat. *From bulk to monolayer MoS2: evolution of Raman scattering.* Advanced Functional Materials, 22(7):1385–1390, 2012.

[226] Hyun Dong Ha, Dong Ju Han, Jong Seob Choi, Minsu Park, and Tae Seok Seo. *Dual role of blue luminescent MoS2 quantum dots in fluorescence resonance energy transfer phenomenon.* Small, 10(19):3858–3862, 2014.

[227] Haifeng Dong, Songsong Tang, Yansong Hao, Haizhu Yu, Wenhao Dai, Guifeng Zhao, Yu Cao, Huiting Lu, Xueji Zhang, and Huangxian Ju. *Fluorescent MoS2 quantum dots: ultrasonic preparation, up-conversion and down-conversion bioimaging, and photodynamic therapy.* ACS applied materials & interfaces, 8(5):3107–3114, 2016.

[228] Fabian Cadiz, Simon Tricard, Maxime Gay, Delphine Lagarde, Gang Wang, Cedric Robert, Pierre Renucci, Bernhard Urbaszek, and Xavier Marie. *Well separated trion and neutral excitons on superacid treated MoS2 monolayers.* Applied Physics Letters, 108(25):251106, 2016.

[229] V Huard, RT Cox, K Saminadayar, A Arnoult, and S Tatarenko. *Bound states in optical absorption of semiconductor quantum wells containing a two-dimensional electron gas.* Physical review letters, 84(1):187, 2000.

[230] Kin Fai Mak, Keliang He, Changgu Lee, Gwan Hyoung Lee, James Hone, Tony F Heinz, and Jie Shan. *Tightly bound trions in monolayer MoS2.* Nature materials, 12(3):207–211, 2013.

[231] A Thilagam. *Two-dimensional charged-exciton complexes.* Physical Review B, 55(12):7804, 1997.

[232] Ashish Arora, Nils Kolja Wessling, Thorsten Deilmann, Till Reichenauer, Paul Steeger, Piotr Kossacki, Marek Potemski, Steffen Michaelis de Vasconcellos, Michael Rohlfing, and Rudolf Bratschitsch. *Dark trions govern the temperature-dependent optical absorption and emission of doped atomically thin semiconductors.* Physical Review B, 101(24):241413, 2020.

[233] Gabriele Pippia, Diem Van Hamme, Beatriz Martín-García, Mirko Prato, and Iwan Moreels. *A colloidal route to semiconducting tungsten disulfide nanosheets with monolayer thickness.* Nanoscale, 14(42):15859–15868, 2022.

[234] Ilkka Kylänpää and Hannu-Pekka Komsa. *Binding energies of exciton complexes in transition metal dichalcogenide monolayers and effect of dielectric environment.* Physical Review B, 92(20):205418, 2015.

[235] Alexey Chernikov, Claudia Ruppert, Heather M Hill, Albert F Rigosi, and Tony F Heinz. *Population inversion and giant bandgap renormalization in atomically thin* WS_2 *layers.* Nature Photonics, 9(7):466–470, 2015.

[236] Frederik Lohof, Alexander Steinhoff, M Florian, M Lorke, Daniel Erben, Frank Jahnke, and Christopher Gies. *Prospects and limitations of transition metal dichalcogenide laser gain materials.* Nano letters, 19(1):210–217, 2018.

[237] Wenxu Zhang, Zhishuo Huang, Wanli Zhang, and Yanrong Li. *Two-dimensional semiconductors with possible high room temperature mobility.* Nano Research, 7(12):1731–1737, 2014.

[238] Dimitri D Vaughn, Romesh J Patel, Michael A Hickner, and Raymond E Schaak. *Single-crystal colloidal nanosheets of GeS and GeSe.* Journal of the American Chemical Society, 132(43):15170–15172, 2010.

[239] Pengshang Zhou, Gearoid Collins, Zeger Hens, Kevin M Ryan, Hugh Geaney, and Shalini Singh. *Colloidal WSe2 nanocrystals*

as anodes for lithium-ion batteries. Nanoscale, 12(43):22307–22316, 2020.

[240] Pengshang Zhou, Pieter Schiettecatte, Matthias Vandichel, Anastasia Rousaki, Peter Vandenabeele, Zeger Hens, and Shalini Singh. *Synthesis of colloidal WSe2 nanocrystals: polymorphism control by precursor-ligand chemistry.* Crystal Growth & Design, 21(3):1451–1460, 2021.

[241] Jessica Q Geisenhoff, Ashley K Tamura, and Alina M Schimpf. *Using ligands to control reactivity, size and phase in the colloidal synthesis of WSe 2 nanocrystals.* Chemical Communications, 55(60):8856–8859, 2019.

[242] Zhaoqiang Zheng, Tanmei Zhang, Jiandomg Yao, Yi Zhang, Jiarui Xu, and Guowei Yang. *Flexible, transparent and ultra-broadband photodetector based on large-area WSe2 film for wearable devices.* Nanotechnology, 27(22):225501, 2016.

[243] Tania Roy, Mahmut Tosun, Mark Hettick, Geun Ho Ahn, Chenming Hu, and Ali Javey. *2D-2D tunneling field-effect transistors using WSe2/SnSe2 heterostructures.* Applied Physics Letters, 108(8):083111, 2016.

[244] S Thirumala, T Hung, Arnab Raha, Niharika Thakuria, K Cho, Vijay Raghunathan, Zhihong Chen, and S Gupta. *WSe 2 based valley-coupled-spintronic devices for low power non-volatile memories.* In 2019 Device Research Conference (DRC), pages 211–212. IEEE, 2019.

[245] Neal Fairley, Vincent Fernandez, Mireille Richard-Plouet, Catherine Guillot-Deudon, John Walton, Emily Smith, Delphine Flahaut, Mark Greiner, Mark Biesinger, Sven Tougaard, et al. *Systematic and collaborative approach to problem solving using X-ray photoelectron spectroscopy.* Applied Surface Science Advances, 5:100112, 2021.

[246] Xue Zhao, Xiao Ma, Jian Sun, Dehui Li, and Xiurong Yang. *Enhanced catalytic activities of surfactant-assisted exfoliated* WS_2 *nanodots for hydrogen evolution.* ACS nano, 10(2):2159–2166, 2016.

[247] Andrew A Neath and Joseph E Cavanaugh. *The Bayesian information criterion: background, derivation, and applica-*

tions. Wiley Interdisciplinary Reviews: Computational Statistics, 4(2):199–203, 2012.

[248] Clifford M Hurvich and Chih-Ling Tsai. *Regression and time series model selection in small samples.* Biometrika, 76(2):297–307, 1989.

[249] Pengshang Zhou, Ivo Tanghe, Pieter Schiettecatte, Dries Van Thourhout, Zeger Hens, and Pieter Geiregat. *Ultrafast carrier dynamics in colloidal WS_2 nanosheets obtained through a hot injection synthesis.* The Journal of chemical physics, 151(16):164701, 2019.

[250] Lin Wang, Wenyan Wang, Quan Wang, Xiaochun Chi, Zhihui Kang, Qiang Zhou, Lingyun Pan, Hanzhuang Zhang, and Yinghui Wang. *Study on photoelectric characteristics of monolayer WS_2 films.* RSC advances, 9(64):37195–37200, 2019.

[251] Adriano Ambrosi, Zdeněk Sofer, and Martin Pumera. *2H→ 1T phase transition and hydrogen evolution activity of MoS2, MoSe2, WS2 and WSe2 strongly depends on the MX2 composition.* Chemical Communications, 51(40):8450–8453, 2015.

[252] Jung-wook Seo, Young-wook Jun, Seung Jin Ko, and Jinwoo Cheon. *In situ one-pot synthesis of 1-dimensional transition metal oxide nanocrystals.* The Journal of Physical Chemistry B, 109(12):5389–5391, 2005.

[253] David G Castner, Kenneth Hinds, and David W Grainger. *X-ray photoelectron spectroscopy sulfur 2p study of organic thiol and disulfide binding interactions with gold surfaces.* Langmuir, 12(21):5083–5086, 1996.

[254] Farid Bensebaa, Yu Zhou, Yves Deslandes, Erik Kruus, and Tomas H Ellis. *XPS study of metal-sulfur bonds in metal-alkanethiolate materials.* Surface science, 405(1):L472–L476, 1998.

[255] Alexei Barinov, O Baris Malcioglu, Stefano Fabris, Tao Sun, Luca Gregoratti, Matteo Dalmiglio, and Maya Kiskinova. *Initial stages of oxidation on graphitic surfaces: photoemission study and density functional theory calculations.* The Journal of Physical Chemistry C, 113(21):9009–9013, 2009.

[256] Urvesh Patil and Nuala M Caffrey. *Composition dependence of the charge-driven phase transition in group-VI transition metal dichalcogenides.* Physical Review B, 100(7):075424, 2019.

[257] Riccardo Frisenda, Yue Niu, Patricia Gant, Aday J Molina-Mendoza, Robert Schmidt, Rudolf Bratschitsch, Jinxin Liu, Lei Fu, Dumitru Dumcenco, Andras Kis, et al. *Micro-reflectance and transmittance spectroscopy: a versatile and powerful tool to characterize 2D materials.* Journal of Physics D: Applied Physics, 50(7):074002, 2017.

[258] Weijie Zhao, Zohreh Ghorannevis, Kiran Kumar Amara, Jing Ren Pang, Minglin Toh, Xin Zhang, Christian Kloc, Ping Heng Tan, and Goki Eda. *Lattice dynamics in mono-and few-layer sheets of WS2 and WSe2.* Nanoscale, 5(20):9677–9683, 2013.

[259] Xin Luo, Yanyuan Zhao, Jun Zhang, Minglin Toh, Christian Kloc, Qihua Xiong, and Su Ying Quek. *Effects of lower symmetry and dimensionality on Raman spectra in two-dimensional WSe2.* Physical Review B, 88(19):195313, 2013.

[260] Philipp Tonndorf, Robert Schmidt, Philipp Böttger, Xiao Zhang, Janna Börner, Andreas Liebig, Manfred Albrecht, Christian Kloc, Ovidiu Gordan, Dietrich RT Zahn, et al. *Photoluminescence emission and Raman response of monolayer MoS2, MoSe2, and WSe2.* Optics express, 21(4):4908–4916, 2013.

[261] Rui Zhang, Daniel Drysdale, Vasileios Koutsos, and Rebecca Cheung. *Controlled layer thinning and p-type doping of WSe_2 by vapor XeF_2.* Advanced Functional Materials, 27(41):1702455, 2017.

[262] Maria S Sokolikova, Peter C Sherrell, Pawel Palczynski, Victoria L Bemmer, and Cecilia Mattevi. *Direct solution-phase synthesis of 1T' WSe2 nanosheets.* Nature communications, 10(1):1–8, 2019.

[263] Juanjuan Jia, Azzedine Bendounan, Harish Makri Nimbegondi Kotresh, Karine Chaouchi, Fausto Sirotti, Srinivasan Sampath, and Vladimir A Esaulov. *Selenium adsorption on Au (111) and Ag (111) surfaces: adsorbed selenium and selenide films.* The Journal of Physical Chemistry C, 117(19):9835–9842, 2013.

[264] Jahee Kim, Yi Rang Lim, Yeoheung Yoon, Wooseok Song, Bo Keun Park, Jongsun Lim, Taek-Mo Chung, and Chang Gyoun Kim. *A facile synthetic route to tungsten diselenide using a new precursor containing a long alkyl chain cation for multifunctional electronic and optoelectronic applications.* RSC advances, 9(11):6169–6176, 2019.

[265] Sheng Liu, Andrés Granados del Águila, Xue Liu, Yihan Zhu, Yu Han, Apoorva Chaturvedi, Pu Gong, Hongyi Yu, Hua Zhang, Wang Yao, et al. *Room-temperature valley polarization in atomically thin semiconductors via chalcogenide alloying.* ACS nano, 14(8):9873–9883, 2020.

[266] Jun Kang, Sefaattin Tongay, Jian Zhou, Jingbo Li, and Junqiao Wu. *Band offsets and heterostructures of two-dimensional semiconductors.* Applied Physics Letters, 102(1):012111, 2013.

[267] Hannu-Pekka Komsa and Arkady V Krasheninnikov. *Electronic structures and optical properties of realistic transition metal dichalcogenide heterostructures from first principles.* Physical Review B, 88(8):085318, 2013.

[268] Biao Wu, Haihong Zheng, Shaofei Li, Junnan Ding, Jun He, Zongwen Liu, and Yanping Liu. *Enhanced interlayer neutral excitons and trions in MoSe2/MoS2/MoSe2 trilayer heterostructure.* Nano Research, pages 1–6, 2022.

[269] Nan Zhang, Alessandro Surrente, Michał Baranowski, Duncan K Maude, Patricia Gant, Andres Castellanos-Gomez, and Paulina Plochocka. *Moiré intralayer excitons in a MoSe2/MoS2 heterostructure.* Nano letters, 18(12):7651–7657, 2018.

[270] Fang Li, Boyi Xu, Wen Yang, Zhaoyang Qi, Chao Ma, Yajuan Wang, Xuehong Zhang, Zhuoran Luo, Delang Liang, Dong Li, et al. *High-performance optoelectronic devices based on van der Waals vertical MoS2/MoSe2 heterostructures.* Nano Research, 13(4):1053–1059, 2020.

[271] Masoud Mahjouri-Samani, Ming-Wei Lin, Kai Wang, Andrew R Lupini, Jaekwang Lee, Leonardo Basile, Abdelaziz Boulesbaa, Christopher M Rouleau, Alexander A Puretzky, Ilia N Ivanov, et al. *Patterned arrays of lateral heterojunctions within monolayer two-dimensional semiconductors.* Nature communications, 6(1):1–6, 2015.

[272] Matthew Z Bellus, Masoud Mahjouri-Samani, Samuel D Lane, Akinola D Oyedele, Xufan Li, Alexander A Puretzky, David Geohegan, Kai Xiao, and Hui Zhao. *Photocarrier transfer across monolayer MoS2–MoSe2 lateral heterojunctions.* ACS nano, 12(7):7086–7092, 2018.

[273] Yating Yang, Wei-Hai Fang, and Run Long. *Disparity in photoexcitation dynamics between vertical and lateral MoS2/WSe2 heterojunctions: time-domain simulation emphasizes the importance of donor–acceptor interaction and band alignment.* The Journal of Physical Chemistry Letters, 8(23):5771–5778, 2017.

[274] Yuzheng Guo and John Robertson. *Band engineering in transition metal dichalcogenides: Stacked versus lateral heterostructures.* Applied Physics Letters, 108(23):233104, 2016.

[275] Bin Amin, Thaneshwor P Kaloni, Georg Schreckenbach, and Michael S Freund. *Materials properties of out-of-plane heterostructures of MoS2-WSe2 and WS2-MoSe2.* applied physics letters, 108(6):063105, 2016.

[276] Krzysztof Kośmider and Joaquın Fernández-Rossier. *Electronic properties of the MoS 2-WS 2 heterojunction.* Physical Review B, 87(7):075451, 2013.

[277] Frank Ceballos, Matthew Z Bellus, Hsin-Ying Chiu, and Hui Zhao. *Ultrafast charge separation and indirect exciton formation in a MoS2–MoSe2 van der Waals heterostructure.* ACS nano, 8(12):12717–12724, 2014.

[278] Michal Baranowski, Alessandro Surrente, L Klopotowski, JM Urban, Nan Zhang, Duncan K Maude, Kamil Wiwatowski, Sebastian Mackowski, Yen-Cheng Kung, Dumitru Dumcenco, et al. *Probing the interlayer exciton physics in a MoS2/MoSe2/MoS2 van der Waals heterostructure.* Nano letters, 17(10):6360–6365, 2017.

[279] Ming-Yang Li, Chang-Hsiao Chen, Yumeng Shi, and Lain-Jong Li. *Heterostructures based on two-dimensional layered materials and their potential applications.* Materials Today, 19(6):322–335, 2016.

[280] Yuze Meng, Tianmeng Wang, Zhipeng Li, Ying Qin, Zhen Lian, Yanwen Chen, Michael C Lucking, Kory Beach, Takashi Taniguchi, Kenji Watanabe, et al. *Excitonic complexes and*

emerging interlayer electron–phonon coupling in BN encapsulated monolayer semiconductor alloy: WS0. 6Se1. 4. Nano Letters, 19(1):299–307, 2018.

[281] Xidong Duan, Chen Wang, Zheng Fan, Guolin Hao, Liangzhi Kou, Udayabagya Halim, Honglai Li, Xueping Wu, Yicheng Wang, Jianhui Jiang, et al. *Synthesis of* $WS_{2x}Se_{2\text{-}2x}$ *alloy nanosheets with composition-tunable electronic properties.* Nano letters, 16(1):264–269, 2016.

[282] Qi Fu, Lei Yang, Wenhui Wang, Ali Han, Jian Huang, Pingwu Du, Zhiyong Fan, Jingyu Zhang, and Bin Xiang. *Synthesis and enhanced electrochemical catalytic performance of monolayer* $WS_{2(1\text{-}x)}Se_{2x}$ *with a tunable band gap.* Advanced Materials, 27(32):4732–4738, 2015.

[283] Albert F Rigosi, Heather M Hill, Yilei Li, Alexey Chernikov, and Tony F Heinz. *Probing interlayer interactions in transition metal dichalcogenide heterostructures by optical spectroscopy: MoS2/WS2 and MoSe2/WSe2.* Nano letters, 15(8):5033–5038, 2015.

[284] Nikolaus Flöry, Achint Jain, Palash Bharadwaj, Markus Parzefall, Takashi Taniguchi, Kenji Watanabe, and Lukas Novotny. *A WSe2/MoSe2 heterostructure photovoltaic device.* Applied Physics Letters, 107(12):123106, 2015.

[285] Zilong Wang, Patrick Altmann, Christoph Gadermaier, Yating Yang, Wei Li, Lavinia Ghirardini, Chiara Trovatello, Marco Finazzi, Lamberto Duò, Michele Celebrano, et al. *Phonon-mediated interlayer charge separation and recombination in a MoSe2/WSe2 heterostructure.* Nano Letters, 21(5):2165–2173, 2021.

[286] Merve Öper, Yahaya Shehu, and Nihan Kosku Perkgöz. *Temperature-dependent Raman modes of MoS2/MoSe2 van der Waals heterostructures.* Semiconductor Science and Technology, 35(11):115020, 2020.

[287] Qian Cai, Qiankun Ju, Wenting Hong, Chuanyong Jian, Taikun Wang, and Wei Liu. *Water assisted growth of two-dimensional MoS2/MoSe2 vertical heterostructures on molten glass.* Nanoscale, 14(5):1990–1996, 2022.

[288] Lingming Yang, Kausik Majumdar, Han Liu, Yuchen Du, Heng Wu, Michael Hatzistergos, PY Hung, Robert Tieckelmann, Wilman Tsai, Chris Hobbs, et al. *Chloride molecular doping technique on 2D materials: WS2 and MoS2.* Nano letters, 14(11):6275–6280, 2014.

[289] Jinok Kim, Keun Heo, Dong-Ho Kang, Changhwan Shin, Sungjoo Lee, Hyun-Yong Yu, and Jin-Hong Park. *Rhenium Diselenide (ReSe2) Near-Infrared Photodetector: Performance Enhancement by Selective p-Doping Technique.* Advanced Science, 6(21):1901255, 2019.

[290] Gayatri Swain, Sabiha Sultana, and Kulamani Parida. *A review on vertical and lateral heterostructures of semiconducting 2D-MoS2 with other 2D materials: A feasible perspective for energy conversion.* Nanoscale, 13(22):9908–9944, 2021.

English Summary
–Summary in English–

Transition metal dichalcogenides (TMDs) are a class of 2D materials characterized by a layered structure, where each single layer is formed by a transition metal plane sandwiched between two planes of chalcogen atoms. These single layers can stack on top of each other via Van der Waals interactions, with the stacking order determining the polytype: 1T, metallic or 2H, semiconducting. In the latter case, the number of layers determines the material properties: an odd-number of layers translates in broken inversion symmetry, while a reduction of layer number yields to an increase of band gap energy. Monolayer thickness is associated to a conversion of the band gap transition from indirect to direct, resulting in the emerging of photoluminescence. Colloidal synthesis is becoming, among chemical vapor deposition, liquid-phase and mechanical exfoliation one of the main techniques used in the production of TMDs, due to its flexibility, tunability, and low production cost.

We started in Chapter 2 with the optimization of the colloidal synthesis of MoS_2 nanosheets using the Design Of Experiment (DOE) approach, a statistical method used to investigate the correlation between the factors involved in a process and the outcome of the process itself, using a set of controlled experiments. The evaluation of the factors involved in the synthesis in correlation with the opto-electronic properties of MoS_2 nanosheets led to an optimized protocol used as starting point for the final protocol. Such protocol provided nanosheets with mono- and bilayer thickness, and exciton energy close to monolayer MoS_2 band gap energy. The extention of the protocol $MoSe_2$ yielded to nanosheets with monolayer thickness and exciton energy slightly blue shifted compared to monolayer $MoSe_2$ nanosheets reported in literature. Both materials displayed photoluminescent properties at cryogenic and room temperature, centred at 1.96 eV and 1.67 eV for MoS_2 and $MoSe_2$ nanosheets respectively and a FWHM (after hBN encapsulation) of 76 meV and 38.6 meV respectively.

The synthesis protocol of MoS_2 is refined In Chapter 3, to reduce the lateral size of the nanosheets. The reduction of the S:Mo ratio to 2 led to MoS_2 nanosheets having mono- and bilayer thickness, with lateral size of 11.45 nm ±4.89 nm and exciton energy close to earlier reported monolayer MoS_2. Photoluminescence spectroscopy reveals photoluminescence at 80 K, formed by trion and neutral exciton centred at 1.91 eV and 1.97 eV and with FWHM of 66 meV and 42 meV respectively, without any encapsulation.

These results justified the shift in topic from molybdenum-based TMDs to tungsten-based TMDs. Chapter 4 report the synthesis optimization of WSe_2 nanosheeets, using the results of the master student Diem Van Hamme on the optimization of WS_2 as starting point. The UV-Vis spectrum of the sample featured the A and B excitons with energy close to monolayer WSe_2 nanosheets and a monolayer thickness. XPS analysis on the nanosheets showed the presence of metallic polytype and oxide species, justifying the lack of photoluminescence from the sample.

The synthesis of molybdenum- and tungsten-based alloys, and $MoS_2/MoSe_2$ heterostructure is addressed in Chapter 5. The alloys synthesis is based on the corresponding sulfide protocols, adding elemental selenium as second chalcogen source. The resulting alloys, $MoS_xSe_{(2-x)}$ and $WS_xSe_{(2-x)}$ displayed in the UV-Vis absorption spectrum the typical two excitons, with energies in between the pristine selenide and sulfide monolayer samples. Raman spectroscopy revealed the presence of the characteristic A_{1g} splitting for $MoS_xSe_{(2-x)}$ alloy and the presence of both sulfide and selenide Raman modes for $WS_xSe_{(2-x)}$ alloy, confirming the alloyed nature of the sample. The $MoS_2/MoSe_2$ heterostructure is obtained combined the MoS_2 and $MoSe_2$ protocols in a two-step synthesis, firstly synthesizing $MoSe_2$ and then starting in the same reaction medium the MoS_2 synthesis. The so-obtained heterostructure is characterized by three different excitonic features in the UV-Vis absorption spectrum, associated to $MoSe_2$ and MoS_2 species. The Raman spectrum displayed by the sample si composed by the single modes associated to pristine $MoSe_2$ and MoS_2 nanosheets; with the clear absence of modes associated to alloyed material. The sample composition mapping, via EDS, revealed the presence of discrete regions in composition, supporting the assignation to an heterostructured sample.

Nederlandse Samenvatting
–Summary in Dutch–

Transitiemetaaldichalcogeniden (TMDs) zijn een klasse van 2D-materialen die gekenmerkt worden door een gelaagde structuur, waarbij elke enkele laag wordt gevormd door een transitiemetaalvlak tussen twee vlakken van chalcogenideatomen. Deze enkele lagen kunnen op elkaar stapelen via Van der Waals interacties, waarbij de stapelvolgorde het polytype bepaalt: 1T, metallisch of 2H, halfgeleidend. In het laatste geval bepaalt het aantal lagen de materiaaleigenschappen: een oneven aantal lagen vertaalt zich in een gebroken inversiesymmetrie, terwijl een vermindering van het aantal lagen leidt tot een toename van de bandkloofenergie. Monolaagdikte wordt geassocieerd met een omzetting van de bandkloofovergang van indirect naar direct, wat resulteert in het ontstaan van fotoluminescentie. Colloïdale synthese wordt, naast chemische dampdepositie, vloeibare fase en mechanische exfoliatie, één van de belangrijkste technieken voor de productie van TMD's, vanwege de flexibiliteit, de afstembaarheid en de lage productiekosten. In hoofdstuk 2 zijn we begonnen met de optimalisatie van de colloïdale synthese van nanoplaatjes met behulp van de Design Of Experiment (DOE) methode, een statistische methode die wordt gebruikt om de correlatie te onderzoeken tussen de factoren die een rol spelen in een proces en de uitkomst van het proces zelf, met behulp van een reeks gecontroleerde experimenten. De evaluatie van de factoren die betrokken zijn bij de synthese in correlatie met de opto-elektronische eigenschappen van nanoplaatjes leidde tot een geoptimaliseerd protocol gebruikt als uitgangspunt voor het uiteindelijke protocol. Dit protocol leverde nanoplaatjes op met een mono- en bilaagdikte, en een excitonenergie dicht bij de bandkloofenergie van monolaag MoS_2. De uitbreiding van het protocol leverde $MoSe_2$ nanoplaatjes

op met monolaag dikte en exciton energie enigszins verschoven naar het blauw ten opzichte van monolaag $MoSe_2$ nanoplaatjes beschreven in de literatuur. Beide materialen vertoonden fotoluminescente eigenschappen bij cryogene- en kamertemperatuur, gecentreerd bij 1.96 eV en 1.67 eV voor respectievelijk MoS_2 en $MoSe_2$ nanoplaatjes en een volle breedte op halve hoogte (VBHH) (na hBN inkapseling) van 76 meV en 38.6 meV respectievelijk. Het syntheseprotocol van MoS_2 is verfijnd in hoofdstuk 3, om de laterale grootte van de nanoplaatjes te verkleinen. De reductie van de S:Mo verhouding tot 2 leidde tot MoS_2 nanoplaatjes met mono- en bilaagdikte, met een laterale grootte van 11.45 nm ± 4.89 nm en excitonenergie dicht bij eerder beschreven monolaag MoS_2. Fotoluminescentie spectroscopie onthult fotoluminescentie bij 80 K, gevormd door trion en neutraal excitonen gecentreerd bij 1.91 eV en 1.97 eV en met VBHH van 66 meV en 42 meV respectievelijk, zonder enige hBN inkapseling.
Deze resultaten rechtvaardigen de verschuiving in onderwerp van TMD's op molybdeenbasis naar TMD's op wolfraambasis. In het hoofdstuk WSe_2 wordt verslag gegeven over de optimalisatie van de synthese van WSe_2- nanoplaatjes, waarbij de resultaten van de masterstudent Diem Van Hamme over de optimalisatie van WS_2 als uitgangspunt zijn genomen. Het UV-Vis spectrum van het monster toonde de A en B excitonen met energie dicht bij monolaag WSe_2 nanoplaatjes en een monolaag dikte. X-stralen photoelektron spectroscopie analyse van de nanoplaatjes toonde de aanwezigheid van metallische polytypes en oxidesoorten, wat het ontbreken van fotoluminescentie van het monster rechtvaardigt. De synthese van molybdeen- en wolfraam-gebaseerde legeringen en $MoS_2/MoSe_2$ heterostructuren wordt behandeld in hoofdstuk 5. De synthese van de legeringen is gebaseerd op de overeenkomstige sulfideprotocollen, met toevoeging van elementair selenium als tweede chalcogenidebron. De resulterende legeringen, $MoS_xSe_{(2\text{-}x)}$ en $WS_xSe_{(2\text{-}x)}$ vertoonden in het UV-Vis absorptiespectrum de typische twee excitonen, met energieën tussen de zuivere selenide en sulfide monolaag monsters. Raman spectroscopie toonde de aanwezigheid aan van de karakteristieke A_{1g} -splitsing voor de MoS_2-legering en de aanwezigheid van zowel sulfide- als selenide- Raman-modi voor de WSSe-legering, wat de gelegeerde aard van het monster bevestigt. De $MoS_2/MoSe_2$ heterostructuur wordt verkregen door combinatie van de MoS_2 en $MoSe_2$ protocollen in een twee-staps synthese, eerst synthetiseren van MoS_2 en vervolgens in hetzelfde reactiemedium de $MoSe_2$ synthese te beginnen. De aldus verkregen heterostructuur wordt gekarakteri-

seerd door drie verschillende excitonische kenmerken in het UV-Vis absorptiespectrum, geassocieerd met $MoSe_2$ en MoS_2 soorten. Het Raman spectrum van het monster is opgebouwd uit enkele modi die geassocieerd zijn met zuivere $MoSe_2$ en MoS_2 nanoplaatjes, met de duidelijke afwezigheid van modi die geassocieerd zijn met gelegeerd materiaal. Het in kaart brengen van de samenstelling van het monster via energie-dispersieve X-stralen spectroscopie, onthulde de aanwezigheid van afgebakende regio's in samenstelling, wat de toewijzing van heterostructuur aan het monster ondersteunt.